Eindhoven University of Technology

MASTER

Towards CFD analysis of the natural ventilation of urban areas

development and application of urban CFD models based on GIS data for analysis of urban wind flow and heat transfer

Roelofs, J.G.J.

Award date:
2011

Where innovation starts

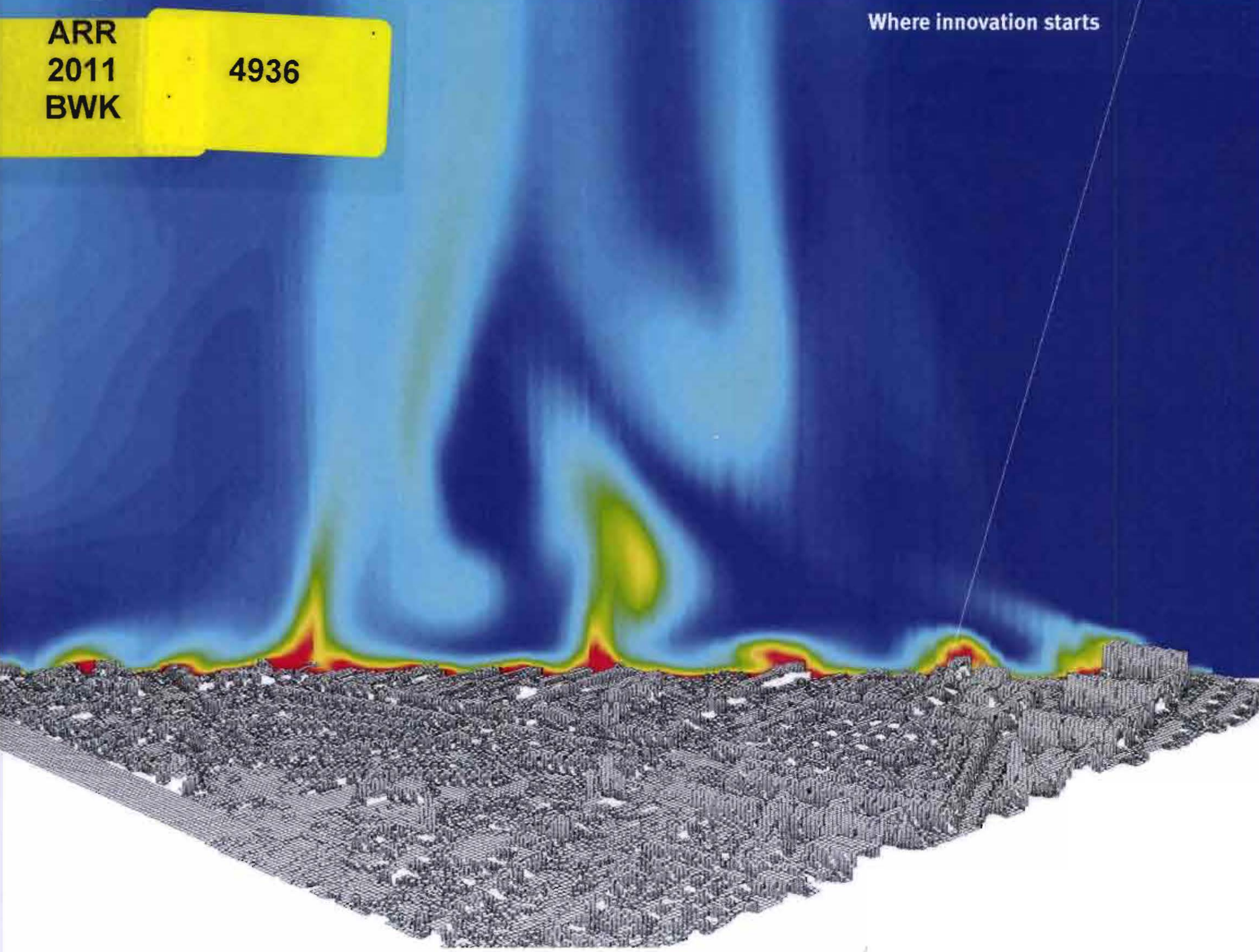

building physics and systems

Master thesis by J.G.J. Roelofs

Towards CFD analysis of the natural ventilation of urban areas

Development and application of urban CFD models based on GIS data for analysis of urban wind flow and heat transfer

Technische Universiteit
Eindhoven
University of Technology

MASTER THESIS – EINDHOVEN UNIVERSITY OF TECHNOLOGY

TU/e
Technische Universiteit
Eindhoven
University of Technology

Towards CFD analysis of the natural ventilation of urban areas

---

"Development and application of urban CFD models based on GIS data for analysis of urban wind flow and heat transfer"

J.G.J. Roelofs

November 2011

Towards CFD analysis of the natural ventilation of urban areas

"Development and application of urban CFD models based on GIS data for analysis of urban wind flow and heat transfer"

MSc thesis for obtaining the degree of Master of Science in Building Services at Eindhoven University of Technology

---

Author:	J.G.J. Roelofs (Jelle)
Committee:	Prof.dr.ir. B.J.E. Blocken (Chairman) Ir. T.A.J. van Hooff Ir. W.D. Janssen
Master:	Building Services
Department:	Built Environment
Unit:	Building Physics and Systems

Eindhoven University of Technology
21st of November 2011

Acknowledgement

Starting up a large project such as your Master thesis is always a difficult task, as the subject you choose has to be both interesting and challenging enough to keep you occupied for a relatively long period of time. About a year ago, after searching on the website of unit BPS, contacting companies, and talking to multiple professors, I finally choose a Computational Fluid Dynamics (CFD) project suggested by Bert Blocken. Less than a week later I joined a new group of PhD students for a refreshment course in 'high-quality CFD simulations'. Finishing my project took slightly longer than anticipated, but after months of hard work I am content with the process and the final result.

A special word of thanks goes out to my supervisors Bert Blocken, Twan van Hooff, and Wendy Janssen, for making this project possible by means of their critical attitude, expertise help, and motivating words. A second word of thanks goes out to Zara Huijbregts who got me started on programming the journal files that allowed for automating the grid-generation process. Also, I am most grateful that during my busy graduation period there was still time to enjoy another for me important and fun part of studying; being an active member of study association Mollier and in addition helping to organize the 2011 Russia study trip. During my graduation I spent many hours at the University where I worked together with my friends. For their sociability and for many "wasted" hours drinking coffee whilst discussing the less important things in life, I want to thank them and wish them all the very best.

Finally, I would like to thank my family: Koos, Ans, Marieke and Anne, for supporting my choices and believing in me throughout my years of study.

Jelle Roelofs
November 2011

Abstract

The aim of this study is to gain insight in the development and application of high-quality urban Computational Fluid Dynamics (CFD) models for analysis of natural ventilation of urban areas. To achieve this project aim, three research questions have been devised.

1) What information is available in literature with respect to natural ventilation of cities and the development of urban CFD models?
2) Can a high-quality CFD model be developed that can be used to analyze natural ventilation of a city by wind and buoyancy?
3) To what extent can Geographic Information System (GIS) data be used to develop a body-conformal structured grid for an urban CFD model and what are the current software capabilities and limitations?

To provide answers to the research questions, a literature review was conducted, a method was developed to generate the computational domain using GIS data, and finally isothermal and non-isothermal CFD simulations with the urban CFD model were conducted.

Based on the literature review and the obtained results, the following conclusions can be drawn. A fair number of papers are available on the subject of natural ventilation of cities. In general however, it should be noted that a very limited amount of information is available on, the advantages and disadvantages of the applied grid development methods, which problems might occur, possible software limitations, or what computational resources are required. Hence, knowledge made available through publications and other media would be beneficial for future projects in which urban CFD models are adopted. With respect to the second research question it can be stated that, despite the reduced target domain size in this study, an urban CFD model was successfully created and used to analyze natural ventilation of a city by wind and buoyancy. Lastly, this study has shown that GIS data can form the basis for generating an urban CFD model with a body-conformal structured grid. However, it has to be said that the applied method in this study was not yet optimal. By mapping and analyzing the knowledge obtained in this study, a step was made in the right direction towards developing a method to efficiently generate a body-conformal structured grid for urban CFD simulations.

Nomenclature

Roman symbols

B	constant in logarithmic law-of-the-wall	-
C_s	roughness constant	-
C_μ	constant in the standard k- ε model	-
g	gravitational constant	m/s^2
H	height of a building	m
k	turbulent kinetic energy	m^2/s^2
k_s	physical roughness height	m
n	number of terms	-
u, v, w	x, y, and z component of the instantaneous wind velocity vector	m/s
u′, v′, w′	fluctuating parts of u, v, and w	m/s
U, V, W	x, y, and z components of mean wind velocity-vector	m/s
u^*	friction velocity	m/s
u^+	dimensionless fluid speed	-
x, y, z	Cartesian coordinates	m
X, Y, Z	width, depth, and height	m
y^+	dimensionless wall coordinate y-plus	-
y_0	aerodynamic roughness length	m
y_p	distance from point P to the wall	m

Greek letters

α_p	power-law exponent	-
β	thermal expansion coefficient	K^{-1}
ε	turbulent dissipation rate	m^2/s^3
κ	von Karman constant	-
μ	dynamic molecular viscosity	kg/ms
μ_τ	dynamic turbulent viscosity	kg/ms
ρ	fluid density	kg/m^3

Dimensionless numbers

Fr	Froude number	-
Gr	Grasshoff number	-
Re	Reynolds number	-
Ri	Richardson number	-

Subscript

max	maximum
o	operating
ref	reference
temp	temperature
wall	wall

Acronyms

2-D	2-Dimensional
3-D	3-Dimensional
ABL	Atmospheric Boundary Layer
AHN	Algemeen Hoogtebestand Nederland/ General Height database Netherlands
BCG	Body-Conformal Grid
BPS	Building Physics and Systems

CAD	Computer Aided Design
CBD	Central Business District
CFD	Computational Fluid Dynamics
CHTC	Convective Heat Transfer Coefficient
DNS	Direct Numerical Simulation
GIS	Geographic Information System or Geospatial Information Science
UHI	Urban Heat Island
IB	Immersed Boundary
LES	Large Eddy Simulation
LIDAR	Light Detection and Ranging
RANS	Reynolds-Averaged Navier-Stokes
RMSE	Root Mean Squared Error
RNG	Renormalization Group
RSM	Reynolds Stress Model
TU/e	Technische Universiteit Eindhoven/ Eindhoven University of Technology

Contents

Acknowledgement.....i

Abstract.....iii

Nomenclature.....v

1 Introduction.....5
  1.1 Relevance of the project.....5
  1.2 Project aim and research questions.....6
  1.3 Project methodology.....6

2 Literature study.....9
  2.1 UHI effect.....9
  2.2 GIS data.....12
  2.3 CFD for wind flows in the urban environment.....13
    2.3.1 Approaches for modeling turbulent flow.....13
    2.3.2 Computational domain size.....13
    2.3.3 Computational grid.....14
    2.3.4 Atmospheric boundary layer flow.....15
    2.3.5 Turbulence modeling.....18
    2.3.6 Near-wall treatment.....19
    2.3.7 Thermal effects.....20
    2.3.8 IB and BFG method.....21

3 Validation studies.....23
  3.1 Case study for validation: 2-D wind flow pattern and wind speed.....23
    3.1.1 Description of validation case.....23
    3.1.2 Simulation characteristics.....24
    3.1.3 Comparison of simulation and measurements.....32
  3.2 Case study for validation: 2-D buoyancy effect.....37
    3.2.1 Description of validation case.....37
    3.2.2 Simulation characteristics.....38
    3.2.3 Comparison of simulation and measurements.....41

3.3 Case study for validation: 3-D wind speed and buoyancy effect 46
3.3.1 Description of validation case 46
3.3.2 Simulation characteristics 47
3.3.3 Comparison of simulation and measurements 49
3.3.4 Adopting standard wall functions instead of low-Re-number modeling 55

4 Method: development of urban CFD models 59
4.1 Generating the computational domain 59
4.2 Generating mesh files for the urban CFD models 62
4.3 Discussion of the applied methodology 64
4.4 Software errors and limitation: displayed errors 68
4.5 Software errors and limitation: software issues 70

5 Case study city Rotterdam: simulation set-up and results 71
5.1 Description of urban area and domains 71
5.2 Simulation set-up of for the case study city 74
5.2.1 Description of simulation variants 74
5.2.2 Description of grid and model characteristics 74
5.3 Computational domains 77
5.4 Homogeneous ABL flow 80
5.5 Isothermal case 81
5.6 Non-isothermal cases 86
5.6.1 Wind-induced flow 86
5.6.2 Buoyancy-driven flow 89
5.6.3 Convective heat transfer coefficient 94

6 Discussion 97
6.1 Methodology 97
6.2 Simulation results 97

7 Conclusions 101

8 Recommendation 103

References 105

Appendices (available on cd)

Appendix A: GIS data and the area of interest A1-A3

Appendix B: Validation cases supplements B1-B2

Appendix C: Wind speed, wind direction and roughness classification for Rotterdam C1-C3

Appendix D: Deformation of building shapes due to the use of GIS data D1-D2

Appendix E: Isothermal results E1-E17

Variant: U_{ref} = 8.0 m/s, domain *Station* E2

Variant: U_{ref} = 8.0 m/s, domain *Coolsingel* E7

Variant: U_{ref} = 8.0 m/s, domain *Residential area* E12

Appendix F: Non-isothermal results F1-F55

Variant: U_{ref} = 5.0 m/s, domain *Station* F2

Variant: U_{ref} = 0.1 m/s, domain *Station* F11

Variant: U_{ref} = 5.0 m/s, domain *Coolsingel* F20

Variant: U_{ref} = 0.1 m/s, domain *Coolsingel* F29

Variant: U_{ref} = 5.0 m/s, domain *Residential area* F38

Variant: U_{ref} = 0.1 m/s, domain *Residential area* F47

1 Introduction

1.1 Relevance of the project

Natural phenomena come in all sort of forms, such as floods, heat waves, droughts, tornados, hurricanes, volcanic eruptions, earthquakes, and landslides. When these occur in populated areas and cannot be prevented, they are referred to as natural disasters. It is possible to take precautions, e.g. building dikes, using earthquake and hurricane resistant foundations, and thorough investigation of geographic properties of areas before starting a building project. However, some natural phenomena, such as heat waves, cannot be prevented and are even amplified by human presence and activities.

Climate change is already increasing the global temperature. In addition to this global change, the temperature in urban environments increases due to the Urban Heat Island (UHI) effect. During heat waves, this additional temperature increase can significantly raise morbidity and mortality levels in cities (Matzarakis and Mayer, 1991; Changnon et al., 1996). A good example is the European heat wave of 2003, where over 35,000 people found their death of which an estimated 1,400 in the Netherlands (Earth Policy, 2003; New Scientist, 2003). A clear indicator that these deaths are also correlated to the UHI effect is the mortality rate in cities. For example in London, an estimated 900 people died from the heat, where heat related fatalities in the United Kingdom reached 2,045. Although heat waves are rarely given adequate attention, they claim more lives each year than floods, hurricanes, and tornadoes combined (Earth Policy, 2003). During heat waves, the elderly and infants are the most vulnerable groups. Besides people being physically uncomfortable, an increased temperature also has a negative effect on building cooling demand, a parameter which is directly dependent on the micro-climate conditions around a building.

The UHI effect refers to urban areas that are significantly warmer than the surrounding rural areas. Studies on nocturnal and diurnal UHI effect show contradicting results. Depending on the author, location and other variables, it was concluded that the temperature difference is larger during nighttime or during daytime. The effect however, is known to be most pronounced when wind speed and thus natural ventilation of the city are low. This phenomenon was first investigated and described at the beginning of the 19th century by the British amateur meteorologist Luke Howard (1818).
Bringing the complex problem of UHIs back to basics, the solution to mitigate the UHI effect would simply be counteracting of the sources. However, a city is an established and slowly changing environment. As a result, many countermeasures will take a long time to implement, not to mention that often measures will be impractical and financially not feasible. Mitigation measures can be categorized as those that can only be implemented during the design and planning phase, e.g. building materials and geometrical effects, and those which can also be implemented after the design and planning phase, for example more vegetation and roof spray cooling (Memon et al., 2008). Urban designers, urban physicists, architects, and other parties involved in developing urban environments must join forces in mitigating the UHI effect.

A tool that could be used to analyze wind flow and heat transfer in cities is Computational Fluid Dynamics (CFD). Traditionally, wind engineering simulations are performed in a computational domain implementing a single building and its direct surroundings or a small group of buildings. However, to address large scale problems, such as the UHI effect and pollution dispersion in cities, urban CFD models are required; models with a domain size that allows for the analysis of e.g. wind flow and heat transfer on a scale larger than a single building or group of buildings. With respect to these urban CFD models, a subdivision is made between microscale and mesoscale models. The latter can be used for the study of weather systems, whilst microscale models are more suitable for issues such as the UHI effect. For both model types nested-grid techniques can be applied which allow for the combination of a high-resolution grid in the target area and a coarser grid in other parts of the domain (Burrows et al., 2007; Nozu et al., 2008; Mochida et al., 2010). When dealing with urban CFD models, creating the computational grid is a time-consuming process which is often not straightforward. There are multiple modeling approaches possible towards creating these large computational grids:

- Manually create surface representation, e.g. buildings and streets (Dixon et al., 2003; Gidhagen et al. 2004; Huang et al., 2005; Chan and Leach, 2007; Lu et al., 2007);
- Semi-automated grid-generation using Geographic Information System (GIS) data directly in the preprocessor (this process will be described in chapter 0 of this report);
- Semi-automated grid-generation with the use of a Computer Aided Design (CAD) environment, GIS data can be utilized or basic maps in combination with added height data (Coirier et al., 2006b; Burrows et al., 2007).

For the manual modeling approach it was not explicitly stated in the reviewed papers that the grid was built manually. However, due to the grid size and the observation that the use of GIS data was not mentioned, this is a reasonable assumption. In other research projects (Coirier et al., 2006b; Tamura et al., 2006; Burrows et al., 2007; Yoshie et al., 2007; Neofytou et al., 2008; Nozu et al., 2008; Tamura, 2008) the use of GIS data was explicitly mentioned. It is also observed that for some of these projects a CAD environment was used to import GIS data to create surface representations. However, there is no information available on how GIS data could be used directly in combination with a preprocessor. In general, it can be said that a very limited amount of information is available on the advantages and disadvantages of the grid development methods, which problems might occur, possible software limitations, or what computational resources are required.

1.2 Project aim and research questions

The conducted literature study indicated a lack of available information on urban CFD models which are developed using GIS data. As a result, the emphasis in this study was not only placed on analyzing natural ventilation of cities, but foremost on the mapping of the applied methodology with respect to developing urban CFD models using GIS data. The heat transfer in the simulations was kept relatively simple by only including the convective heat transfer component. Heat transfer due to radiation and conduction are not included, nor are wall temperature differences due to, for example shadowing effect and thermal capacity of constructions.

The aim of this study is to gain insight in the development and application of high-quality urban CFD models for analysis of natural ventilation of urban areas.

To achieve this project aim, three research questions have been devised.

1) What information is available in literature with respect to natural ventilation of cities and the development of urban CFD models?
2) Can a high-quality CFD model be developed that can be used to analyze natural ventilation of a city by wind and buoyancy?
3) To what extent can GIS data be used to develop a body-conformal structured grid for an urban CFD model and what are the current software capabilities and limitations?

1.3 Project methodology

In this project CFD is used to analyze the natural ventilation of a city by wind and thermal buoyancy. CFD is a numerical approach for predicting fluid flow, heat and mass transfer, chemical reactions, and related phenomena by numerically solving the set of governing mathematical equations.

The Dutch harbor city of Rotterdam will serve as a case study city because of the presence of interesting high-rise and medium-rise buildings in the central business district (CBD) and the oceanic climate influence on the city. In addition, recently updated Geographic Information System (GIS) data have become available for the city of Rotterdam. The most recent observations provide height data with a grid resolution of 0.5 m.

To provide answers to the research questions; a literature review was conducted, a method was developed to generate the computational domain using GIS data, and finally CFD simulations were performed. The literature review provided answers on aspects such as, the UHI effect, GIS data, state-of-the-art in developing urban CFD models, and the natural ventilation of cities. The methodology is schematically presented in Figure 1-1. Emphasis in this project was placed on the used methodology for generating the computational domain using GIS data. Preparing the GIS data and producing the journal files for the preprocessor Gambit (Gambit, 2004) was conducted with the mathematical application Matlab R2010a (the MathWorks Inc., 2010). The commercial CFD code Ansys Fluent 12.1.4 (Ansys, 2009) was used for solving the Navier-Stokes equations and predicting the turbulent flow. Papers describing wind tunnel experiments were used for validation purposes.

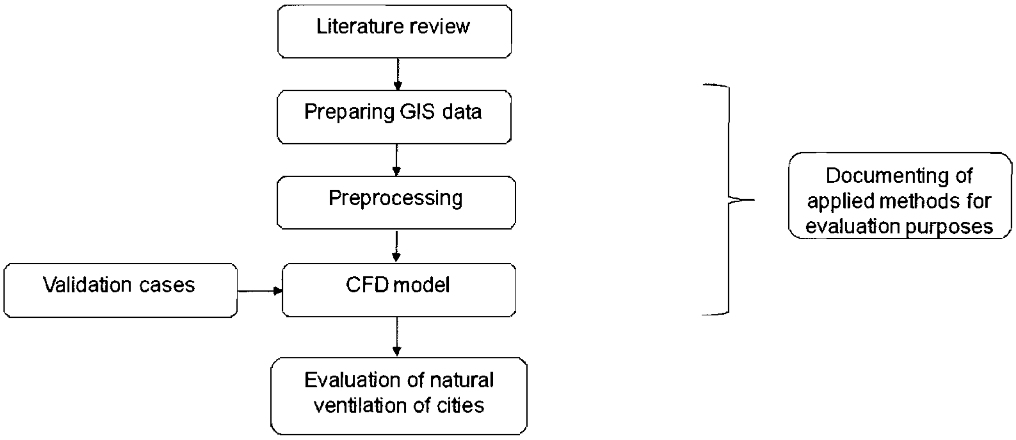

Figure 1-1: Schematic representation of the applied methodology.

Reducing the size of the target area

One of the project aims is to create a high-quality urban CFD model of the case study city Rotterdam. This translates into an intended target area of approximately 4.2 km^2 and a computational domain of an estimated 32 million cells. This estimation is based on the adopted grid resolution and observed blockage ratio in the computational domains that have been generated for this study. The term 'target area' in this study refers to that part of the domain where buildings are explicitly modeled. A two-way nested-grid technique would be used to minimize cell count and allow for a higher resolution in the two target areas: *Station* and *Coolsingel*. Unfortunately, the adopted approach, combined with limitations of the CFD software, do not allow for the intended computational domain of 4.2 km^2. To continue the study, the part of the city that is incorporated into the CFD model was reduced. Instead of one large computational domain three smaller domains were defined. To limit the time needed to create these new computational domains, grid resolution of the target areas is kept the same; the three new computational domains were built with the mesh files that had already been generated. The three domains can be described as follows:

- Domain 1: *Station*, a cluster of high-rise office buildings near the central railway station (size of target area 400 x 400 m^2).
- Domain 2: *Coolsingel*, the main shopping street of Rotterdam (size of target area 300 x 400 m^2).
- Domain 3: A *Residential area* in the center of Rotterdam (size of target area 1000 x 1000 m^2).

Simulations

After the validation study was performed and the computational domains were created, the final simulations where conducted. Firstly, a set of isothermal simulations were conducted, followed by two sets of non-isothermal simulations designed to analyze the natural ventilation of the three urban areas. For this purpose, the bulk Richardson number is introduced. With respect to wind flow around buildings the bulk Richardson-number can be adopted to derive whether a flow is either wind-induced or buoyancy-driven. The theoretical background on the bulk Richardson-number is elucidated in paragraph 2.3.7. The three simulation sets are:

- Isothermal.
- Wind-induced ventilation flow, $Ri \ll 1$.
- Buoyancy-driven ventilation flow, $Ri \gg 1$.

With respect to the three simulation sets, the isothermal and the wind-induced ventilation flow variants are very much alike. However, the non-isothermal simulations also takes into account the possible influence of buoyancy effect on the ventilation flow which might occur in areas of, for example low wind speed.

2 Literature study

2.1 UHI effect

In the introduction chapter the UHI effect was briefly discussed. Stated was that the UHI effect refers to urban areas that are significantly warmer than the surrounding rural areas, both during day- and nighttime. This temperature difference is most pronounced when wind speed in the city and thus natural ventilation are low. Figure 2-1a and Figure 2-1b show a practical example of the UHI effect in Singapore. The former shows recorded temperature fluctuations in an urban area; the latter also gives an indication on how large the temperature differences between urban and rural areas can be. Important to know is that the effect of an UHI is not limited to an increase in air temperature. Side effects of increased temperature are, for example decreased air quality due to the increased production and change in dispersion of pollutants (Rosenfeld et al., 1998; Sarrat et al., 2006). Water quality also decreases as warm water flows into surface waters stressing the ecosystem. Higher air temperatures also result in an increase in energy demand for cooling, but a decreased energy demand in winter (Konopacki and Akbari, 2002). Aside from increased air temperatures, the UHI effect can also induce large scale effects. The local climate can be affected by altering wind patterns, the development of clouds and fog, and even rates of precipitation.

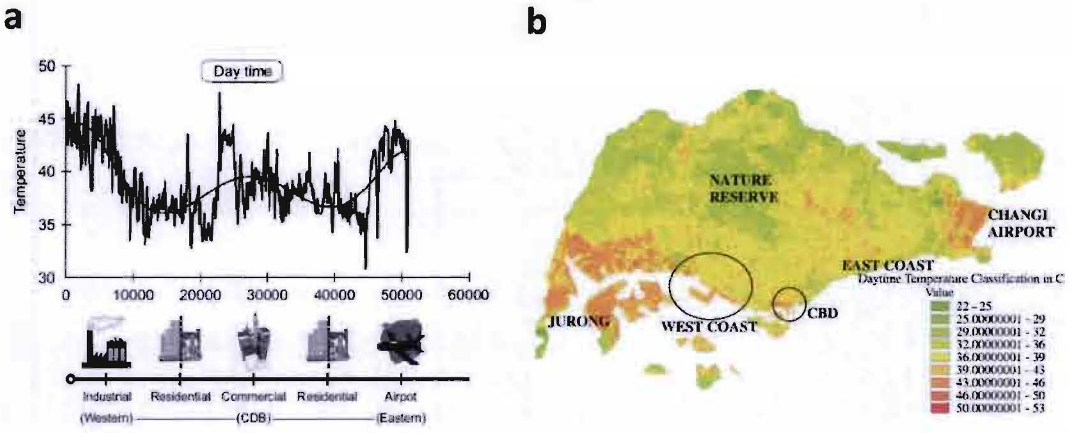

Figure 2-1: a) Temperature profile of daytime surface temperature distribution from west to east of Singapore (Jusuf et al., 2007); b) daytime surface temperature classification (Jusuf et al., 2007).

The UHI effect is a global issue; all around the world research projects are being conducted in which causes are being analyzed and possible mitigation measures proposed. Striking is the number of research reports available on the analysis of causes and effects of the UHI effect with respect to a case study city. Some examples of case study cities are, Hong Kong (Giridharan et al., 2005), New Jersey (Solecki et al., 2005), Singapore (Jusuf et al., 2007), London (Giridharan and Kolokotroni, 2009), Crete (Kolokatsa et al., 2009), and Nanjing (Zeng et al., 2009). In these studies, data analysis software was used to obtain results.

Causes

The urban air temperature is rising in cities around the world. There are several causes for the presence of these UHIs, although not all of equally large influence. Below an overview is given on what, in literature, are thought to be the main causes.

Causes can be divided into the categories "controllable" and "uncontrollable" (Memon et al., 2008). Examples of uncontrollable factors are, wind speed, cloud cover, and solar irradiation. These factors are environmental and nature related, and are beyond our control. For this reason, uncontrollable factors will not be further discussed. On the other hand there are the controllable factors, i.e. influenceable causes which can be humanly controlled, such as heat release from buildings and difference in applied building materials between urban and rural areas. These sources are discussed below.

Storing and re-radiating
Commonly used building materials in urban areas are different to those used in rural areas. Changing thermal properties of building materials, e.g. heat capacity, conductivity, and radiative properties (albedo and emmisitivity) result in an increased UHI effect. In addition to building materials, also other surface materials in urban areas are different to those in rural areas. Urban areas will for example have a more extensive infrastructure, meaning additional black asphalt and pavement in which more heat can be absorbed and released. Lastly, the geometrical effects are discussed; in densely built areas, large and high buildings provide multiple surfaces for the reflection and absorption of sunlight, increasing the efficiency with which urban areas are heated. This is called the urban heat canyon effect. Large and high buildings also block wind and by doing so decrease natural ventilation of a city (Oke, 1982; Tamura et al., 2006; Memon et al., 2008; Tamura, 2008).

Waste heat
Waste heat from automobiles, air conditioning, industry, and other sources also contributes to the UHI. This source is, like many other sources, strongly dependent on factors such as population density.

High levels of pollution
Closely related to waste heat is pollutant dispersion. Many forms of pollution change the radiative properties of the atmosphere, which can result in a decreased heat release from the city to her surroundings (Oke, 1982; Sarrat et al., 2006; Memon et al., 2008). This could be interpreted as a greenhouse effect on an urban scale.

Less evapotranspiration
Due to a lack of trees and other vegetation in urban areas there is less evaporation and plant transpiration from the Earth's land surface to the atmosphere (Jusuf et al., 2007; Giridharan et al., 2008; Memon et al., 2008; Giridharan and Kolokotroni, 2009). Referring back to the storage and re-radiating source, lack of vegetation not only results in less evapotranspiration, but also changes storage and re-radiating properties of an urban area.

Of the sources mentioned above: storage, re-radiating and waste heat are identified by Memon et al. (2008) as the main sources of heat in an urban area. The correlation between high pollution levels and the UHI is less often regarded significant with respect to the three main sources. Furthermore, lack of evapotranspiration is not regarded as a source of heat, but more a missed opportunity in mitigating the UHI effect.

Mitigation
Table 2-1 shows the overview that Memon et al. (2008) made of mitigation measures as proposed by various researchers. For part of the proposed mitigation measures the predicted maximum temperature reduction and possible energy savings was estimated. Thus far however, most proposed mitigation measures as described in literature have not been implemented on a large scale, but merely simulated numerically. The actual effectiveness of these measures therefore remains debatable.

Increasing evapotranspiration by planting vegetation is the most widely applied mitigation measure. Expected maximum temperature reduction is in the range of 1.0 - 1.5 °C (Ca et al., 1998; Ashie et al., 1999; Tong et al., 2005), combined with other measures maximum reduction is estimated to be 1.2 -

3.0 °C (Rosenfield et al., 1998; Taha et al., 1999; Kikegawa et al., 2006). The studies previously mentioned assume increased evapotranspiration by creating parks and green zones. An alternative to increasing evapotranspiration by parks and green zones is the introduction of green roofs (Takebayashi and Moriyama, 2007; Geridharan et al., 2008). When implementing mitigation measures, location is of importance; Geridharan et al. (2008) for example, acknowledges a temperature reduction by increasing evapotranspiration, but stresses that introducing vegetation in high-density high-rise developments will not lead to an significant reduction in outdoor temperature.

Table 2-1: Proposed mitigation measures, maximum temperature reduction, and possible energy savings (Memon et al., 2008).

Mitigation measure	Max. temp. reduction (°C)	Reported savings [%]	Reference
Roof spray cooling	13–17 (ceiling temperature)	40 (electrical consumption)	Jain and Rao, 1974
Flow of water over roof	-	-	Sodha et al., 1980
Roof pond, roof spray cooling and moving water over roof	-	-	Tiwari et al., 1982
Planting and vegetation	1.5	-	Ca et al., 1998
Vegetation, lighter color of paving and cooler roofs	3.0	-	Rosenfield et al., 1998
Planting and vegetation	1.3	25	Ashie et al., 1999
Vegetation and suitable albedo	2.0	10	Taha et al., 1999
Reducing anthropogenic heat and energy consumption, improvement in building design	-	-	Urano et al., 1999
Planting and vegetation	-	-	Spronken-Smith et al., 2000
Turn air-conditioners off	1.0	6	Kikegawa et al., 2003
Planting and vegetation	1.5-1.6	-	Tong et al., 2005
Reducing anthropogenic heat and planting vegetation	1.2	40	Kikegawa et al., 2006
Proper ventilation		10	Kolokotroni et al., 2006
Shades, highly reflective materials, open and airy spaces, reduce heat release from buildings etc.	-	-	Yamamoto, 2006
Planting and vegetation		10	Yu and Hien, 2006
Photovoltaic canopies	-	-	Golden et al., 2007
Green and highly reflective roofs	-	-	Takebayashi and Moriyama, 2007
Humidification and albedo increase	-	-	Ihara et al., 2008

UHI effect and CFD

To create a realistic model to predict the UHI effect, both wind and thermal buoyancy need to be included in the CFD model. Modeling wind flows is a common practice; however, extra attention is still needed to correctly include thermal effects. The driving force behind thermal buoyancy is a temperature difference between the air, building surfaces, and other surfaces. To capture the essence of this problem, heat fluxes from these surfaces need to be known. This can be done by either imposing surface temperatures *T* or heat fluxes *Q* on building surfaces and other surfaces.

Currently, the largest obstacle is that it is almost impossible to measure heat transfer on such a large scale. Maybe in the near future using satellite technology, measured heat transfer on an urban level can be combined with numerical simulation techniques to accurately assess the UHI effect (Memon et al., 2008). Meanwhile, small-scale measurements could be extrapolated to provide an insight in heat transfer in the urban environment. Another option is to measure surface temperatures. These measurements could for example be conducted using thermal imaging cameras; both pictures and time dependent data can be obtained using this technique.

2.2 GIS data

Manually defining all the buildings and obstacles for the grid of an urban area is a time-consuming practice. In this sense, the use of GIS data seems a more effective and more practical approach as it can be used to semi-automate the grid-generation process.

Geographic Information System (GIS) or Geospatial Information Science, is a set of tools that captures, stores, analyzes, manages, and presents data that are linked to locations. In the simplest terms, GIS is the merging of cartography, statistical analysis, and database technology. Practically, one could think of using GIS data for population mapping, demographic studies, resource management, and location planning. Another application is measuring and storing height data. In this project the General Height database for the Netherlands (AHN, NL: Algemeen Hoogtebestand Nederland) is utilized (AHN, 2010).

In 2003, height data were available for the Netherlands with a resolution of one measurement point per square meter and a precision of 0.15 m. Less recently updated parts have a resolution of one point per sixteen square meter. Technological development and government subsidies however, have allowed for a project in which all height data will be updated in the period 2007-2012. For the case study city Rotterdam, height data measurements were performed in 2008. The updated AHN data provides data on a structured grid with a resolution of 0.5 m. Also, the precision has improved to a maximum deviation of 0.05 m. (AHN, 2010)

Measurements for the AHN cannot be conducted throughout the year, as in order to obtain accurate results, height measurements have to be performed when trees are leafless and the grass is still short (AHN, 2010). As a result, surveillance flights are limited to the period end of January – end of March. To conduct the measurements, airplanes are equipped with lasers and so-called LIDAR technology. LIDAR is short for Light Detection and Ranging; an optical remote technology to find and range distant objects by measuring properties of scattered light.

The utilized data in this project were available as grid data in text file format. These grid data consisted of rows and columns, where each cell stores a single value; each line in the data-file represents one xyz-coordinate. The xy-coordinates are based on the Dutch 'Rijksdriehoekscoördinaten'; a system of standardized geographical coordinates. A single xyz-file as provided by AHN represents an area of 1 km x 1.25 km. Consequently, the Netherlands is divided into 1.25 km^2 encoded sections. This subdivision is shown in Appendix A for the southwest of the Netherlands. Figure 2-2 shows an example of how height data can be represented visually.

Figure 2-2: Digital elevation model of the Netherlands, a visual representation of the height data (www.ahn.nl/viewer, November 2010).

2.3 CFD for wind flows in the urban environment

2.3.1 Approaches for modeling turbulent flow

Because the atmospheric boundary layer (ABL) flow is turbulent, Franke et al. (2007) state that an unsteady treatment is required. The solving method should be able to predict the general flow pattern in the urban area whilst considering the effect of turbulence in the flow field and changing wind pressure on building surfaces. In general, Direct Numerical Simulation (DNS), Large Eddy Simulation (LES), and Unsteady Reynolds-Averaged Navier-Stokes (URANS) are suitable methods for solving unsteady flow predictions. It is expected however, that DNS, in which the Navier-Stokes equations are solved entirely, will not be attainable for some time to come. For this reason it is only used for simple geometries and low-Reynolds-number flows.

Taking into account the desired model accuracy and assuming enough computational resources are available for LES, this method could be considered an appropriate solving method in this project. In multiple studies, urban areas in Tokyo have been simulated using LES for flow prediction. In comparison with both full-scale field measurements and experimental wind tunnel data, LES showed good results (Tamura et al., 2006; Nozu, 2008; Tamura, 2008).

Another option is the Reynolds-Averaged Navier-Stokes (RANS) approach, which is also known to be used for wind flow prediction in cities with simulation results that are in good agreement with the full-scale measurements (Tamura, 2008; van Hooff and Blocken, 2010). The RANS approach is the most widely applied and validated method in the field of numerical simulation for wind flow around buildings; a big advantage of using RANS is the reduced computational cost (Franke et al., 2004; Tominaga et al., 2008).

2.3.2 Computational domain size

The size of the computational domain depends on the size of the target area and the boundary conditions that will be used. The target area refers to that part of the domain where buildings are explicitly modeled. For LES, an additional requirement is that the domain should be large enough to allow for the largest, energetically relevant flow structures to be solved. Similarly, for RANS the domain should be large enough to ensure that the wake of buildings is not influenced by the domain boundaries. Guidelines (Franke et al., 2007; Tominaga et al., 2008) are available that suggest domain dimensions in the vertical, lateral and flow direction, based on the highest building present in the target area. A computational domain of cuboid shape is presumed.

In general, a maximum blockage ratio of 3% is recommended by the CFD community. This is based on the results of Baetke et al. (1990) for the flow over a wall mounted cube. Other published recommendations however, suggest a much lower blockage ratio of 1.5% (Cowan et al., 1997; Hall, 1997; Bartzis et al., 2004; Scaperdas and Gillham, 2004).

For domains with a single building Franke et al. (2007) recommend the top of the computational domain to be at least $5H_{max}$ away from the tallest building with height H_{max}. After having chosen the domain height, lateral and streamwise direction extension can be determined based on the required blockage ratio. In general, in the lateral direction using $5H_{max}$ is recommended, where in the flow direction $5H_{max}$ upstream and $15H_{max}$ for the wake is recommended (Cowan et al., 1997; Scaperdas and Gilfham, 2004; Franke et al., 2007). These suggested domain extensions are depicted in Figure 2-3. For urban areas with multiple buildings, lateral and streamwise domain extension can be shorter than the proposed $5H_{max}$ and $15H_{max}$ (Franke et al., 2007). No suggestion however, is given on how much shorter, but recommended is that at least two different distances from the target area are tested.

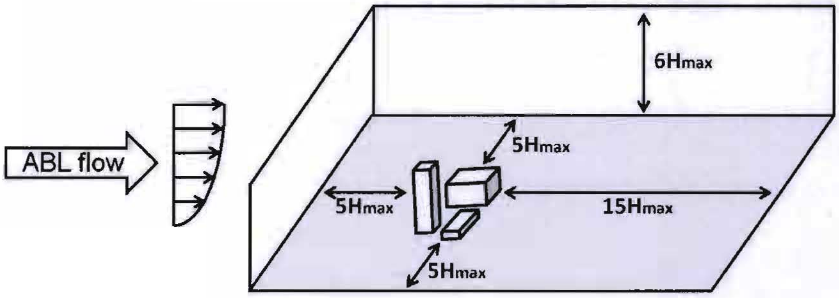

Figure 2-3: Suggested domain extensions.

2.3.3 Computational grid

A high-quality grid is ideally equidistant, preferably with hexahedral shaped cells. Also grid stretching should be kept to a minimum in regions of high gradients. Expansion between two consecutive cells should be below 1.3 (Franke, 2007). Scaperdas and Gilham (2004), and Bartiz et al. (2004) even recommend a maximum of 1.2 for the expansion ratio.

Concerning the minimum grid resolution, literature sources suggest at least 10 cells per building side and 10 cells per cube root of building volume (Franke et al., 2007; Tominaga et al., 2008). In addition, a grid-sensitivity analysis should be conducted to obtain a grid-independent solution. Franke et al. (2004) states that at least three substantially refined grids should be used so that the ratio of consecutive grids is at least 1.5 in each dimension. In a 3-D case each consecutive grid should therefore be refined by a ratio of 3.4.

No proposal or guideline could be found concerning the maximum number of cells that should be applied in the computational domain. Therefore, it is credible that the amount of computational cells is only limited by capabilities of the software packages used and available computational resources.

When implementing a relatively large urban area into a computational domain, two-way nested-grid techniques allow for an improved spatial accuracy in the target area (Brown et al., 2000; Cox et al., 2000; Ehrhard et al., 2000; Murakami et al., 2003a; Murakami et al., 2003b; Coirier et al, 2006a; Kondo et al, 2006; Nozu et al., 2008; Baik et al, 2009). The concept of this method is that multiple nestings are defined, where each nesting has a different grid resolution. Consequently, at each time step information of the coarser grid is projected on the adjacent finer grid and vice versa (Nozu and

Tamura, 2006). Decreased computational resources can be expected due to the use of a coarser grid. However, precaution is needed with respect to the coarseness of the grid applied for the nestings. A grid that is too coarse is not a suitable representation of an urban area. Instead it will behave like a homogeneous terrain with a low roughness height. This could lead to an artificial acceleration of the vertical wind speed profile, something which should be prevented at all times (Blocken et al., 2007).
Continuing on the above, an important aspect is the choice of a suitable resolution of the grid together with the domain size. Nozu et al. (2008) applied the two-way nested-grid technique on a domain of 1 x 2 km^2 with three nestings and corresponding grid sizes of 2 m, 4 m, and 8 m. Other examples of applied target area sizes, where GIS data is used to create a structured grid, are 1.75 x 1 km^2 (Tamura, 2008) and 1.5 x 1 km^2 (Tamura et al., 2006), the former with a grid resolution of 5 m, the latter with grid resolution 2.95 m. The generated grids of the target areas of two of these projects are shown in Figure 2-4.

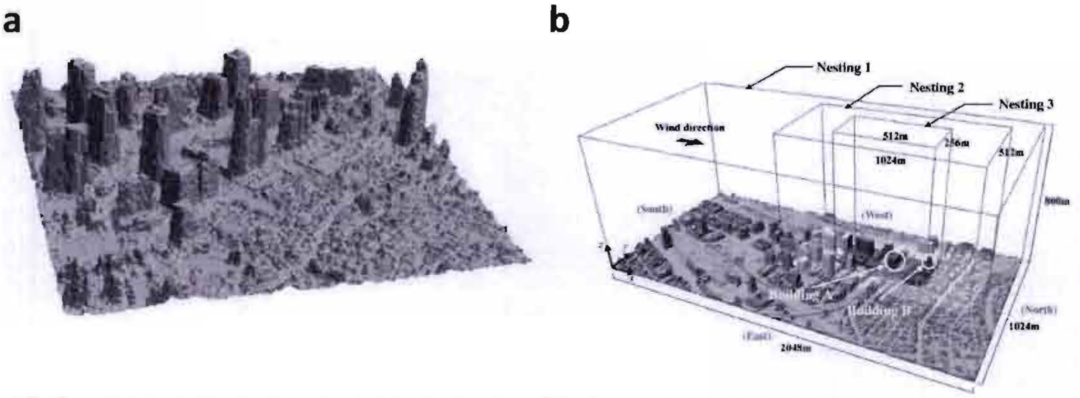

Figure 2-4: Grids of the target area in the studies of a) Tamura (2008); b) Nozu et al. (2008).

2.3.4 Atmospheric boundary layer flow

Inlet boundary condition profiles

As inflow boundary condition, wind speed and turbulence profiles are usually prescribed. Non-isothermal simulations might also include a temperature profile. For LES and other unsteady simulation approaches, time dependent boundary conditions are required. For a steady description of the flow field, similar wind speed and turbulence profiles can be considered. By averaging the approach flow variables, the time dimension is eliminated. Several types of wind speed profiles can be considered, below three options are discussed.

a) Theoretical/empirical equilibrium boundary layer flows: For neutral Atmospheric Boundary Layer (ABL) flows, the mean wind speed profile is obtained from a logarithmic (or log-law) equation using the aerodynamic roughness length. Turbulence profiles are also obtained from theoretical or empirical formulas.
b) Experimental data: Validated wind speed and turbulence profiles from wind tunnel experiments or full-scale measurement can be applied. As opposed to ABL flows based on theoretical or empirical formulas, profiles based on experimental data are not necessary constant across the width of the inlet boundary.
c) Driver regions: To obtain realistic inlet profiles driver regions can be used. A driver region can generate and inflow wind speed and turbulence profile for the main region. The vertical wind speed profile and turbulence characteristics at the inflow boundary of the driver domain can be given by for example empirical profiles. The variables at a single y-z section can be reintroduced as inflow boundary for the main region. The ground boundary condition of the driver domain can be defined by either an aerodynamic roughness length or by a geometry representing the urban area. Also, a driver domain could be used to thermally stabilize the boundary layer based on, e.g. sea breeze characteristics. (Tamaru, 2008)

Homogeneous boundary layer flow

A horizontally homogeneous boundary layer flow is required in the upstream region of the target area. Horizontally homogeneous in this context refers to the absence of streamwise gradients in the streamwise direction for the vertical wind speed and turbulence profiles, i.e. the inlet profiles are maintained in the downstream direction. Homogeneity is possible when the ground roughness is in balance with the vertical profiles of mean wind speed, turbulence properties, and the thermal profile in case of non-isothermal stability. In many CFD codes, wall roughness is described by an equivalent sand-grain roughness height and four requirements should simultaneously be satisfied (Blocken et al., 2007):

1) A sufficiently high mesh resolution in the vertical direction close to the bottom of the computational domain;
2) A horizontally homogeneous ABL flow in the upstream and downstream region of the target area;
3) A distance y_P from the center point P of the wall-adjacent cell to the wall (bottom of domain) that is larger than the physical roughness height k_S of the terrain ($y_P > k_S$); and
4) Knowing the relationship between the equivalent sand-grain roughness height k_S and the corresponding aerodynamic roughness length y_0.

Usually it is impossible to satisfy all requirements, for example if the relation $k_S \approx 30 \cdot y_0$ is assumed and $y_0 = 0.03$ m, then $y_P > k_S = 0.9$. This illustrates that even with a relatively low ground roughness large cells close to the ground should be used which is in conflict with the first requirement. Often the fourth requirement is abandoned and k_S is taken low. Assuming a low k_S however, results in an artificial acceleration of the wind speed profile and herewith a horizontally inhomogeneous flow. A solution would be to implement new and approved wall functions. This is not possible in all commercial CFD codes. Two suggestions were made by Franke et al. (2004), followed by four more by Blocken et al. (2007):

1) A variable height of the wall adjacent cell;
2) Explicitly modeling the roughness blocks upstream of the model;
3) Artificially reduce turbulent kinetic energy;
4) Reduction of upstream length of computational domain;
5) Employing wall shear stress boundary conditions; and
6) Implementation of a user-defined function overruling the existing k_S and y_0 relationship.

In the same paper as the above suggestions were made by Blocken et al. (2007), the relationship between k_S and y_0 was determined with respect to the commercial CFD code Ansys (2009a).

$$k_s = \frac{9.793 \cdot y_0}{C_s} \qquad \text{(Eq. 2.1)}$$

From the Ansys user's guide (2009a) it can be derived that for fully rough walls only the product of C_S and k_S occurs in the wall functions meaning that not the individual variables, but the product is leading. Also, Ansys does not allow k_s to be larger than y_p, which is the center point of the wall-adjacent cell. If a higher value for k_s is set by the user Ansys will automatically change it back to y_p without warning. However, utilizing the observation that the relationship between k_s and C_s is leading, k_s can be purposefully be chosen to be equal or smaller than y_p whilst adjusting the roughness constant C_s to satisfy the equation above. A user-defined function is applied to implement C_s because Ansys only allows a value in the interval [0-1] (Blocken et al., 2007). Experience in this graduation project has taught that even when applying a user-defined function, a maximum value for C_s of 7-10 is acceptable. Without apparent mathematical and numerical cause simulations tend to diverge when this value is exceeded.

Mean wind speed profiles

The log-law and power-law based vertical wind speed profiles are most commonly used in wind engineering when measured values are not available. An often applied, simplified log-law profile, as described by Richards and Hoxey (1993) is defined as follows:

$$U(y) = \frac{u^*}{\kappa} \cdot \ln\left(\frac{y+y_0}{y_0}\right), \qquad \text{(Eq. 2.2)}$$

where U(y) is the mean wind speed at height y, u* is the friction velocity, κ the Von Karman constant, and y_0 the aerodynamic roughness length. The introduced aerodynamic roughness length y_o is an empirical representation of the roughness of a landscape (Table 2-2).

Table 2-2: Updated Davenport roughness classification (Wieringa, 1992).

y_o [m]	Landscape description
0.0002 *Sea*	Open sea or lake (irrespective of the wave size), tidal flat, snow-covered flat plain, featureless desert, tarmac and concrete, with a free fetch of several kilometers.
0.005 *Smooth*	Featureless land surface without any noticeable obstacles and with negligible vegetation; e.g. beaches, pack ice without large ridges, morass, and snow-covered or fallow open country.
0.03 *Open*	Level country with low vegetation (e.g. grass) and isolated obstacles with separations of at least 50 obstacle heights; e.g. grazing land without windbreaks, heather, moor and tundra, runway area of airports.
0.10 *Roughly open*	Cultivated area with regular cover of low crops, or moderately open country with occasional obstacles (e.g. low hedges, single rows of trees, isolated farms) at relative horizontal distances of at least 20 obstacle heights.
0.25 Rough	Recently-developed "young" landscape with high crops or crops of varying height, and scattered obstacles (e.g. dense shelterbelts, vineyards) at relative distances of about 15 obstacle heights.
0.5 *Very rough*	"Old" cultivated landscape with many rather large obstacle groups (large farms, clumps of forest) separated by open spaces of about 10 obstacle heights. Also low large vegetation with small interspaces, such as bush land, orchards, young densely-planted forest.
1.0 *Closed*	Landscape totally and quite regularly covered with similar-size large obstacles, with open spaces comparable to the obstacle heights; e.g., mature regular forests, homogeneous cities or villages.
> 2.0 *Chaotic*	Centers of large towns with mixture of low-rise and high-rise buildings. Also irregular large forests with many clearings.

The original paper or book in which the power-law profile is first proposed was not found. One of the non-original papers in which this profile is described is in that of Heier (2005):

$$U(y) = U_{ref} \cdot \left(\frac{y}{y_{ref}}\right)^{\alpha}, \qquad \text{(Eq. 2.3)}$$

where U_{ref} is the reference wind speed at height y_{ref} and α the log-power exponent; which takes into account the terrain roughness.

Turbulent kinetic energy k and turbulent dissipation rate ε

When compared to wind speed profiles, measured values for k and ε are even less often available. Instead, the theoretical profiles for k and ε (Eq 2.4 and Eq. 2.5) by Richards and Hoxey (1993) are usually applied.

$$k = \frac{u^{*2}}{\sqrt{C_\mu}} = 3.33u^{*2}, \qquad \text{(Eq. 2.4)}$$

where C_μ is a constant in the k-ε model and u* the friction velocity.

$$\varepsilon = \frac{u^{*3}}{(\kappa \cdot (y + y_o))} \qquad \text{(Eq. 2.5)}$$

Note that in the two formulas above, the u* carries the effect of roughness.

2.3.5 Turbulence modeling

Characteristic for RANS solving method is that the RANS equations are solved, i.e. the mean flow; turbulence models are used to model all eddies. It is a fact that no single turbulence model is universally accepted as being superior for all classes of problem. As a result, 15 turbulence models are available in Ansys (2009b) to close the RANS equations. In this paragraph, four widely applied turbulence models are described: the standard k-ε model, the realizable k-ε model, the RNG k-ε model, and the Reynolds Stress equation Model (RSM).

k-ε Models in general
Linear k-ε models model the Reynolds stresses by adopting the extended Boussinesq hypothesis that relates the stresses to the mean rate of deformation (Hinze, 1975). The k-ε model adds two equations to the RANS equations; a transport equation for turbulent kinetic energy k and a transport equation for turbulent dissipation rate ε. The advantage of this approach is the relatively low computational cost associated with the computation of the turbulent viscosity. Disadvantage is that in the derivation of the model, it is assumed that the flow is fully turbulent and that the effect of molecular viscosity is negligible. As a result, this model is only valid for fully turbulent flows. Another well known shortcoming of this modeling approach is the overestimation of k in regions of high pressure gradients. (Casey and Wintergerste, 2000; Launder and Spalding, 1974)

Standard k-ε model
The most well known linear k-ε model is the standard k-ε model. Due to its robustness, economy, and relative high accuracy for a wide range of turbulent flows, application of this turbulence model has been popular since it was proposed by Launder and Spalding (1972). After the strengths and weaknesses of the standard k-ε models became known, improvements were made. Two variants are available in Ansys (2009b), the realizable k-ε model (Shih et al., 1995) and the RNG k-ε model (Yakhot and Orszag, 1986).

RNG k-ε model
The RNG k-ε model (Yakhot and Orszag, 1986) is based on the instantaneous Navier-Stokes equations. An analytical derivation technique called the "renormalization group (RNG)" method, resulted in this model with different constants than the standard k-ε model. Also the transport equations for k and ε are altered; additional functions and terms are adopted. A more comprehensive description of the RNG theory and its relation with turbulence modeling can be found in the work of Orszag et al. (1993). Important benefits of the RNG approach are, for example, including the effect of swirl on flows and providing an analytical formula for Prandtl numbers (in contrast to the user-defined Prandtl number for the standard k-ε model). Also, in contrast to the standard k-ε model, the RNG k-ε model provides formulas that better support low-Re-number effects. The effectiveness of this measure is highly dependent on the near-wall treatment. (Ansys, 2009a)

Realizable k-ε model

The realizable k-ε model (Shih et al., 1995) differs from the standard k-ε model in two important ways. The first is that the turbulent viscosity is newly formulated. Secondly, a new transport equation for the dissipation rate ε has been derived from an exact equation for the transport of the mean-square vorticity fluctuation. The term "realizable" means that the model satisfies certain mathematical constraints on the Reynolds stresses. Neither the standard k-ε model nor the RNG k-ε model is realizable. An immediate benefit of the realizable k-ε model is that it is likely to provide superior performance for flows involving rotation, boundary layers under strong adverse pressure gradients, separation, and recirculation. (Ansys, 2009a)

RSM

An alternative approach to the Boussinesq hypothesis based models is the Reynold Stress equation Model. In Ansys (2009b) three options are available for solving the pressure-strain term: 1) linear pressure-strain, modeled according to the proposals by Gibson and Launder (1978), Fu et al. (1987), and Launder (1989a; 1989b); 2) quadratic pressure-strain (Speziale et al. 1991), and 3) low-Re stress-omega, based on the omega equations and the Local Linear Regression (LLR) model (Wilcox, 1998).

In this model the isotropic eddy-viscosity hypothesis is abandoned, instead the RSM closes the Reynolds-averaged Navier-Stokes equations by solving transport equations for the Reynolds stresses together with an equation for the dissipation rate. For a 2-D and 3-D situation, respectively five and seven additional equations have to be solved. In general, the increase in computational expenses using RSM is not justified, unless used in situations where anisotropy or turbulence has a dominant effect on flows (Ansys, 2009a).

2.3.6 Near-wall treatment

Turbulence models are valid for turbulent flow regions; characteristic for these flows is that inertia forces are dominant. In regions near walls, local Reynolds numbers will be low and viscous effects important. For this purpose special treatment is needed with respect to near-wall treatment. Traditionally, near-wall treatment can be subdivided into two categories: the wall function approach and the near-wall modeling approach (Figure 2-5). When the first approach is used, the viscous-affected region is not resolved. Near-wall modeling on the other hand, resolves the flow all the way down to the wall; hence the turbulence model used should be valid throughout the near-wall region.

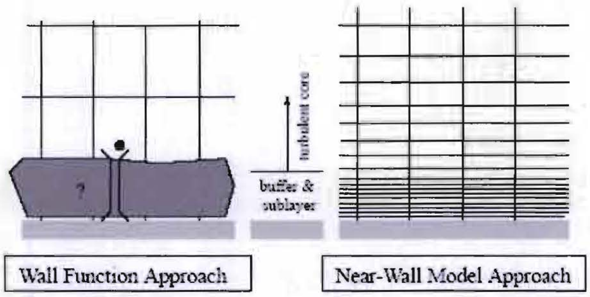

Figure 2-5: Subdivision of near-wall treatment methods in Ansys (2009a).

Low-Re-modeling

The preferred near-wall-treatment-method for near-wall flow and heat transfer is enhanced wall treatment which allows for the addition of pressure gradient and thermal effects (only if the energy equation is enabled) in the CFD model (Casey and Wintergerste, 2000). The restriction of near-wall modeling is that the near-wall mesh must be sufficiently fine. This condition can be represented by the y^+ value, a dimensionless wall coordinate defined by:

$$y^+ = \frac{\rho \cdot u_\tau \cdot y_p}{\mu}, \qquad \text{(Eq. 2.6)}$$

where ρ is the fluid density, u_τ is the friction velocity in wall functions, y_p is the distance to the center of the wall-adjacent cell, and μ the dynamic molecular viscosity. When enhanced wall treatment is applied preferably $y^+ \approx 1$, if this cannot be realized y^+ should at least be < 4-5 so that the center of the wall-adjacent cell y_p is well inside the linear sub-layer (Figure 2-6) where the viscous effects dominate the flow (Casey and Wintergerste, 2000; Ansys, 2009a).

Standard wall function

Similar to low-Re-number modeling, the use of standard wall functions is also restricted. To be valid, the center of the wall-adjacent cell y_p should be situated in the log-layer $30 < y^+ < 500$ (Ansys, 2009a), where the inertia forces are dominant. Values of y^+ close to, yet above, 30 are most desirable when applying the standard wall function.

Obtaining the desired y^+ value is an iterative process which can be time-consuming. The time needed to fit the y^+ values within the preferred linear sub-layer or log-layer depends mainly on the user's experience. In between these two layers we speak of the buffer layer, $5 < y^+ < 30$. It is called the buffer layer because neither the linear wind speed profile (valid in the linear sub-layer), nor the logarithmic wind speed profile (valid in the log-layer) is valid. Within this layer less accurate model predictions can be expected. This is observed when comparing the theoretical wind speed profiles and experimental data for the buffer layer in Figure 2-6. It should be noted that when the y^+ value is situated in the buffer-layer ($5 < y^+ < 30$), the CFD code Ansys (2009a) automatically switches from log-law to linear-law when $y^+ < 11.225$.

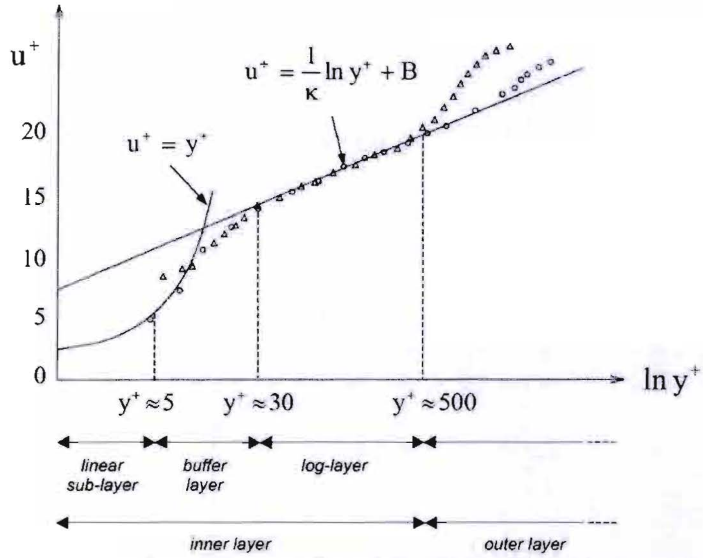

Figure 2-6: The turbulent layer adjacent to a solid wall. The solid lines represent the linear wind speed profile and the logarithmic profile. The open dots and squared represent experimental data. U^+ is the dimensionless fluid speed. (Adapted figure from Ansys (2009a))

2.3.7 Thermal effects

Heat transfer can occur in three ways: conduction, convection, and radiation. All of which can be included in a CFD simulation. To do so, Ansys (2009b) allows for different wall boundary conditions: fixed heat flux, fixed temperature, convective heat transfer, external radiation heat transfer, combined external radiation, and convection heat transfer. When a 'fixed temperature' boundary condition is applied, the heat flux from wall to fluid is computed by multiplying the temperature difference by the heat transfer coefficient. The fluid side heat transfer coefficient is calculated based on the local flow field conditions, such as turbulence, temperature, and wind speed profile (Ansys, 2009a).

Including buoyancy effects in the CFD model

Besides forced convection flows, also buoyancy-driven flows and mixed-convection flows can be modeled by Ansys, when a non-zero gravity force is set in the CFD model combined with a non-isothermal flow. Generation of turbulent kinetic energy as a result of buoyancy is by default included in the k equation (Ansys, 2009b). Enabling the "full thermal effect" option in Ansys (2009b) also includes the influence of buoyancy effects on ε. This option is available for all k-ε turbulence models and the RSM.

Richardson number

With respect to wind flow around buildings, the bulk Richardson number can be adopted to derive whether a flow is either wind-induced or buoyancy-driven. The Richardson number is defined as the ratio of the Grashoff and squared Reynolds number, i.e. a dimensionless number that indicates the ratio of potential to kinetic energy and is defined as:

$$Ri = \frac{Gr}{Re^2} = \frac{\beta g H(T_{wall}-T_{ref})}{U_{ref}^2}, \qquad \text{(Eq. 2.7)}$$

where β is the coefficient of thermal expansion, g the acceleration due to gravity, H the obstacle height, T_{wall} the mean wall temperature, T_{ref} the ambient temperature, and U_{ref} the reference wind speed at a height of 10 meters measured upstream of the building model (unless specifically indicated otherwise). When $Gr/Re^2 \approx 1$ the motion is induced by both buoyancy and wind, $Gr/Re^2 >> 1$ indicates that buoyancy effects are more significant, and $Gr/Re^2 << 1$ indicates a wind-induced flow.

Boussinesq model

When heat is added to a fluid, and fluid density varies with temperature, a force as a result of gravity acts on the fluid based on density differences. Flows induced in such a way are called buoyancy-driven flow or natural convection. If forced convection also plays a part, one speaks of mixed-convection. For faster convergence the Boussinesq approach can be used for many flows. In this approach, all fluid densities are treated as a constant, except for the buoyancy term in the momentum equation (Ansys, 2009a):

$$(\rho - \rho_0)g \approx -\rho_0\beta(T - T_o)g, \qquad \text{(Eq. 2.8)}$$

where $\rho_0$is the constant density of the flow, T_o is the operating temperature, and β is the thermal expansion coefficient. This approximation is accurate as long as variation in fluid density, i.e. the temperature difference is small. The approach is valid when $\beta \cdot (T - T_0) \ll 1$.

2.3.8 IB and BFG method

This paragraph describes two grid-generation approaches: the Body Fitted Grid (BFG) and Immersed Boundary (IB) method. The BFG method has been adopted by conventional CFD codes, the IB method however has also been around for quite some time. The first reference to it was made by Peskin (1972) who studied the blood flow in the human body and conducted a simulation on a Cartesian grid which did not conform to the geometry of the hart. Especially in the last fifteen years, popularity of this method has risen tremendously in the field of CFD (Iaccarino and Mittal, 2005).

When the BFG method is applied, a structured or unstructured grid is adopted that conforms to the geometry. Essentially two steps can be defined towards making a mesh. Firstly, the surface representation, i.e. the geometry, is covered by a surface mesh, after which volume meshes are built to create the computational domain. Local grid refinement is realized by refining the surface mesh where required. For more complex geometries the grid is often divided into sub domains to obtain the desired grid quality and resolution.

The IB methods refer to methods that use immersed boundaries of which the grid does not conform to the geometry of these boundaries (Iaccarino and Mittal, 2005; Iaccarino and Moreau, 2006). Consider a structured Cartesian grid which is created without regard to the implemented body geometry. Body boundaries would cut through this structured grid altering the cell shape near the boundaries. Grid refinement is realized by locally increasing grid resolution, thus introducing hanging nodes. In 2-D these hanging nodes occur when one of the cells sharing a face is divided and the other is not, an example is encircled in Figure 2-7b. The last step is to refine the grid to avoid large jumps in cell size. The principle of both methods is depicted in Figure 2-7.

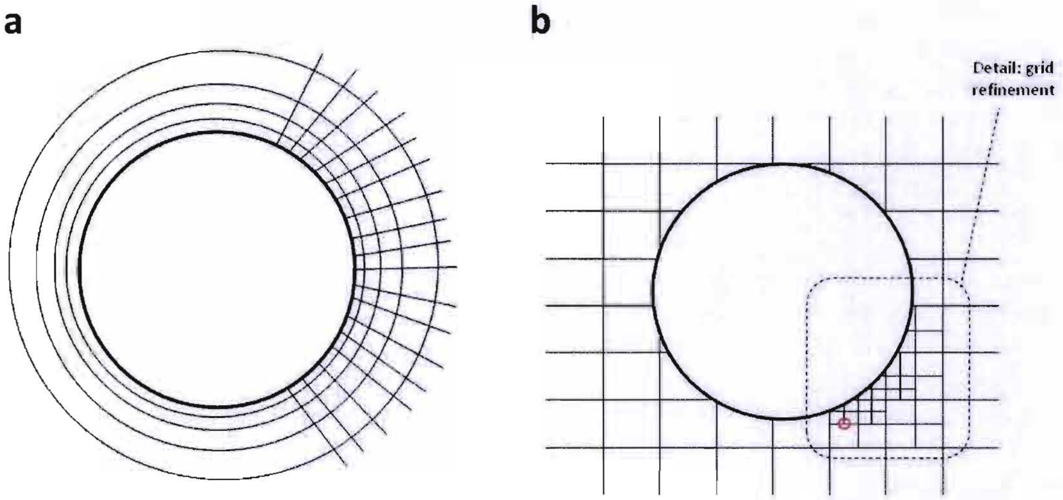

Figure 2-7: Principle of a structured 2-D grid around a cylinder using the a) BFG; b) IB method.

Below, the most important advantages and disadvantages of both methods are summarized based on the papers of Iaccarino and Mittal (2005) and Iaccarino and Moreau (2006).

BFG has a number of advantages as it is the conventionally used method: a lot of knowledge is available, it is integrated in all commercial CFD codes, a wide range of strong preprocessors is available, and the designer has full control over mesh-generation. The largest disadvantage is that creating grids and making local grid refinements is extremely time-consuming when modeling complex geometries. Hands-on-time can be reduced when semi-automating this process; for this purpose so called journal files, which contain command lines, can be adopted in Ansys (2009b).

The primary advantages of the IB method are the ability to handle complex geometries created in a CAD environment and the functionality of easy grid refinement. In addition, easy to use CAD software plug-ins are available making CFD more accessible for the commercial sector. Most significant disadvantages are that imposing boundary conditions is not straightforward and that the effect on the accuracy and properties of numerical schemes are not obvious; this still needs additional research (Iaccarino and Mittal, 2005).

3 Validation studies

In the literature study some general information with respect to urban CFD models, the UHI effect and implementation of thermal effects in CFD models was presented. The gathered information is then used to validate the aspects: wind flow pattern, wind speed, and thermal buoyancy to ensure reliability of the CFD model. Due to the complexity of the case study city, three validation cases have been adopted. In the first case, wind flow and wind speed are validated. In addition, this case is used to determine how coarse the computational grid can be whilst still providing results with the desired accuracy. Determining the maximum coarseness is important with respect to limiting the number of grid cells and required computational time. The second case aims to validate the buoyancy effect, i.e. change of the wind flow pattern and temperature field due to temperature differences between the air, building surfaces, and other surfaces. In the third case, knowledge obtained from the previous two cases is used to validate the CFD model for a 3-D case.

For each validation case the same approach was adopted: 1) description of the validation case, 2) definition of simulation characteristics, i.e. conduct grid-sensitivity analysis and study the influence of different turbulence models, and 3) comparison of simulation and measurement results.

3.1 Case study for validation: 2-D wind flow pattern and wind speed

3.1.1 Description of validation case

Simplified, an urban area can be characterized as an array of buildings connected by streets. When applying CFD models on an urban scale, prediction of general wind flow in and around street canyons and clusters of buildings is more significant than predicting very fine scales of turbulence in the vicinity of single buildings. Therefore, the first step in this study is introducing a relatively simple 2-D case in which the predicted flow pattern and wind speed in a street canyon are validated against wind tunnel experiments as described by Kovar-Panskus et al. (2002a). This paper provides results of wind tunnel measurements of a logarithmic boundary layer flow across five configurations of urban street canyons which are characterized by the ratio between canyon width W and height H (Figure 3-1). This ratio was varied between W/H = 0.3 and W/H = 2.0, representing steep to shallow street canyons. Due to limitations of the experimental set-up however, only the configurations with ratio W/H = 2.0, 1.0, and 0.7 were deemed useful for validation purposes.

The height of the canyon model was H = 0.106 m and fits a scale of 1:200, thus giving it an approximate actual building height of 20 m. The neutrally stratified approach conditions were; boundary layer height δ = 737 mm, aerodynamic roughness length y_0 = 0.3 mm, and friction velocity u^* = 0.4 m/s. The ground and cavity walls were roughened using 'Lego boards'. Flow measurements were taken with pulsed-wire-anemometer which simultaneously measured wind speed and direction. Furthermore, the experiment was set-up such that the flow over the street canyon can be considered 2-D. The authors concluded that two-dimensionality was established for the central 60% of the spanwise length of the cavity. In this region wind speed in the direction of the flow was within ±5% of the mean and turbulence intensity even within ±3% of the mean. A maximum deviation in the flow direction from the XZ-plane of 3° was obtained. A schematic representation of the wind tunnel experiment is depicted in Figure 3-1.

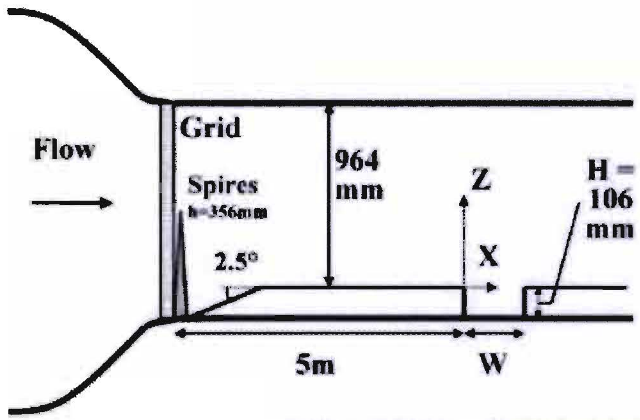

Figure 3-1: Schematic representation of wind tunnel and canyon model (Kovar-Panskus et al., 2002a).

CFD simulations are ideally performed under the same conditions as the wind tunnel experiment. Figure 3-2 shows the measured and simulated boundary layer mean wind speed and turbulent kinetic energy in the wind tunnel before separation at the street canyon. The profiles used for the simulations are based on the measured y_0, u^*, u', and w' values.

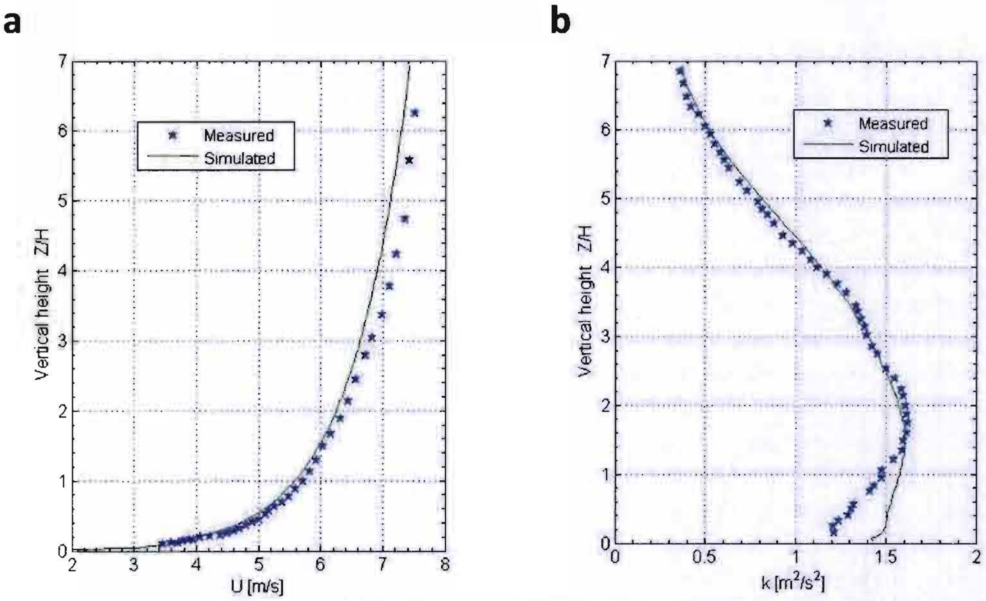

Figure 3-2: Comparison of measured and simulated boundary layer a) mean wind speed profile; b) turbulent kinetic energy.

The simulated mean wind speed profile before separation at the cavity shows good results when compared to the measured values, especially in the near-ground region Z/H < 1.0 the profiles match very well. The maximum deviation of 0.27 m/s at height Z/H = 4.8 is deemed acceptable. The simulated turbulent kinetic energy is overestimated for heights Z/H < 2.0; above Z/H = 2.0 the profiles match very well.

3.1.2 Simulation characteristics

In this paragraph, the following simulation characteristics are assessed: grid independence of the solution and influence of the turbulence model. The results of this review will form the basis for the CFD model that will be used to compare the simulation results with the experimental wind tunnel measurements.

Grid-sensitivity analysis

A grid-sensitivity analysis was conducted for the W/H = 1.0 street canyon configuration to obtain a grid-independent solution. In addition, this analysis is used to determine how coarse the computational grid can be whilst providing results with the desired accuracy. The W/H = 1.0 configuration was used because additional wind speed measurements inside the street canyon are available for this configuration.

The reference grid resolution is equal to 10 cells per building side (Franke et al., 2007; Tominaga et al., 2008), which corresponds to 3,700 cells in the computational domain. As recommended by Franke et al. (2004), this grid was structurally refined three times whilst the ratio of cells in consecutive grids is 2.25. In addition, two coarser grids were created. The reference grid and the street canyon details are shown in Figure 3-3. Except for the mesh resolution, no modifications were made to the grid and model. Important grid characteristics are: applying a structured grid, equidistant cells in the street canyon, maximum cell ratio in other parts of the domain 1.05, and the number of cells varies between 688 and 42,722. These characteristics were chosen keeping in mind the desired grid build-up for the case study city Rotterdam. Furthermore, the size of the computational domain is based on the street canyon depth and recommendations by Franke et al. (2007). In the streamwise direction the domain stretches 1H upstream and 15H for the wake, height of the domain is 8H to allow for a fully developed boundary layer flow. For determining the appropriate approach flow domain length, four distances to the street canyon were tested; 0.2H, 0.5H, 1H, and 5H. The results of this comparison are presented in Appendix B. For turbulence modeling the standard k-ε model was used. The y^+ values for the different mesh resolution are described in Table 3-1. Other model characteristics are as presented in Table 3-2.

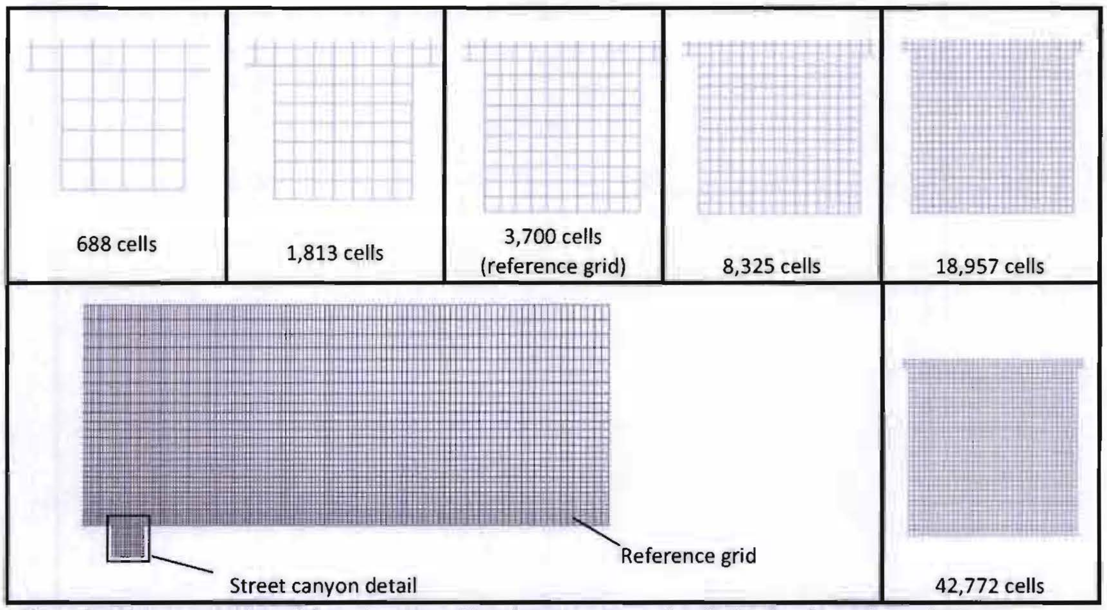

Figure 3-3: Representation of the reference grid and street canyon details for the six mesh resolutions, W/H = 1.0.

Grid independence is assessed by comparing the measured and simulated wind speed and wind flow patterns in the street canyon. Figure 3-4 and Figure 3-5 depict the mean wind speed vectors and flow patterns for the six mesh resolutions. For all the grids the general flow compares well to the measurements. Exception is the grid with 688 cells, which is unable to predict the upward flow in the top left part of the street canyon and also underestimates the mean wind speed. It can be concluded from these figures that refinements of the grid with 1,813 cells do not further improve prediction of the wind flow pattern and mean wind speed significantly.

Table 3-1: y+ values for the six grid resolutions.

Number of cells	y^+ value	Number of cells	y^+ value
688	70 - 240	8,325	8 - 105
1,813	40 - 150	18,957	3 - 65
3,700	36 - 130	42,772	3 - 52

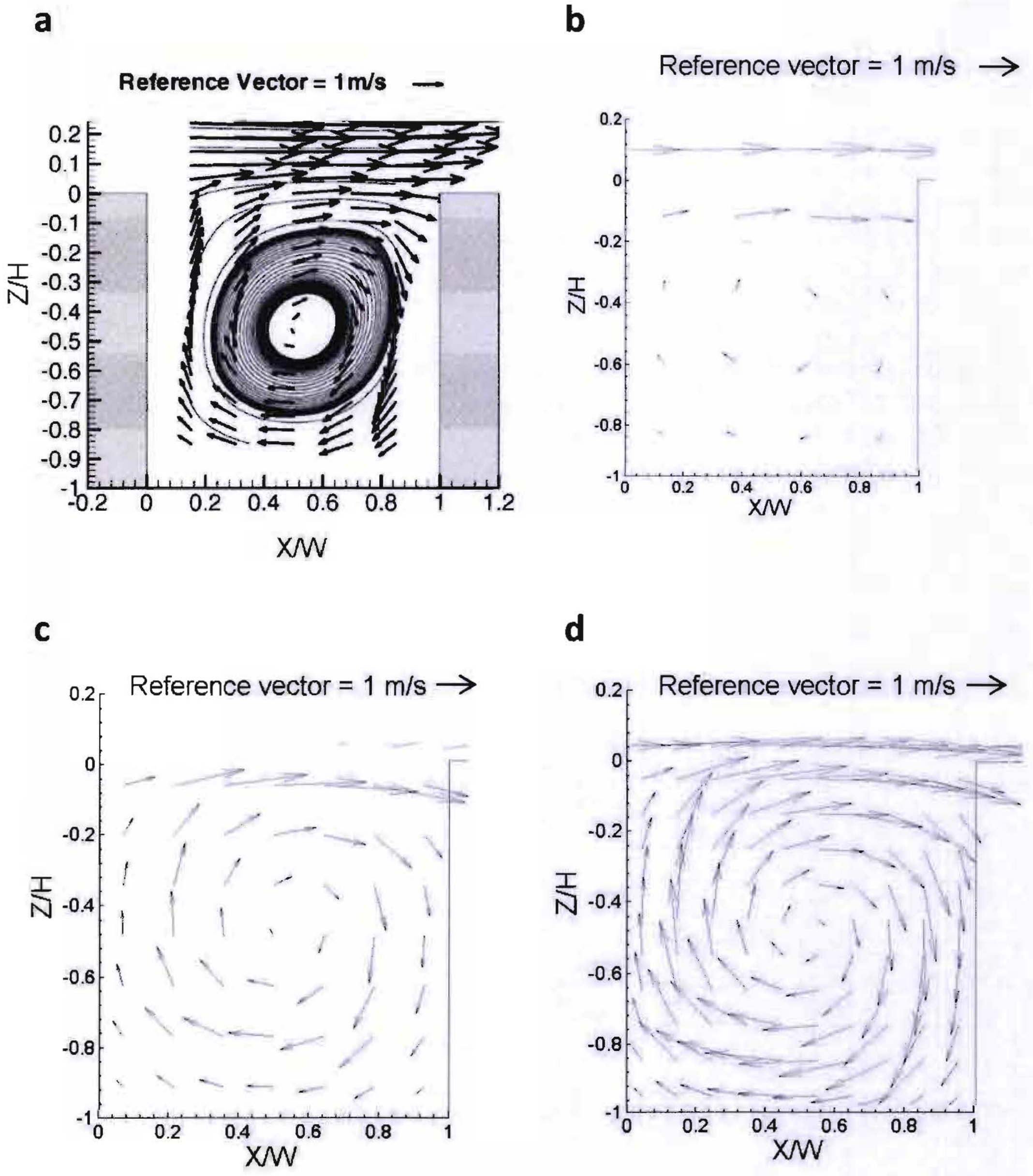

Figure 3-4: Mean wind speed vectors for W/H = 1.0, a) measured; b) 688 cells; c) 1,813 cells; d) 3,700 cells (reference grid).

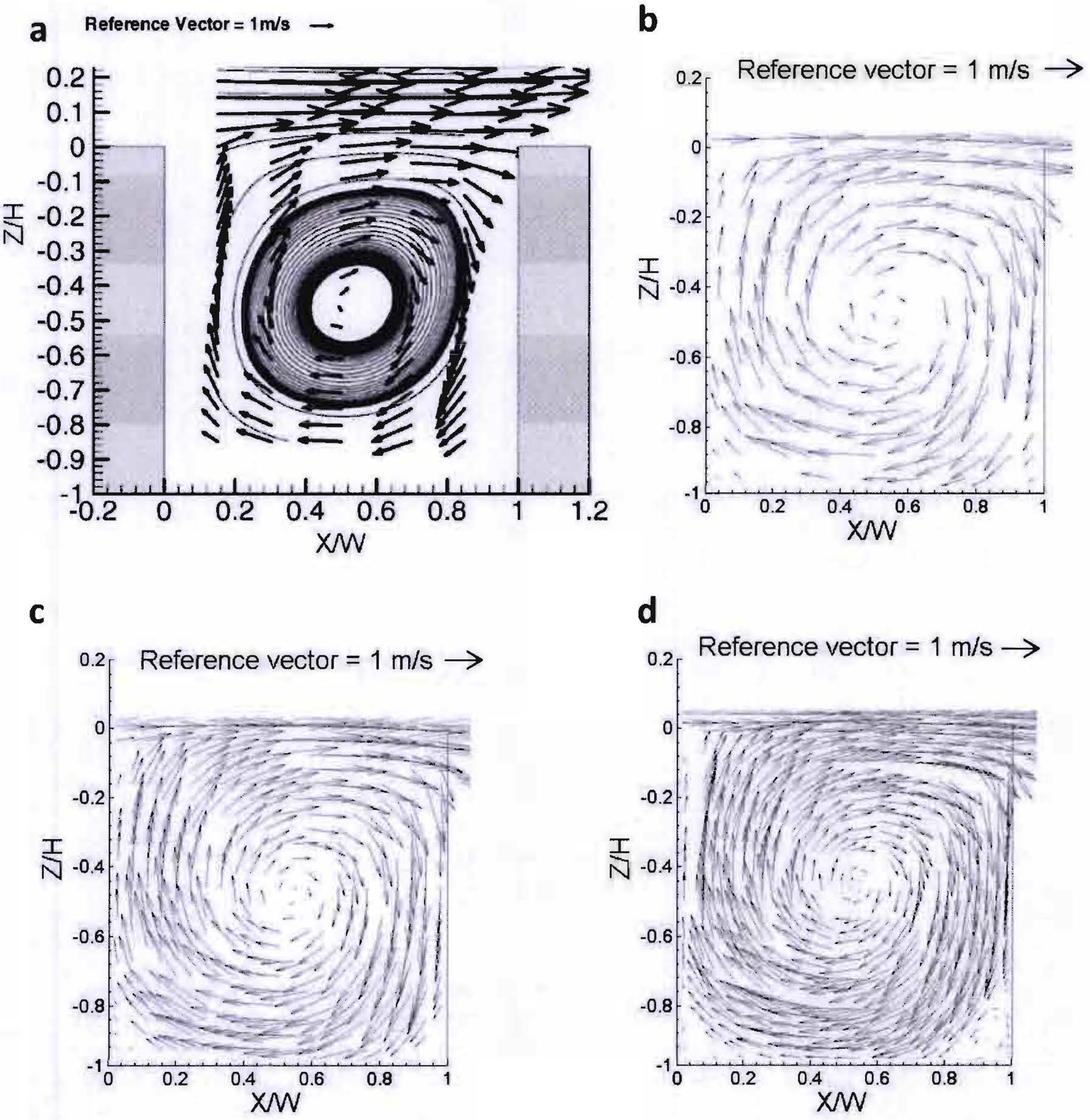

Figure 3-5 (Figure 3-4 continued): Mean wind speed vectors for W/H = 1.0, a) measured; b) 8,325 cells; c) 18,957 cells; d) 42,772 cells.

Figure 3-6 shows the comparison of the measured and predicted dominant vortex center. It can be seen that none of the grids is able to exactly predict the location of the vortex center. However, the grid with 8,325 cells and the two consecutively refined grids are able to make the most accurate prediction of the vortex center's location. The three grids predict about the same deviation with respect to the measurements.

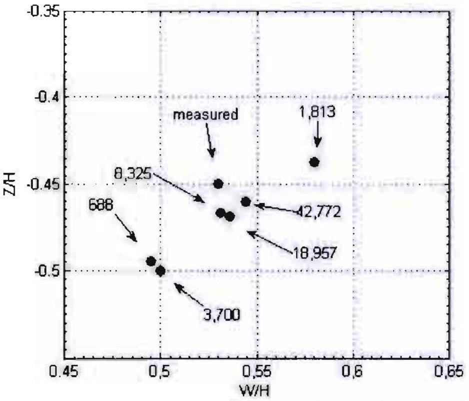

Figure 3-6: Comparison of measured and predicted vortex center in the W/H = 1.0 street canyon for the six grid resolutions.

As a quantitative comparison, the Root Mean Squared Error (RMSE) was calculated for 15 points in the street canyon. The RMSE is a frequently-used measure for the difference between values predicted by a model or an estimator and measured values. RMSE is a good measure of precision and is defined by:

$$RMSE = \sqrt{\sum_{i=1}^{n} \frac{(x_{measured,i} - x_{simulated,i})^2}{n}} \qquad \text{(Eq. 3.1)}$$

In which:

RMSE = Root Mean Squared Error [m/s]
$x_{measured}$ = Measured U component wind speed [m/s]
$x_{simulated}$ = Simulated U component wind speed [m/s]
n = Number of compared points [-]

As depicted in Figure 3-7, the simulation results are strongly affected by the grid resolution. Especially the coarsest grid which only has 688 cells shows relative bad results with a RMSE of 0.452 m/s, over twice as high as the succeeding grid. In turn, a lower RMSE is obtained when applying a grid with 8,325 cells when compared to the reference grid. Only a very small difference is found between the grid with 8,325 cells and the two consecutive refined grids. Based on the figure below it can be concluded that grid independence is not obtained. However, the results for the grid with 8,325 cells are deemed sufficient for the purpose of this validation.

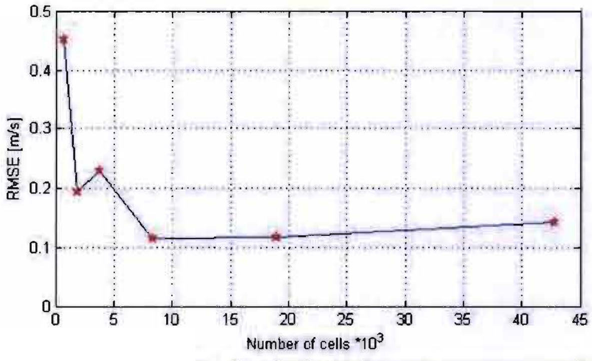

Figure 3-7: RMSE over 15 points in the W/H = 1.0 street canyon for the six mesh resolutions.

The last part of the grid-sensitivity analysis consists of comparing the measured and predicted U component wind speed on five vertical lines in the street canyon (Figure 3-9b). Figure 3-8 and Figure 3-9 show that all the meshes, except for the coarsest, are in good agreement with the measurements, especially in the center region 0.2 < Z/H < 0.8 of the street canyon. An exception is the grid with 1,813 cells, which less accurately predicts the wind speed profile at the X/W = 0.9 location. Taking a closer look at the profiles in the top and the bottom region of the canyon shows that the grids with 18,957 and 42,772 cells are able to predict the velocities in this region more accurately than the coarser meshes. Based on this figure it can be concluded that a grid-independent solution was not obtained. However, using a grid with 18,957 cells provides the desired results.

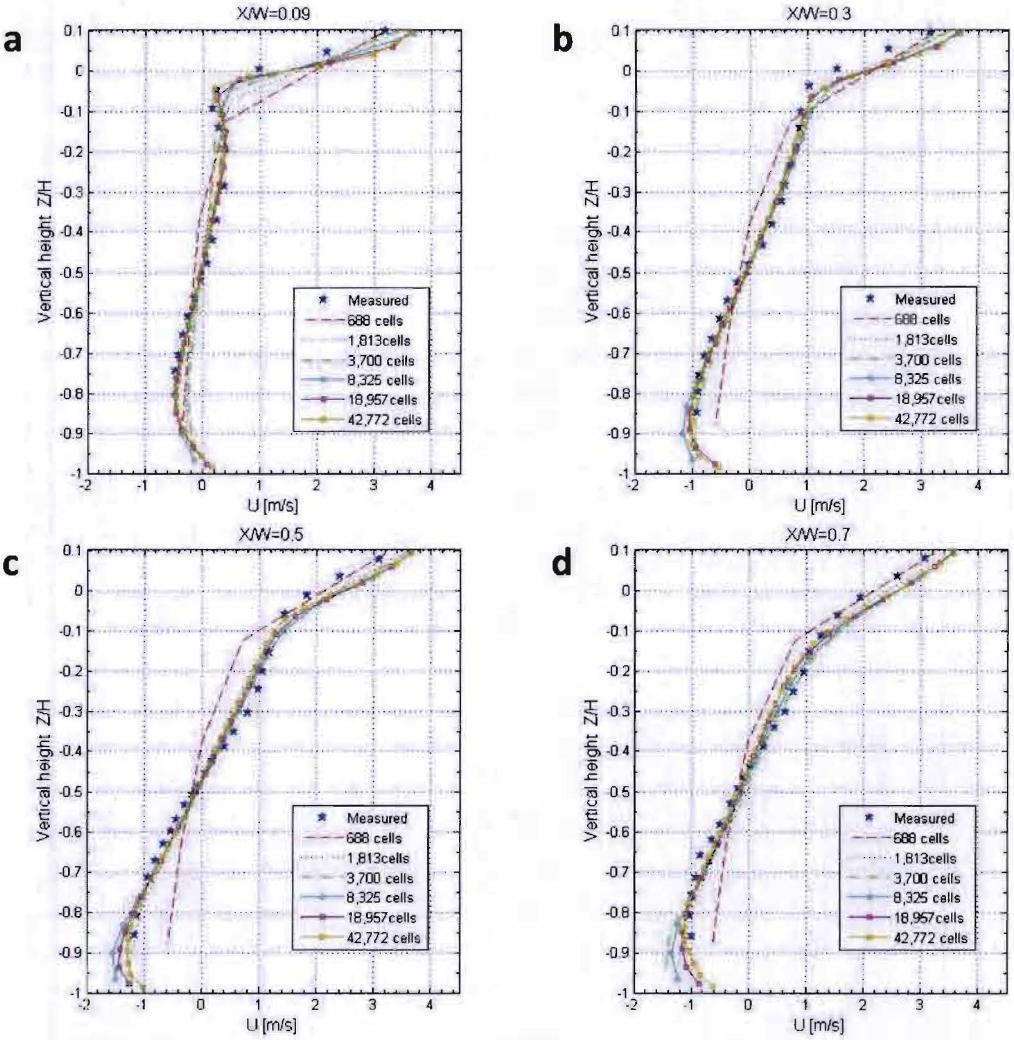

Figure 3-8: Comparison of U component wind speed distribution in the W/H = 1.0 street canyon on five vertical lines: a) X/W = 0.09; b) X/W = 0.3; c) X/W = 0.5; d) X/W = 0.7.

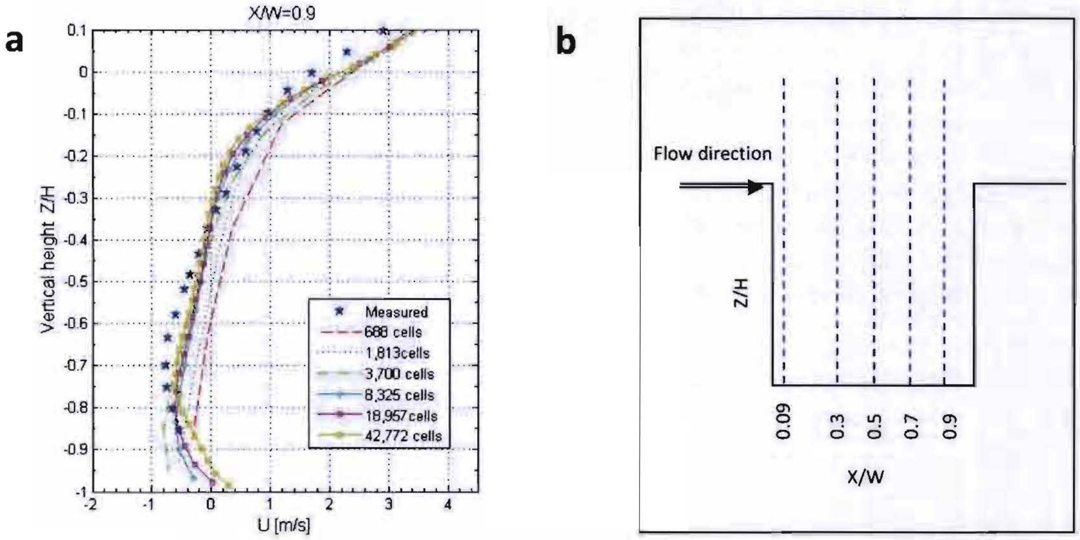

Figure 3-9 (Figure 3-8 continued): Comparison of U component wind speed distribution in the W/H = 1.0 street canyon on five vertical lines: a) X/W = 0.9; b) schematic representation of the five vertical lines.

Turbulence model

In addition to a grid-sensitivity analysis to obtain grid-independent CFD simulation results, different turbulence models are tested to assess the influence of these turbulence models. The standard k-ε model, the realizable k-ε model, the RNG k-ε model, and the Reynolds Stress equation Model with Linear Pressure-Strain (further referred to as RSM model) are assessed. Since the performance of the turbulence models is also depend on the grid resolution, the RMSE (Eq. 3.1) of the turbulence models for three grids resolutions are calculated (Figure 3-10). For assessing the turbulence models the W/H = 1.0 street canyon configuration is used.

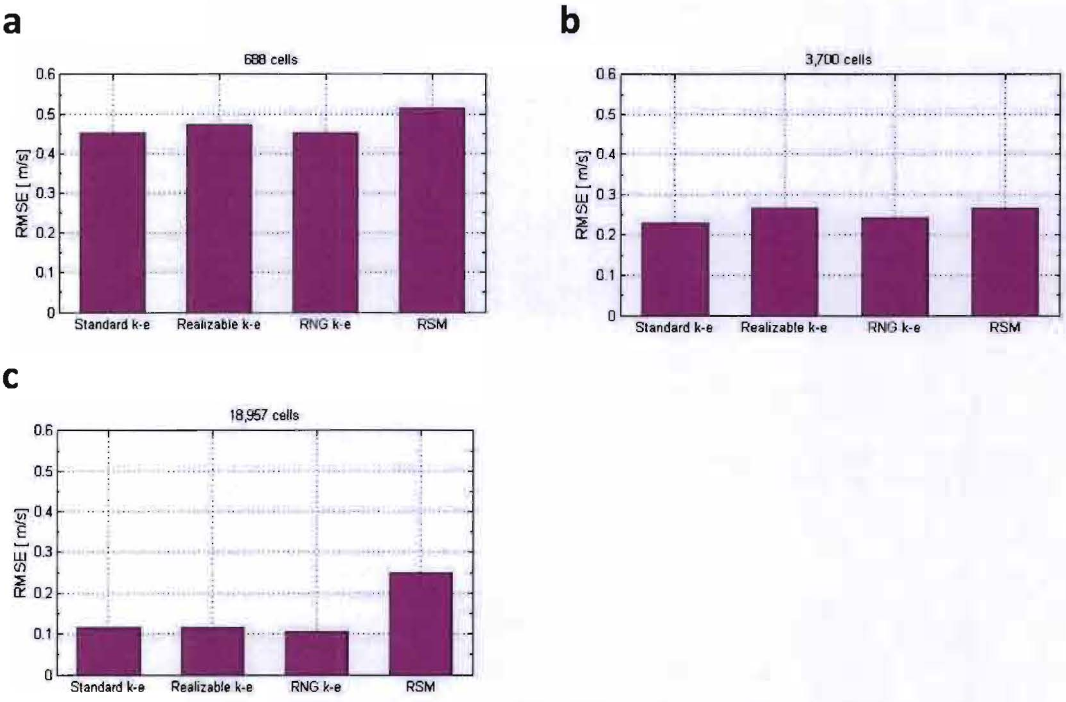

Figure 3-10: Comparison of the RMSE over 15 points in the W/H = 1.0 street canyon for the four turbulence models, a) 688 cells; b) 3,700 cells; c) 18,957 cells.

The figure above confirms that the applicability of turbulence models is grid dependent. For the two coarsest grids the differences are relatively small. For the grid with 688 cells the difference between the standard k-ε model and the RGN k-ε model is even negligible. For the reference grid with 3,700 cells the standard k-ε model seems to produce the most accurate results; noting that the maximum difference in RMSE with the other turbulence models is only 0.038 m/s. As for the finest grid tested; the differences are again very small, with an exception for the RSM model. Since the finest of the mentioned grids will be used for validating the CFD model, an additional comparison was made showing the U component wind speed distribution in the canyon at the vertical line X/W = 0.9 (Figure 3-11). This downstream location is chosen because at this line a relatively large difference occurred when conducting the grid-sensitivity analysis. The figure below shows that not only the RMSE, but also the wind speed profile prediction in the canyon are very similar for the three k-ε turbulence models. Based on these two figures either the standard k-ε model, realizable k-ε model, or RNG k-ε model should be used.

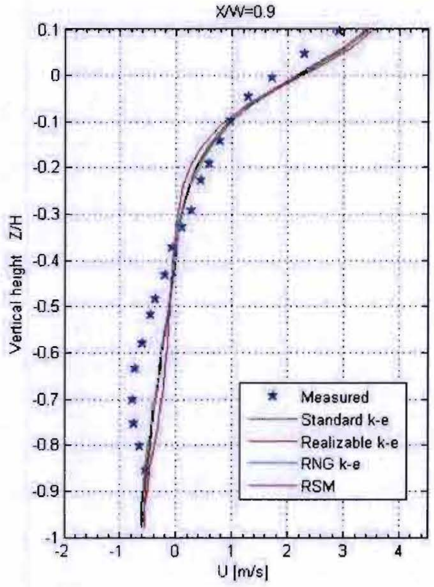

Figure 3-11: Comparison U component wind speed distribution in the W/H = 1.0 street canyon for four turbulence models, 18,957 cells.

Concluding remarks

Six mesh resolutions and four turbulence models were assessed to determine the appropriate simulation characteristics for the validation case: 2-D wind flow pattern and wind speed. To obtain a grid-independent solution, wind flow pattern and mean wind speed in the street canyon were assessed. In this assessment, applicability and accuracy of the applied wall functions depends on the y^+ values. Y^+ values for the coarsest three meshes were in the range 36-240; this is well within the preferred limits for standard wall function approach as suggested by Ansys (2009a). The finer meshes only complied with the upper limit for y^+, with values of respectively 105, 65, and 52 for the meshes with 15, 23, and 34 cells. The lower y^+ values were too low, with values of respectively 8, 3, and 3. These low values occurred in the bottom left en right of the canyon, with a decreased accuracy in the near-wall region as a result. Despite these low y^+ values, the three finest meshes produce more accurate result than the low resolution grids.

Based on the presented results in this paragraph, a grid with 18,957 cells will be adopted for this validation case. This grid resolution is two steps finer than the reference grid which is based on the recommended 10 cells per building side. Also, the performance of four turbulence models was assessed. For this, not only the grid with 18,957 cells was studied, but also two coarser grids to gain insight in the grid dependence of turbulence models. Based on the observation it can be concluded that the difference in performance is negligible between the standard k-ε model, the realizable k-ε model, and the RNG k- ε model, either one can be adopted for this validation case. However, the RNG k- ε model is slightly better in predicting the downstream location of the dominant vortex (Figure 3-6 and Figure 3-12) and will therefore be used in this validation case.

3.1.3 Comparison of simulation and measurements

The simulation results will be compared on three aspects with the measurement data from the wind tunnel experiments; wind flow pattern, wind speed, and location of the vortex center. Based on the grid-sensitivity analysis and turbulence model assessment, a grid with 18,957 cells and the RNG k-ε model are used to run the 2-D Reynolds-Averaged Navier-Stokes (RANS) simulations. Table 3-2 describes the applied grid and other CFD model characteristics.

Table 3-2: Grid and model characteristics for validation case.

Feature	Description
Grid	Structured grid, 18,957 cells, equidistant cells in street canyon, minimal cell size $4.61 \cdot 10^{-3}$ [m], maximum cell ratio in other parts of domain 1.05
Domain	Height 8H, downstream domain 1H, upstream domain 15H; where H = 0.106 [m]
Solver	Steady 2-D RANS
Convergence criteria	Scaled residuals for, continuity: $1 \cdot 10^{-11}$, velocities: $1 \cdot 10^{-11}$, k: $\cdot 10^{-11}$, ε: $1 \cdot 10^{-11}$
Turbulence model	RNG k-ε model; $k = \frac{1}{2} \cdot (u' + 2v'^2)$, $\varepsilon = \frac{U^{*3}}{(\kappa \cdot (y + y_o))}$, both profiles are based on measured values
Discretization	Pressure velocity coupling: scheme (SIMPLE) Spatial Discretization: Gradient (Least Squares Cell Based); Pressure (2^{nd} Order); Momentum, Turbulent Kinetic Energy, and Turbulent Dissipation Rate (all three 2^{nd} Order Upwind)
Near-wall modeling	Standard wall function, Case W/H=0.7: $1.1 < y^+ < 63.1$ Case W/H=1.0: $3.0 < y^+ < 65.2$ Case W/H=2.0: $1.5 < y^+ < 80.1$
Boundary conditions	
Inlet	Adiabatic, user-defined profiles adopted for k, ε and U, where $U = \frac{u^*}{\kappa} \cdot \ln\left(\frac{y + y_0}{y_0}\right)$
Outlet	Adiabatic, pressure outlet; user-defined profiles adopted for k and ε
Canyon walls	Adiabatic, no-slip, roughness height $k_s = 0$ [m] (Eq. 2.1)
Bottom	Adiabatic, no-slip, roughness height $k_s = 2{,}30 \cdot 10^{-3}$ [m], $C_s = 1.27$ [-] (Eq. 2.1)
Top	Symmetry

In Figure 3-12 the measured and predicted dominant vortex locations are depicted. This figure is derived from Figure 3-13, Figure 3-14, and Figure 3-15, which show that the height of the dominant vortex center is predicted to be lower than actually measured. Expected is that this is a result of the predicted W component wind speed near the windward facing wall of the street canyon being lower than measured. As a result of the underestimation of the wind speed, it is likely that the weaker downward flow decreases pressure on the street canyon floor, causing the predicted vortex center to shift downwards. Since recording the pressure field and measuring the W component wind speed near the windward facing wall was not included in the measurements, no definitive conclusion can be drawn. Figure 3-16 and Figure 3-17 however, do confirm that the predicted U component wind speed below the vortex center is underestimated, indirectly confirming the expected difference between the predicted and measured W component wind speed. Looking at the different street canyon configurations, it can be observed that the CFD model is least accurate when predicting the vortex center for steep street canyons. A difference of 0.025H is observed, which corresponds to $^1/_{40}$ of the total canyon height. The vortex center for the wide street canyon is predicted slightly more accurate than for the W/H = 1.0 street canyon.

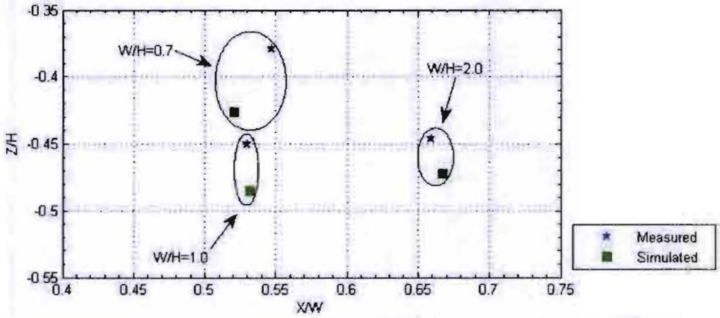

Figure 3-12: Dominant vortex location for the three street canyon configurations.

In Figure 3-13 to Figure 3-15 the air flow pattern is compared for the three street canyon configurations. These figures show that in general the simulated wind flow pattern corresponds well with the wind tunnel measurements. Measurements and predictions for the wide street canyon configuration (W/H = 2.0) are shown in Figure 3-13. In addition to a dominant vortex, a secondary vortex is predicted; this secondary vortex was also measured. When comparing the two figures it seems that the predicted secondary vortex center is too high. However, due to the limited availability of measurement data in the bottom left corner of the street canyon, this comparison is considered inconclusive. In Figure 3-15 the steep street canyon configuration is shown. It could be reasoned that besides a dominant vortex, a minor vortex appears at the bottom of the canyon. Expected is that for steeper street canyons this secondary vortex, and maybe even additional vortices, will occur.

Figure 3-13 to Figure 3-15 also show that the direction of the wind flow at the top of the canyon Z/H = 0.0 - 0.05 (see marking in Figure 3-15), is predicted to be more horizontal than observed by the measurements where a W component wind speed is also observed. The same can be concluded from Figure 3-16 and Figure 3-17, which show that the U component wind speed is structurally overestimated in this region. The largest difference for both canyon types is observed near the (windward-facing) walls. As for the wind speed profiles, the CFD model is better able to make predictions for the regular street canyon than for the wide street canyon. Despite some inaccuracies in predicting the U component wind speed, the predicted profile shape is deemed sufficiently accurate. U component wind speed distribution in the street canyon data was not available for the steep canyon (W/H = 0.7) wind tunnel configuration.

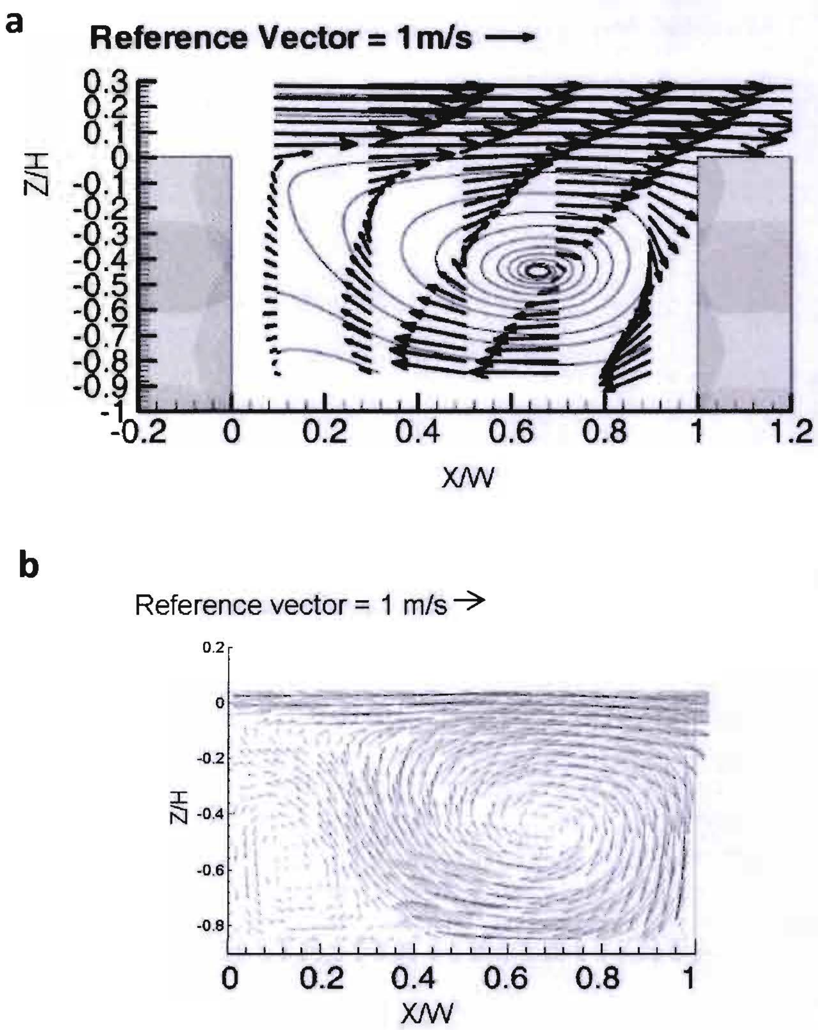

Figure 3-13: Mean wind speed vectors for W/H = 2.0, a) measured; b) simulated.

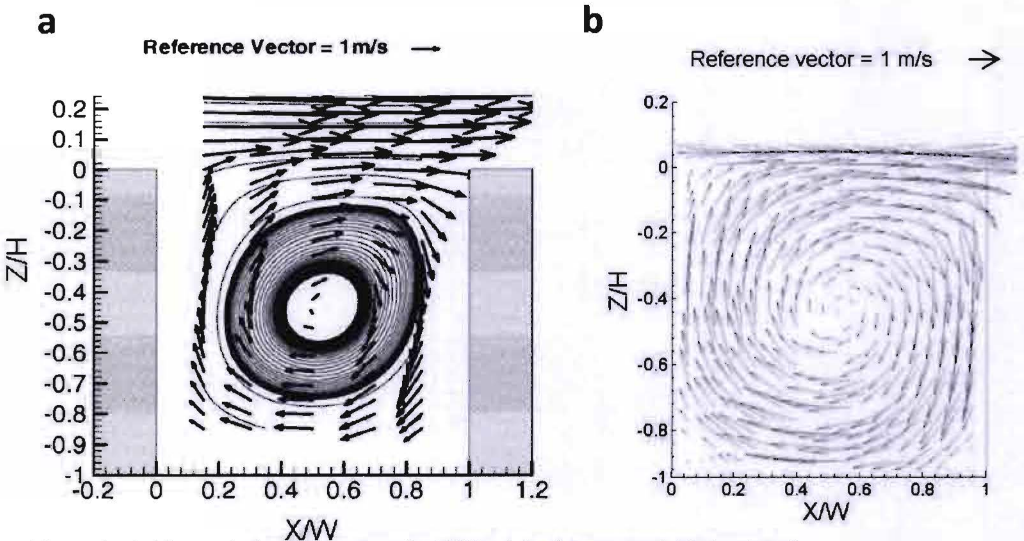

Figure 3-14: Mean wind speed vectors for W/H = 1.0, a) measured; b) simulated.

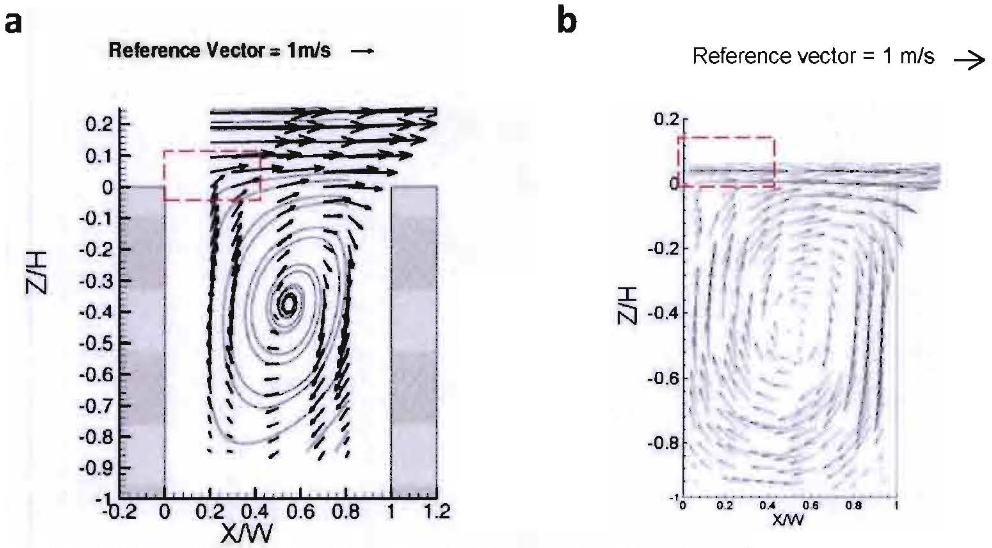

Figure 3-15: Mean wind speed vectors for W/H = 0.7, a) measured; b) simulated.

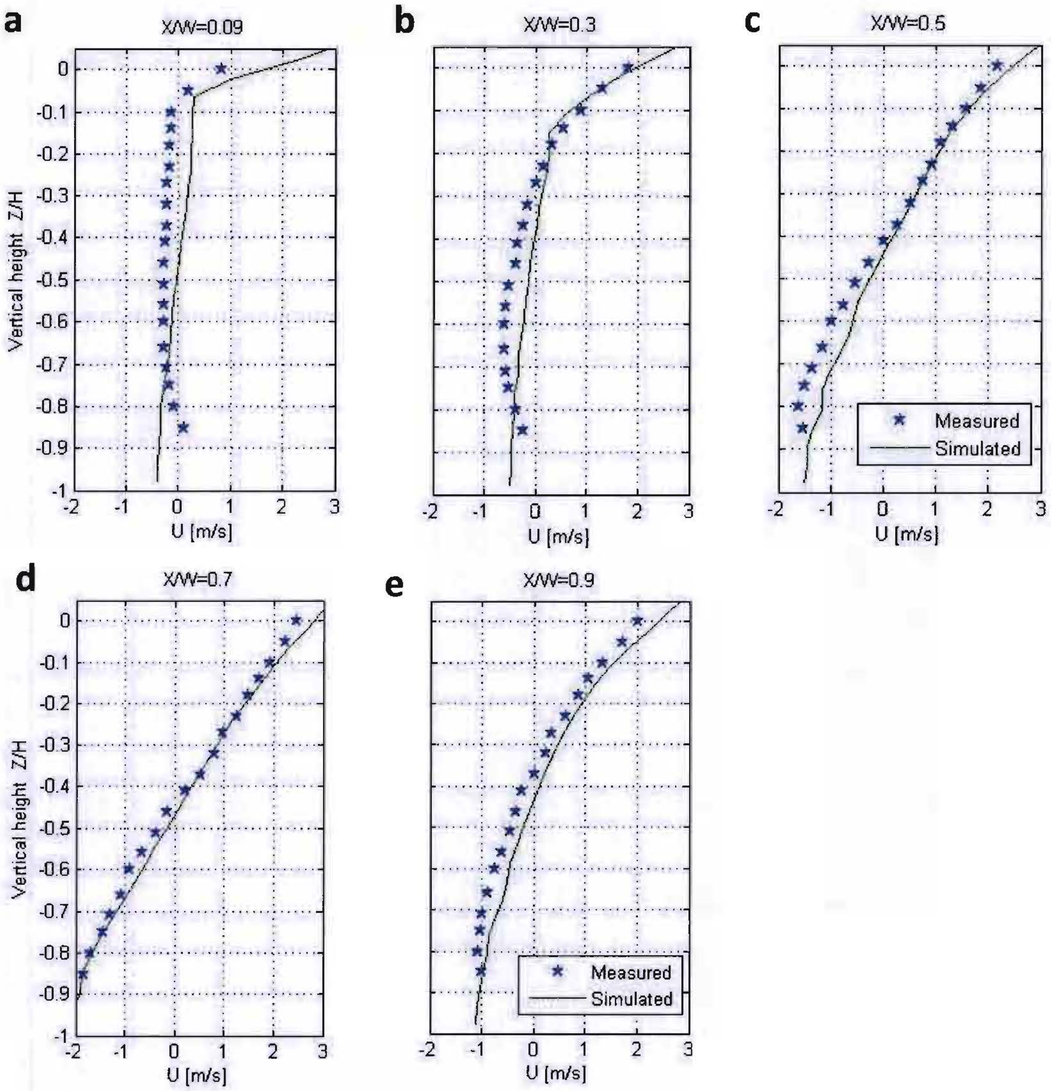

Figure 3-16: Comparison U component wind speed distribution in the W/H = 2.0 street canyon on five vertical lines: a) X/W = 0.09; b) X/W = 0.3; c) X/W = 0.5; d) X/W = 0.7; e) X/W = 0.9.

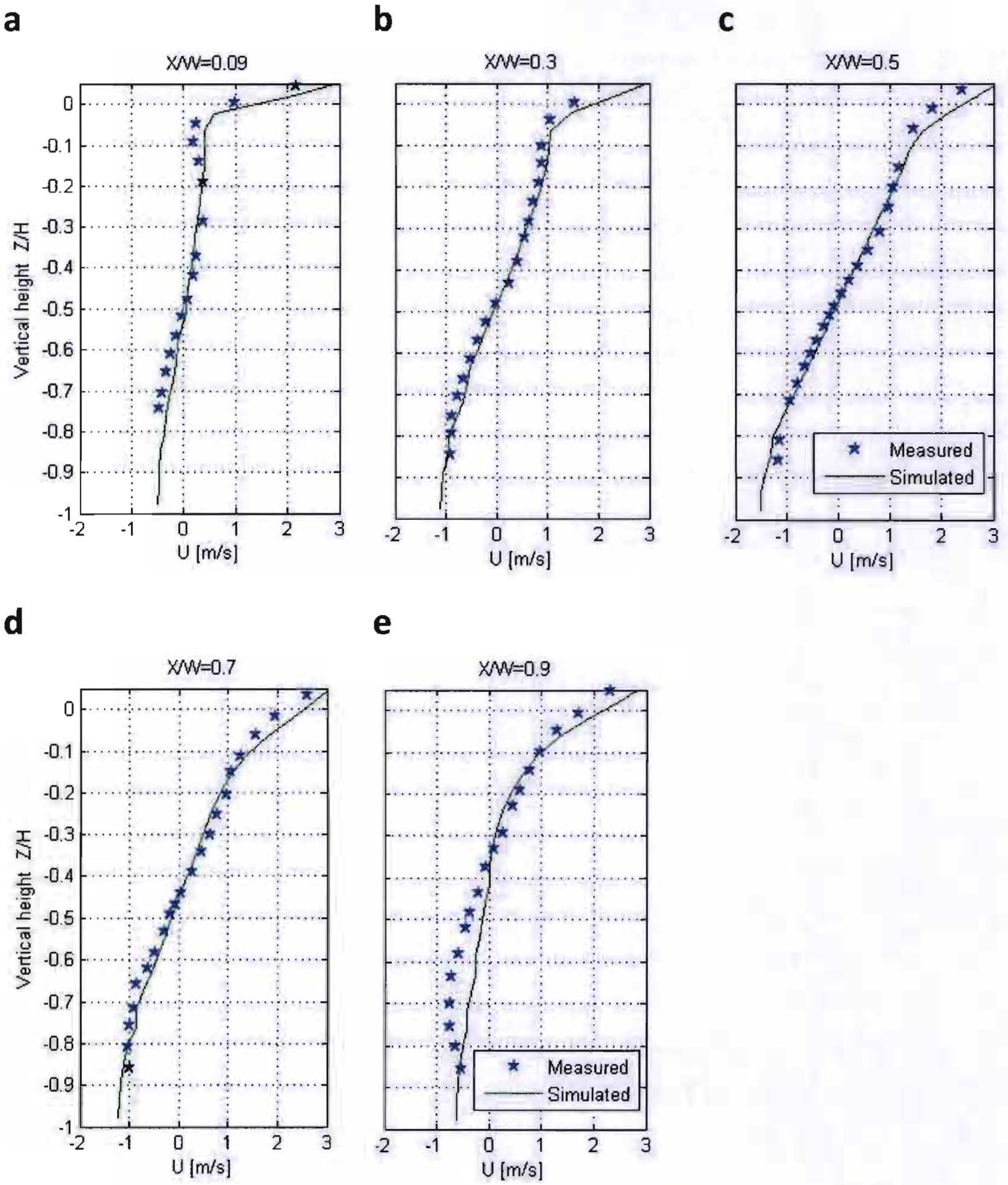

Figure 3-17: Comparison U component wind speed distribution in the W/H = 1.0 street canyon on five vertical lines a) X/W = 0.09; b) X/W = 0.3; c) X/W = 0.5; d) X/W = 0.7; e) X/W = 0.9.

Concluding remarks

In this validation case the dominant vortex location, wind flow pattern, and wind speed profile were analyzed for three isothermal street canyon configurations. For simulation purposes a structured grid with 18,957 cells, equidistant cells in the street canyon, and the RNG k-ε model were adopted. After validation of the prediction of wind flow for the isothermal CFD model, the next step is to implement buoyancy effect into the CFD model.

3.2 Case study for validation: 2-D buoyancy effect

3.2.1 Description of validation case

The sun, human activities, installations, and various other sources, heat up the thermal mass of buildings. Depending on the temperature difference between building surfaces and air, convective heat transfer influences the wind flow pattern and air temperature. Continuing on the previous validation case, another 2-D case is adopted to test the model's capability of predicting non-isothermal flows; a heated street canyon wall in the CFD model represents a building façade heated by the sun. The wind flow pattern and temperatures predicted by this CFD model are validated against wind tunnel experiments as described by Kovar-Panskus et al. (2002b). This paper provides wind tunnel measurements of a logarithmic boundary layer flow across an urban street canyon and aims to show the phenomenological changes in the flow field of heated buildings compared to non-heated buildings. In total, four different test cases were evaluated in which the reference wind speed U_{ref}, measured at a height of 1 m, varied between 0.5 m/s, 0.8 m/s, and 1.0 m/s. Inside the canyon different thermal conditions were simulated by heating the windward-facing wall to respectively 80 °C and 120 °C using heating mats. All the non-windward-facing walls in the cavity were cooled to ambient temperature (T_{ref}), how this was realized is not described in the paper. Also, a value for the ambient temperature during the experiment was not mentioned. However, based on color maps used in the figures, T_{ref} = 20 °C is assumed. Initially the windward-facing wall temperatures might seem high. However, due to the use of a scaled street canyon configuration, wind speed and wall surface temperature were adapted to obtain realistic Froude numbers with respect to a representative full-scale street canyon. In the paper, the Froude number was defined by:

$$Fr = U_{ref} \cdot \left(\frac{g \cdot H \cdot (T_{wall} - T_{ref})}{T_{ref}}\right)^{-1} \qquad \text{(Eq. 3.2)}$$

The canyon model width was equal to the height H = 0.285 m; both fit a scale of 1:70, thus giving the model an approximate actual building height of 20 m. The neutrally stratified approach conditions were; boundary layer height δ = 1 m, aerodynamic roughness length between y_0 = 1.0 mm and 1.6 mm depending on the location in the wind tunnel, and a friction velocity between u^* = 0.032 m/s and 0.070 m/s. Flow measurements were taken with a two-component Laser-Doppler-Anemometer which simultaneously measured wind speed and direction, with an accuracy of 3.5% for the mean values and 4% for the turbulence quantities. Furthermore, the experiment was set-up such that the flow over the street canyon can be considered 2-D. The authors concluded that two-dimensionality was established for the central 60% of the spanwise length of the cavity. In this region the wind speed in the direction of the flow was within ±5% of the mean and turbulence intensity within ±10% of the mean. The temperature measurements were taken with thermocouples and a Platinum-Resistance-Thermometer with an accuracy of respectively 1.2 °C and 0.5 °C. A schematic representation of the wind tunnel experiment is depicted in Figure 3-18.

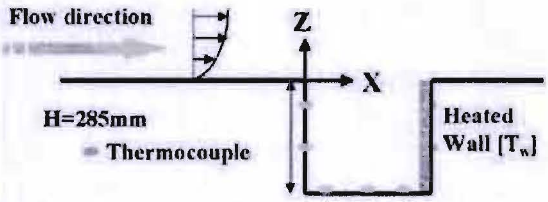

Figure 3-18: Schematic representation of wind tunnel and canyon model (Kovar-Panskus et al., 2002b).

CFD simulations are ideally performed under the same conditions as the wind tunnel experiment. Figure 3-19 shows the measured boundary layer mean wind speed and turbulent kinetic energy in the wind tunnel before separation at the street canyon compared to the simulated boundary layer conditions. The wind speed profile used as inlet boundary condition for the simulations are based on the measured y_0 and u^* values. The turbulence profile used as an input was derived from the measured turbulence profile before separation at the cavity.

The simulated mean wind speed profiles before separation at the cavity agree well with the measured values (Figure 3-19); predominantly the wind speed was slightly underestimated by the simulations. The differences for a wind speed of 1.0 m/s might seem slightly higher compared to the other two wind speeds, but the relative deviations are actually about the same. Figure 3-19 shows that also the simulated turbulent kinetic energy profiles agree well with the wind tunnel experiment. Higher deviations occur in the $0.1 < Z/H < 0.3$ region where the turbulence level was underestimated. Possible explanation is the variation in ground aerodynamic roughness length in the wind tunnel experiment between 1.0 mm and 1.6 mm, where only one roughness was adopted in the simulations. For both the wind speed and turbulent kinetic energy, no measurements were conducted in the near-ground region $Z/H < 0.1$.

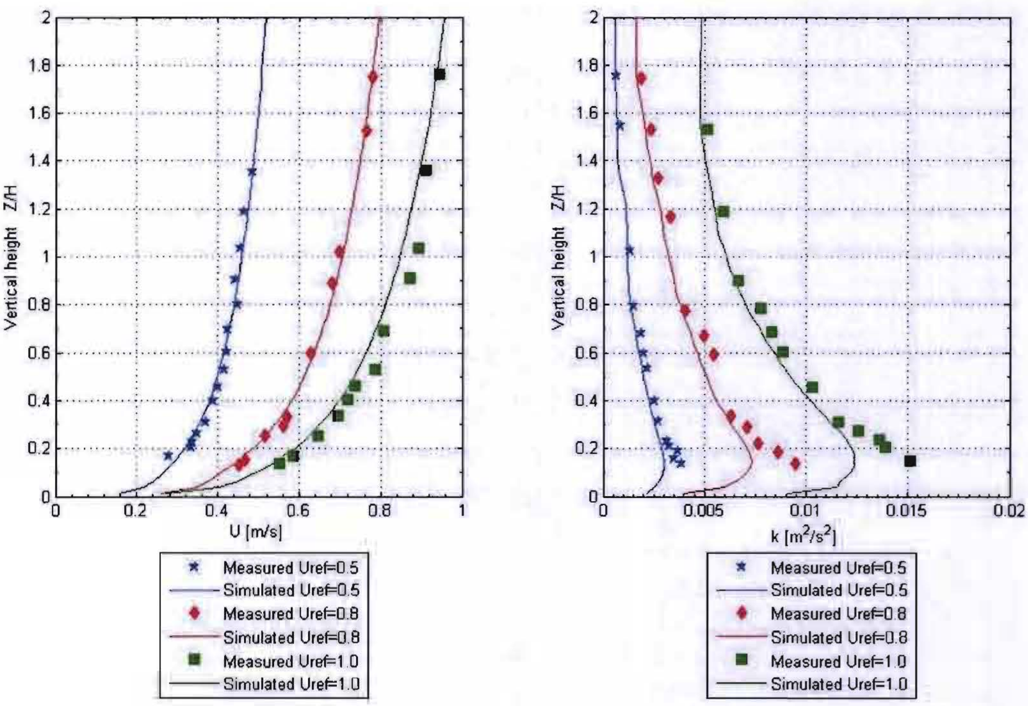

Figure 3-19: Comparison of measured and simulated boundary layer mean a) wind speed profile; b) turbulent kinetic energy.

3.2.2 Simulation characteristics

In this paragraph, the following simulation characteristics are assessed: grid independence of the solution, influence of the turbulence model, and near-wall modeling. The results of this review will form the basis for the CFD model that will be used to compare simulation result against experimental wind tunnel measurements.

Grid-sensitivity analysis

A grid-sensitivity analysis was conducted using the $U_{ref} = 1.0$ m/s, $T_{wall} = 80$ °C configuration. To create grids for this analysis, the same approach as described in the previous validation case was used. Consequently, the reference grid resolution is equal to 10 cells per building side, which corresponds to 37,000 cells in the computational domain. The grids used are similar to those used in the first validation case (Figure 3-3). The only differences between the geometry of the two cases are the canyon height and width and therewith the absolute domain size. The number of cells remains the same because of the 10 cells per building side assumption for the reference grid. Due to the similarities between the previous and this validation case a similar computational domain is adopted; in the streamwise direction the domain stretches 1H upstream and 15H for the wake, the height of the domain is 8H. Based on the assessment of turbulence models in the previous validation case, the RNG k-ε model was used for turbulence modeling. For calculating convective heat transfer near walls the standard heat transfer function was applied (Ansys 2009a). In addition, surface temperatures were imposed. The y^+ values for the different mesh resolution are described in Table 3-3. Other model characteristics are as presented in Table 3-4.

Table 3-3: y+ values for the six grid resolutions.

Number of cells	y^+ value	Number of cells	y^+ value
688	20 - 58	8,325	3 - 28
1,813	11 - 60	18,957	2 - 23
3,700	5 - 30	42,772	2 - 12

The measured mean wind flow pattern and wind speed distribution in the street canyon, with U_{ref} = 1.0 m/s, and ΔT = 60 °C between the heated wall and the reference ambient air temperature, is shown in Figure 3-20. Grid independence is assessed by comparing the wind flow and temperature distribution in the street canyon for different grid resolutions; results of grids with a number of cells varying between 688 and 42,772 cells are shown in Figure 3-21. Comparing the six grid resolutions, it can be seen that all grids except for the coarsest predict two vortices; a dominant vortex near the top of the canyon at location X/W = 0.5 and a secondary relatively large vortex at height Z/H = -0.6 near the heated wall. The latter is expected to be the result of an upward flow induced by the heated wall. This however, is not measured during the wind tunnel experiment (Figure 3-20). This noticeable difference will be elucidated in the next paragraph. Close to the heated wall, a high-temperature layer *T* = 65-80 °C is visible. The figures show that the higher the grid resolution, the smaller this layer is predicted to be. This suggests that this layer is indeed very thin when it would be measured.

When comparing the temperature distribution in the street canyon, the three coarsest grids are very much alike (Figure 3-21a-c), as are the three grids with the finest resolution (Figure 3-21d-f); the latter compare better to the measurements. The low-temperature area, T < 30 °C, occurring near the non-windward facing wall and top of the canyon overlay well. Even the observed bulge at a height of Z/H = -0.2 is predicted. When compared to the coarser grids, the three finer grids predict a stronger upward flow at a height of Z/H = -0.3, which results in a higher temperature in this region. Based on the figures it can be concluded that a grid-independent result for this validation case is not obtained. However, the grid with 18,957 cells is deemed sufficiently refined for further use in this validation case.

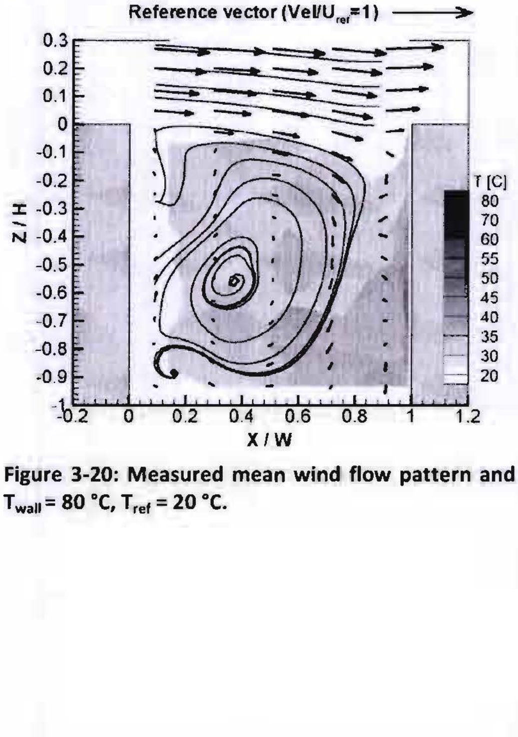

Figure 3-20: Measured mean wind flow pattern and temperature distribution in street canyon, U_{ref} = 1 m/s, T_{wall} = 80 °C, T_{ref} = 20 °C.

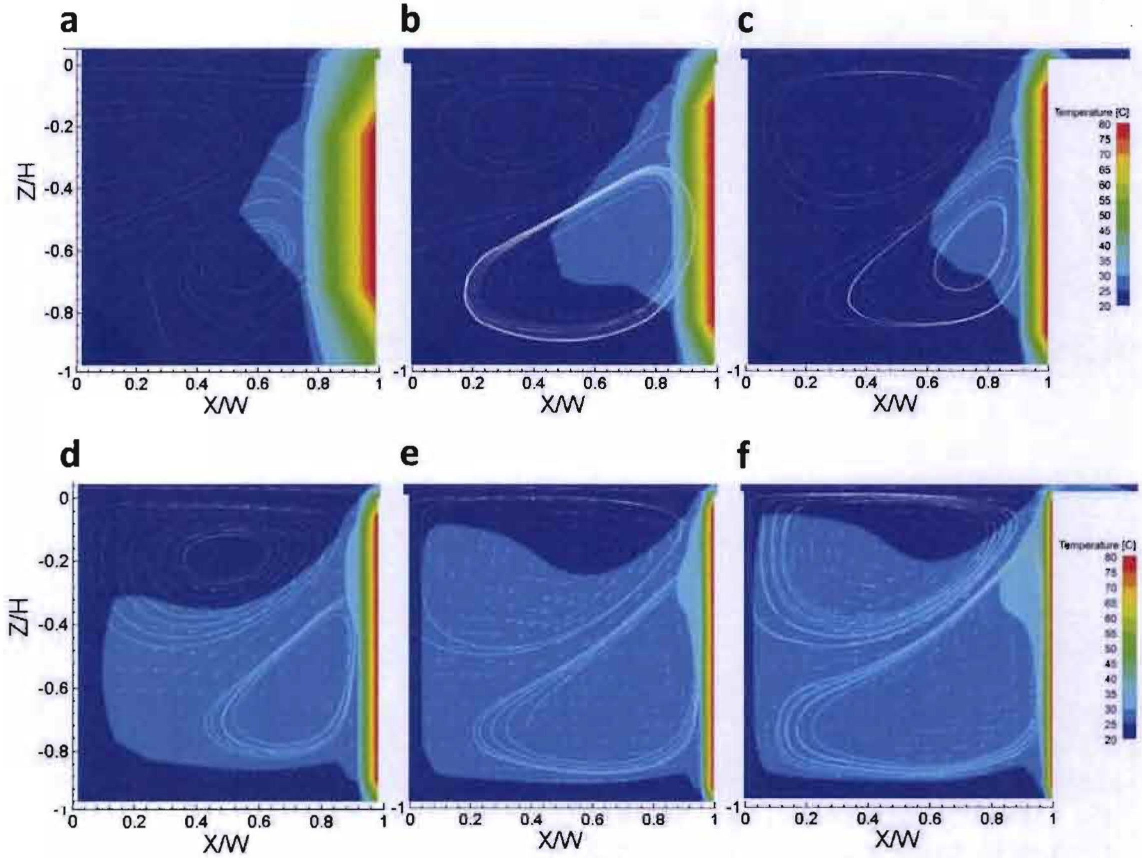

Figure 3-21: Mean wind flow pattern and temperature distribution in street canyon for U_{ref} = 1 m/s, T_{wall} = 80 °C, T_{ref} = 20 °C, a) 688 cells; b) 1,813 cells; c) 3,700 cells (reference grid); d) 8,325 cells; e) 18,957 cells; f) 42,772 cells.

Turbulence model

In addition to a grid-sensitivity analysis to obtain reliable CFD simulation results, different turbulence models are tested. For this purpose, again the U_{ref} = 1.0 m/s, T_{wall} = 80 °C configuration is used in combination with a grid of 18,957 cells. Based on the results of the previous validation case, only the standard k-ε model, the realizable k-ε model, and the RNG k-ε model are assessed. The RSM turbulence model is not included in the comparison. This is a result of the poor simulation results by the RSM model and resemblance between this and the previous validation case. Since these turbulence models have already been extensively tested on wind flow patterns and wind speed, this assessment focuses on the influence of the difference turbulence models on the temperature distribution in the street canyon.

The comparison of the three turbulence models as presented in Figure 3-22 shows that the simulation results are very similar. This is in line with the results obtained in the previous validation case. Most noticeable difference is the height at which the bulge at the top of the canyon commences and also its shape. Another interesting difference is the bulge on the side of the heated-wall which is, depending on the turbulence model, centered between Z/H = -0.2 and Z/H = 0.35. Compared to the measurements (Figure 3-20) the standard k-ε model and the RNG k-ε model produce slightly more accurate results than the realizable k-ε model. This observation is partially based on the height at which the low temperature bulge commences (indicated in Figure 3-22 by the arrows); measured was a height of Z/H = 0.2. Taking the previous validation into account, the RNG k-ε model will be used in this validation case.

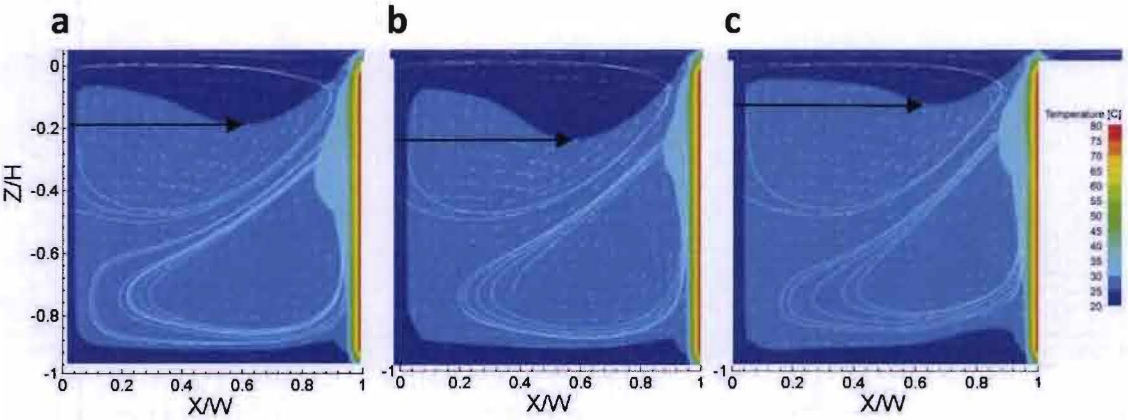

Figure 3-22: Mean wind flow pattern and temperature distribution in street canyon, U_{ref} = 1.0 m/s, T_{wall} = 80 °C, T_{ref} = 20 °C, with 18,957 cells, a) standard k-ε ; b) RNG k-ε; c) realizable k-ε.

Concluding remarks

Six mesh resolutions and three turbulence models were assessed to determine the appropriate simulation characteristics for the validation case: 2-D buoyancy effect. To obtain a grid-independent solution, wind flow pattern, and temperature distribution in the street canyon were assessed. In this assessment, applicability and accuracy of the applied wall functions depends on the y^+ values. In general, it could be stated that the y^+ values are very low and do not comply well with the suggested limits for standard wall function (Ansys, 2009a). This can be explained by the low friction velocity in this validation case. The lowest y^+ values for the six mesh resolutions vary from 2 for the finest mesh to 20 for the coarsest mesh. A decreased accuracy in all simulations can be expected as y+ values predominately lie within the buffer layer ($5 < y^+ < 30$). Noted should be that the CFD code Ansys (2009a) automatically switches from log-law to linear-law when $y^+ < 11.225$, to increase model applicability.

Based on the presented results in this paragraph, a grid with 18,957 cells will be adopted for this validation case. This grid resolution is two steps finer than the reference grid which is based on the recommended 10 cells per building side. Also, the performance of several turbulence models was assessed. Based on the results presented in this paragraph and taking the previous validation case into account, the RNG k-ε model is adopted for this validation case.

3.2.3 Comparison of simulation and measurements

The simulation results will be compared on two aspects with the measurement data from the wind tunnel experiments; the wind flow pattern and temperature distribution. Based on the grid-sensitivity analysis and turbulence model assessment, a grid with 18,957 cells and the RNG k-ε model is used to run the 2-D RANS simulations. Table 3-4 describes the applied grid and other CFD model characteristics. With respect to fluid density, the Boussinesq approach is adopted, as the CFD model is likely to converge faster, when compared to using a model set-up with a temperature based fluid density (Ansys, 2009b).

Table 3-4: Grid and model characteristics for validation case.

Feature	Description
Grid	Structured grid, 18,957 cells, equidistant cells in street canyon, minimal cell size $12.39 \cdot 10^{-3}$ [m], maximum cell ratio in other parts of domain 1.05
Domain	Height 8H, upstream domain 5H, downstream domain 15H; where H = 0.285 [m]
Solver	Steady 2-D RANS
Convergence criteria	Scaled residuals for, continuity: $1 \cdot 10^{-11}$, velocities: $1 \cdot 10^{-11}$, energy: $1 \cdot 10^{-11}$, k: $\cdot 10^{-11}$, ε: $1 \cdot 10^{-11}$
Turbulence model	RNG k-ε model; $k = \frac{1}{2} \cdot (u' + 2v'^2)$, $\varepsilon = \frac{u^{*3}}{(\kappa \cdot (y+y_o)}$, both profiles are based on measured values
Discretization	Pressure velocity coupling: scheme (SIMPLE) Spatial Discretization: Gradient (Least Squares Cell Based); Pressure (2nd Order); Momentum, Turbulent Kinetic Energy, Turbulent Dissipation Rate, and Energy (all four 2nd Order Upwind)
Near-wall modeling	Standard wall function, with full buoyancy effects (enables the inclusion of the influence of buoyancy effects on ε), Case 1.0 m/s, 80 °C: $1.6 < y^+ < 22.8$ Case 1.0 m/s, 120 °C: $1.6 < y^+ < 24.6$ Case 0.8 m/s, 120 °C: $1.5 < y^+ < 23.2$ Case 0.5 m/s, 120 °C: $1.4 < y^+ < 21.3$
Boundary conditions	
Inlet	Imposed temperature (20 °C), user-defined profiles adopted for k, ε and U, where $U = \frac{u^*}{\kappa} \cdot \ln\left(\frac{y+y_0}{y_0}\right)$.
Outlet	Imposed back flow temperature, pressure outlet; user-defined profiles adopted for k and ε
Canyon walls	Imposed wall temperature (20 °C for non-heated surfaces and 80 °C or 120 °C for heated surfaces), no-slip, roughness height $k_s = 0$ [m] (Eq. 3.1)
Bottom	Adiabatic, no-slip, roughness height $k_s = 6{,}19 \cdot 10^{-3}$ [m], $C_s = 2.05$ [-] (Eq. 3.1)
Top	Symmetry

Before making the comparison, some notes made by the authors of the validation paper are recited. Kovar-Panskus et al. (2002) note that differences can be expected when comparing 2-D predictions to the measurements as there was variability in the wall heating, i.e. non-uniformity, and also spanwise recirculation associated with the three-dimensionality of the configuration. In addition, the available measurements restrict comparability; the shortest distance to a wall where wind speed was measured was 0.09W, for temperature this distance was 0.014W.

In Figure 3-23 the measured and simulated wind flow and temperature distribution in the street canyon are shown. This figure shows that the simulations predict the dominant vortex to be higher than actually measured. In line with the measurements, the flow direction at the bottom left of the canyon is predicted to be streamwise for all four variants. However, in contrast with the simulations, measurements of the variants with U_{ref} = 1.0 m/s do not clearly show the streamwise flow continuing until the heated wall; the measured general flow direction near the heated wall appears to be downward. In the predictions, the streamwise wind flow at the bottom of the canyon together with the buoyancy-driven flow result in a secondary vortex near the heated wall. This vortex was predicted for all four variant; the measurements show a change in the direction of the wind flow for the variants with wind speeds U_{ref} = 0.5 m/s and 0.8 m/s, no evident vortex was measured. It is possible that due to measurement restrictions a minor secondary vortex has gone unnoticed during the measurements; a small vortex might have occurred very close to the wall. The predicted buoyancy-driven upward flow is noticeably larger than measured.

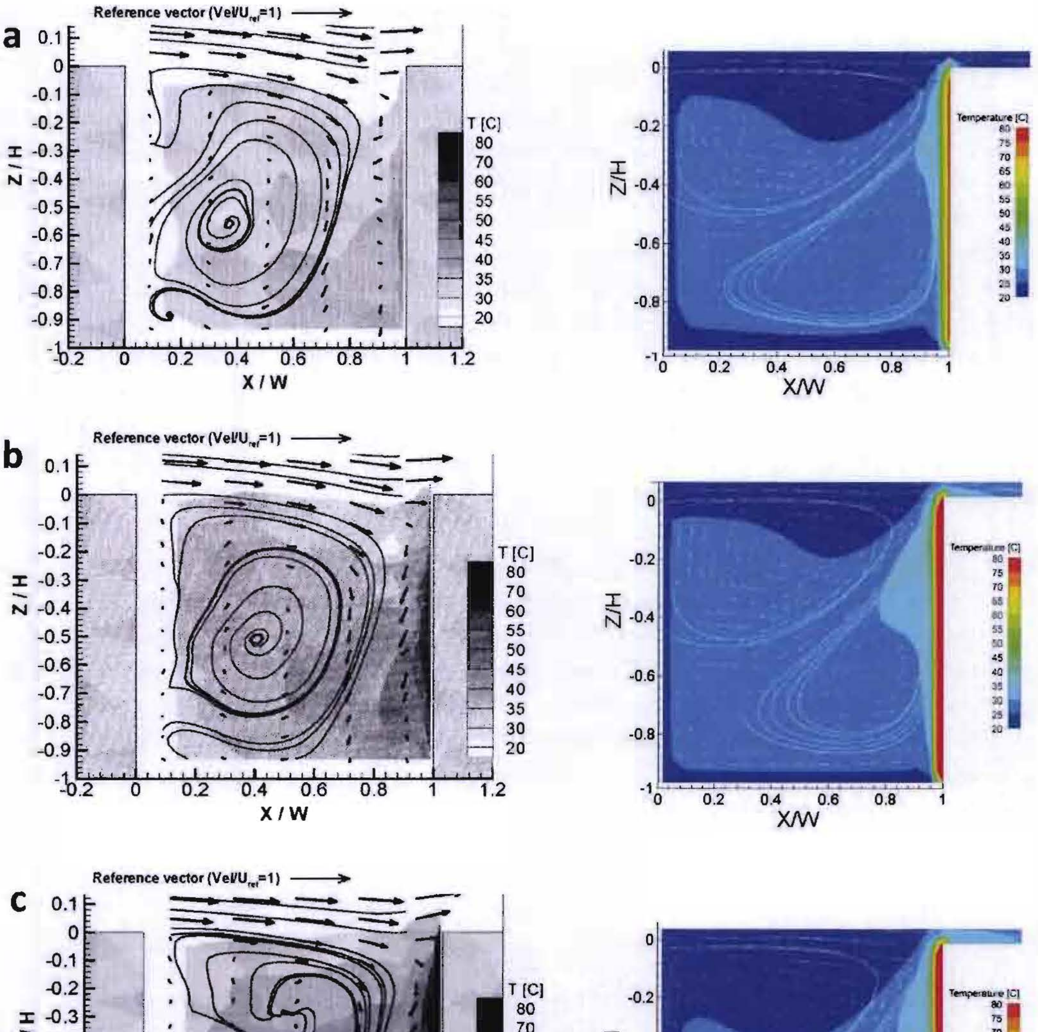

Figure 3-23: Measured (left) and simulated (right) mean wind flow pattern and temperature distribution in street canyon, T_{ref} = 20 °C, a) T_{wall} = 80 °C and U_{ref} = 1 m/s; b) T_{wall} = 120 °C and U_{ref} = 1 m/s; c) T_{wall} = 120 °C and U_{ref} = 0.8 m/s; d) T_{wall} = 120 °C and U_{ref} = 0.5 m/s.

Figure 3-24 and Figure 3-25 show details of the street canyons to better assess the heat transfer and temperature distribution near the heated wall. The contour of air temperature is similar for the four variants. This similarity also applies for the vertical height of the maximum air temperature near the wall which is constant at a vertical height of approximately Z/H = -0.2. For all variants the simulated temperature contour compares well with the measurements, especially the variants with low wind speeds U_{ref} = 0.5 m/s and 0.8 m/s. For the variants with U_{ref} = 1.0 m/s, the predicted contour is shifted upward by approximately 0.4H.

The high-temperature layer at the heated wall of respectively 50-80 °C (Figure 3-24a) and 80-120 °C (Figure 3-24b and Figure 3-25) were not measured. Nonetheless, it can be derived that the simulated high-temperature layer is thicker than during the experiment. Expected is that this higher temperature in the near wall region increases the buoyancy effect and herewith the updraft. This phenomenon would also explain the magnified streamwise flow at the bottom of the canyon and the development of the secondary vortex. The existence of this stronger secondary vortex in the simulations would also explain the upwards shifted vertical height of the highest temperature near the heated wall.

From Figure 3-23, Figure 3-24, and Figure 3-25 it can be concluded that, in general, the predicted thermal effect of the windward-facing heated wall on the flow pattern in the street canyon is overestimated. A similar conclusion was drawn by Richards et al. (2006) who reviewed 15 articles comprising numerical studies, wind tunnel experiments, field measurements, and combined studies. In general, strong influences were predicted as a result of direct ground or wall heating in the reviewed studies. A typical example of the discrepancy between measurements and simulation is the study of Louka et al. (2002), multiple vortices were predicted, where field data only reveals a single dominant vortex. No conclusions were drawn towards explaining the overestimation of thermal effects by Richards et al. (2006).

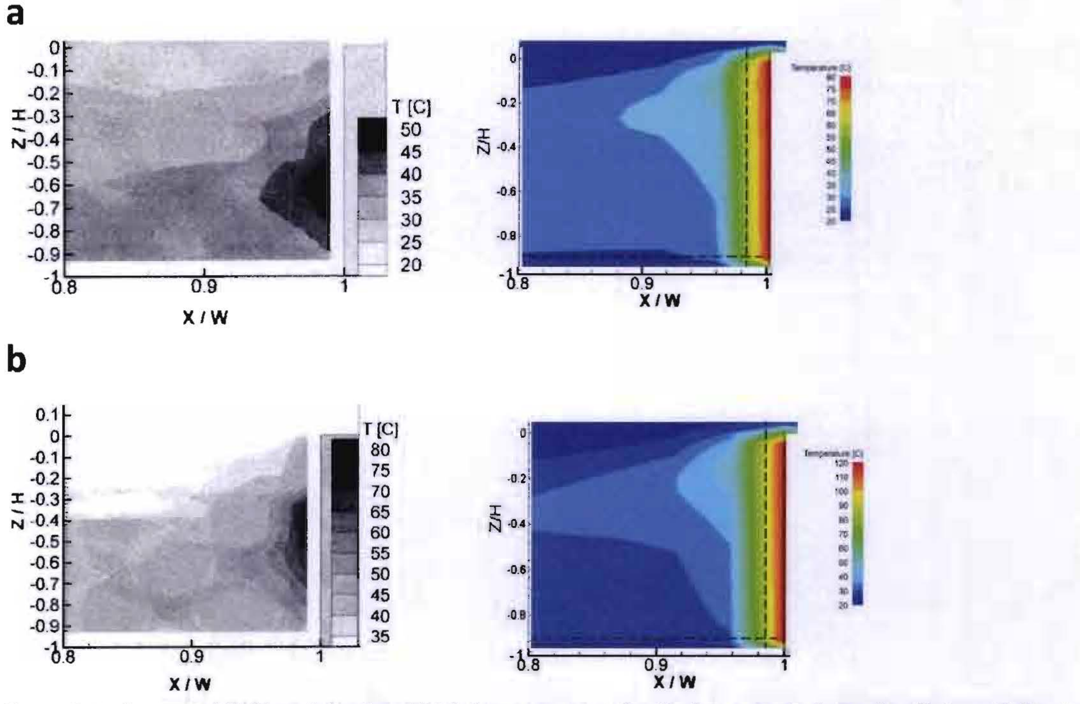

Figure 3-24: Measured (left) and simulated (right) temperature distribution near the heated wall, T_{ref} = 20 °C, a) T_{wall} = 80 °C and U_{ref} = 1 m/s; b) T_{wall} = 120 °C and U_{ref} = 1 m/s.

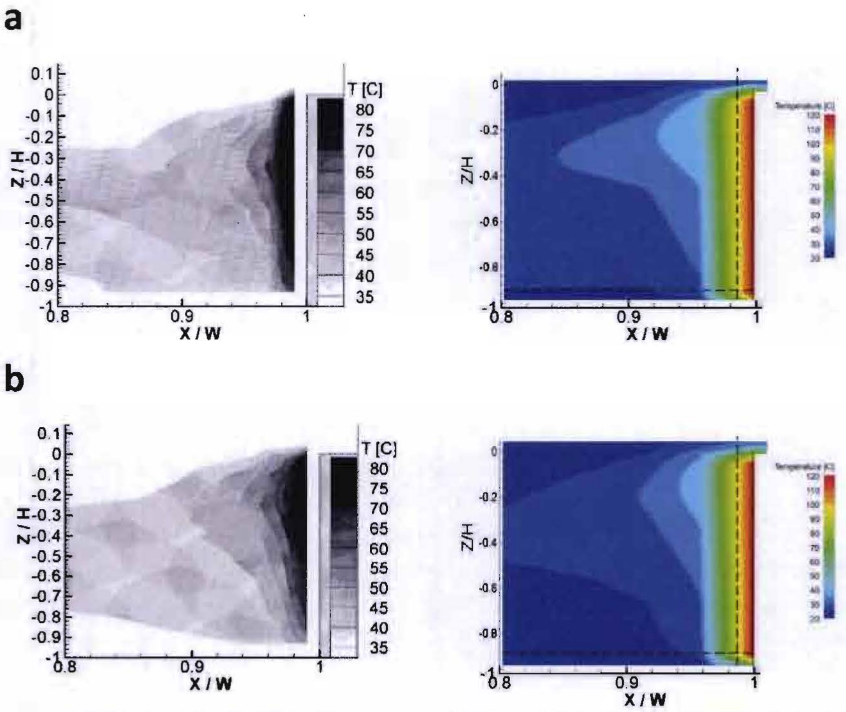

Figure 3-25 (Figure 3-24 continued): Measured (left) and simulated (right) temperature distribution near the heated wall, T_{ref} = 20 °C, a) T_{wall} = 120 °C and U_{ref} = 0.8 m/s; b) T_{wall} = 120 °C and U_{ref} = 0.5 m/s.

Concluding remarks

In this validation case the wind flow pattern and temperature distribution in the street canyon were analyzed for four cases in which the heated wall temperature and reference wind speed were varied. For simulation purposes a structured grid with 18,957 cells and the RNG k-ε turbulence model were adopted. After the prediction of 2-D wind flow and buoyancy effect, the next step is to continue with a 3-D validation case.

3.3 Case study for validation: 3-D wind speed and buoyancy effect

3.3.1 Description of validation case

The wind flow in urban areas is affected by both geometrical shapes and heated surfaces. For this study, the combined validation of these two factors is of importance. The wind flow pattern and temperatures predicted by the CFD model are validated against wind tunnel experiments as described by Richards et al. (2006) and Dimitrova et al. (2009). The former paper describes the original experiment and the latter a later publication presenting additional measurement values. Both papers provide wind tunnel measurement data of a power-law boundary layer flow across a single cube with leeward wall heating. Aim of the experiment was to simulate the thermal effects in the vicinity of a building with a heated wall. In total, three test cases were evaluated in which different thermal conditions were simulated by heating the leeward wall to respectively 30 °C (neutral case), 79 °C and 176 °C. These temperatures were realized by a ceramic radiant heater which heated a 2 mm aluminum plate fixed to this wall. The reference temperature was set to match the ambient temperature, T_{ref} = 24 °C. Similar to the previous validation case, high wall temperatures were applied because of the use of a scaled building configuration. Instead of using the Froude number, the authors applied the Richardson number [Eq. 2.7], which essentially is the inverse Froude number 1/Fr. The Richardson number is an indicator of whether mechanical or thermal effects are more dominant. At a number of ≈ 1 the motion is induced by both thermal and mechanical effects. A number of >> 1 indicates that the thermal effect is more significant.

The cube has a height, width, and length of 0.19 m. The model fits a scale of 1:100, thus giving the model an approximate actual building height of 19 m. The original paper on the wind tunnel experiment (Richardson et al., 2006) describes that the approach boundary layer conditions demonstrate the behavior and characteristics of a urban city like roughness to a scale of 1:100 with a power law exponent of α = 0.52 and a full-scale aerodynamic roughness length y_0 = 2.9 m. The resulting vertical wind speed profile is typically calculated by $U(z) = U_{ref} \cdot (z/z_{ref})^{\alpha}$. An overview of the wind tunnel set-up is shown in Figure 3-26 and Figure 3-27. Besides the location of the model, Figure 3-26 also shows the large number of sharp-edged roughness elements which were used to realize the high roughness length. Flow measurements were taken with a 2-D fiber-optic Laser-Doppler anemometer which had an accuracy of ± 0.05 m/s. The surface temperature and air temperature measurements (Figure 3-27b) were taken with thermocouples; an accuracy of ± 0.5 °C was achieved. In addition to these measurement inaccuracies, there was also a repeatability inaccuracy. This was documented to be 0.011 m/s for flow measurements and respectively 5 °C and 10 °C for T_{ref} and T_{wall}.

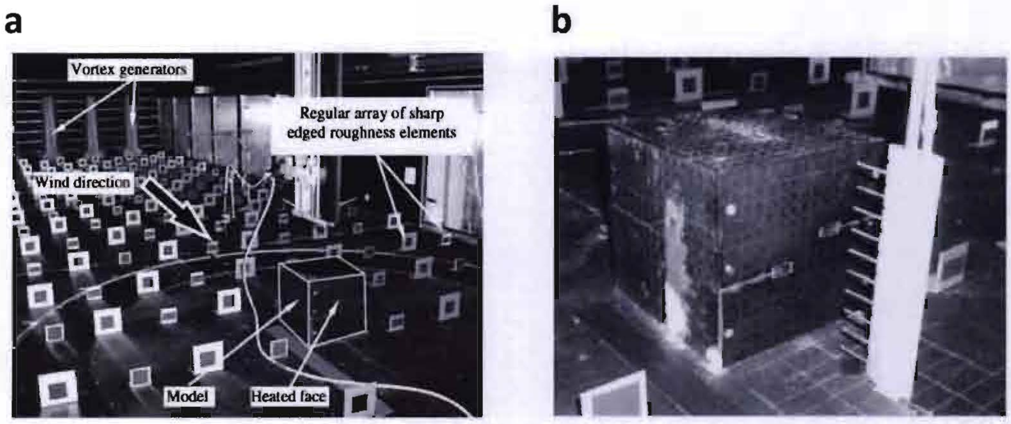

Figure 3-26: Pictures of wind tunnel set-up, a) building model and roughness elements; b) close-up building model (^{a} Richards et al., 2006) and (^{b} Dimitrova et al., 2009).

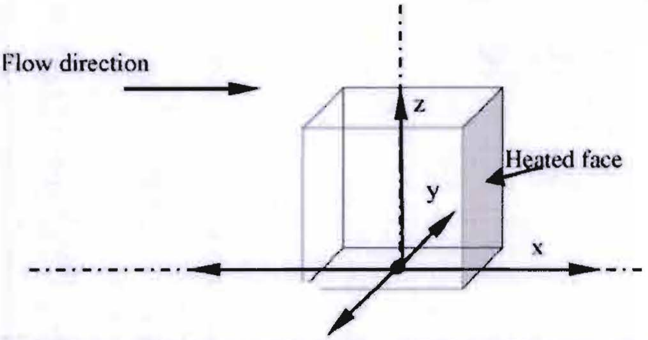

Figure 3-27: Coordinate system used for the wind tunnel experiment and the numerical model (Richards et al., 2006).

CFD simulations are ideally performed under the same conditions as the wind tunnel experiment. However, in contrast to the previous two validation cases, for this validation case no measurement data were available on how the wind speed and turbulence profiles develop themselves in the approach domain, only the conditions at 4H before the building model were presented. The assumption is made that the profiles are in balance with the ground roughness. In addition, no measurement data were presented by the authors on the behavior and characteristics of the wind flow near the ground $z < 0.62H$. Expected is that the wind flow in lower regions was strongly influenced by the roughness elements resulting in a lower wind speed combined with lateral flow directions which does not correspond well with the homogeneous vertical wind speed assumed in the near-ground region.

Some additional difficulties reproducing the wind speed profile were experienced as reference wind speed and height were not clearly reported in either of the adopted research papers. Based on a figure of the wind speed profile presented in the original research paper by Richards et al. (2006), reference values were derived to be $U_{ref} = 0.52$ m/s at a height of 0.2 m, for this study. The second paper (Dimitrova et al., 2009), in which additional measurement values were presented, did not provide a wind speed profile from which a reference value could be derived. The assumed reference values are based on four figures of the wind speed profile at four streamwise locations of the cube. At a height of 0.39 m, a wind speed of approximately 0.69 m/s was observed for all four locations. Based on the imposed power-law wind speed profile, the same reference wind speed as in the other paper can be derived, $U_{ref} = 0.52$ m/s at height $z_{ref} = 0.2$ m.

3.3.2 Simulation characteristics

In this paragraph, the following simulation characteristics are assessed: grid independence of the solution and influence of the turbulence model. The results of this review will form the basis for the CFD model that will be used to compare simulation result with experimental wind tunnel measurements.

Grid-sensitivity analysis

A grid-sensitivity analysis was conducted using two model configurations; 1) isothermal, 2) with a leeward wall heated to 176 °C. The former is used to obtaining a grid-independent solution with respect to predicting wind speed and flow pattern, the latter with respect to predicting temperature. The isothermal case was used for the grid-sensitivity analysis, because for the non-isothermal cases only flow fields were presented by the authors of the validation paper. Four grids were assessed with the number of cells in the computational domain varying between 17,405 and 814,428. The grid with 53,600 cells corresponds to the recommendation of 10 cells per building side (Franke et al., 2007; Tominaga et al., 2008). The y^+ values for the different mesh resolution are described in Table 3-6. The RNG k-ε model was used for turbulence modeling; other model characteristics are as presented in Table 3-6.

Table 3-5: y+ values for the four grid resolutions.

Number of cells	y^+ value (isothermal)	y^+ value (non-isothermal)
17,405	10 - 50	12 -54
53,600	5 - 43	7 - 43
237,600	3 - 32	3 -25
814,428	3 -21	2 - 18

In Figure 3-28, the RMSE (Eq. 3.1) of the predicted wind speed and temperature at four locations at the cube's center (y = 0) for the four grid resolutions are compared. Based on these figures it can be concluded that a grid-independent solution was not obtained. However, the grid with 237,600 cells is considered sufficiently refined and will be adopted for this validation case.

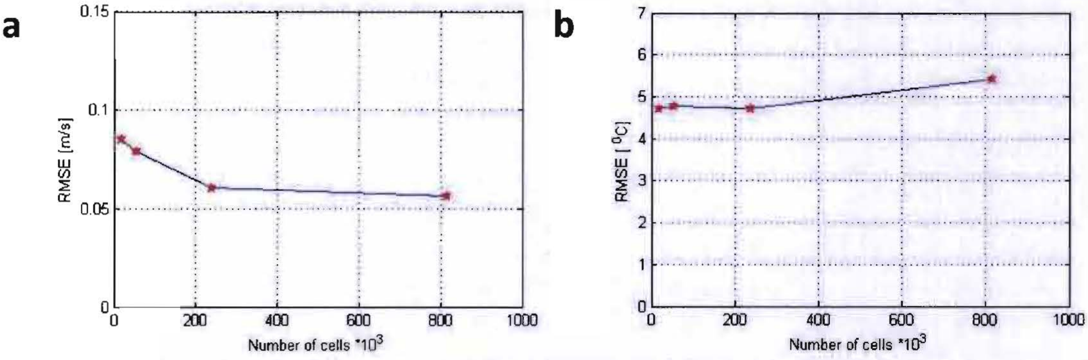

Figure 3-28: RMSE over respectively 35 and 42 points around the cube for four mesh resolutions, with U_{ref} = 0.52 m/s, for a) wind speed in an isothermal case; b) temperature in a non-isothermal case where T_{wall} = 176 °C, T_{ref} = 24 °C.

Turbulence model

After conducting the grid-sensitivity analysis, different turbulence models were tested to assess the influence of the turbulence model on the simulation results. For this purpose, an isothermal and non-isothermal model configuration is used in combination with a grid of 237,600 cells. The influence of the standard k-ε, the realizable k-ε, the RNG k-ε model, and the RSM are assessed.

The comparison presented in Figure 3-29 shows that the predictions by the different turbulence models are very similar. The calculated RMSE for the turbulence models was respectively 0.067 m/s ± 0.008 m/s and 5.03 °C ± 0.37 °C. Comparing the individual results shows that the wind speed is slightly better predicted by the RNG k-ε and the realizable k-ε models. Similar, for predicting air temperature, the standard k-ε and realizable k-ε model produce slightly better results. Based on these two observations the realizable k-ε will be used for turbulence modeling in this validation case.

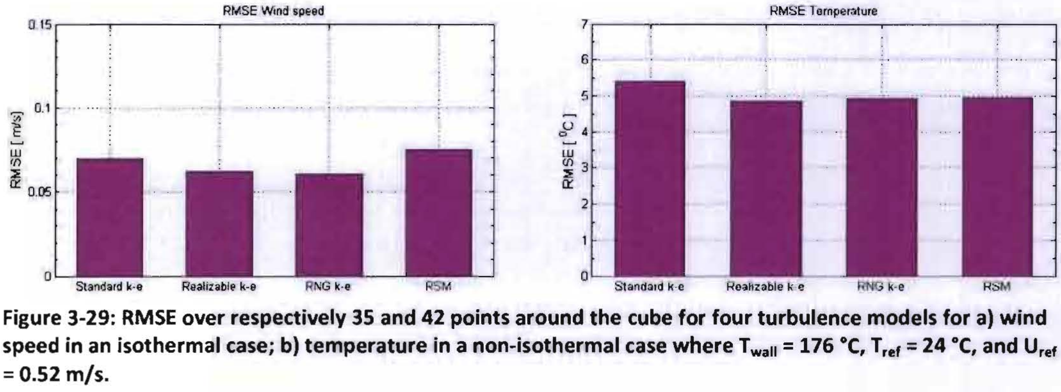

Figure 3-29: RMSE over respectively 35 and 42 points around the cube for four turbulence models for a) wind speed in an isothermal case; b) temperature in a non-isothermal case where T_{wall} = 176 °C, T_{ref} = 24 °C, and U_{ref} = 0.52 m/s.

Concluding remarks

Four mesh resolutions and three turbulence models were assessed to determine the appropriate simulation characteristics for the validation case: 3-D wind speed and buoyancy effect. To obtain a grid-independent solution, the RMSE of wind speed in the vicinity of the cube and the RMSE over 42 points behind the cube comparing temperature were assessed. In this assessment, applicability and accuracy of the applied wall functions depends on the y^+ values. Observed is that the y^+ values for the isothermal and non-isothermal simulations for the same grid resolution are very similar. In general it can be said that the y^+ values around the cube do not comply with the preferred lower limits as suggested by Ansys (2009a). From coarse to fine, the grids have a lowest y^+ value of respectively 10, 5, 3, and 2. A decreased accuracy in all simulations can be expected as y+ values predominately lie within the buffer layer ($5 < y^+ < 30$).

Based on the presented results in this paragraph, a grid with 237,600 cells will be adopted for this validation case. This grid resolution is one step finer than the reference grid which is based on the recommended 10 cells per building side. Also, the performance of several turbulence models was assessed. Based on the results presented in this paragraph, the realizable k-ε model is adopted.

3.3.3 Comparison of simulation and measurements

The simulation results will be compared based on three aspects with the measurement data from the wind tunnel experiments; wind flow pattern, wind speed and temperature distribution. Based on the grid-sensitivity analysis and turbulence model assessment, a grid with 237,600 cells (Figure 3-30) and the realizable k-ε model are used to run the 3-D RANS simulations. Similar to the previous validation case, the Boussinesq approach is adopted. Table 3-6 and Table 3-7 describe the applied grid and other CFD model characteristics.

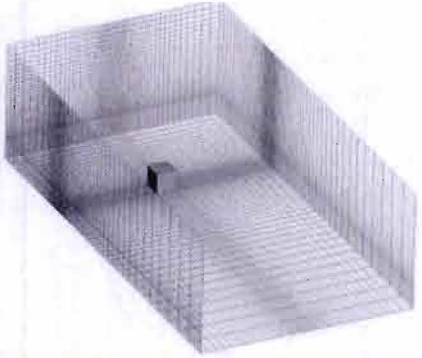

Figure 3-30: Computational domain, displayed are the wall, symmetry (of the domain sides), and inlet boundaries.

Table 3-6: Grid and model characteristics for validation case.

Feature	Description
Grid	Structured grid, 237,600 cells, minimal cell size $12.67 \cdot 10^{-3}$ [m], maximum cell ratio in other parts of domain 1.12
Domain	Height 6H, upstream domain 5H, lateral domain 5H, downstream domain 15H; where H = 0.19 [m]
Solver	Steady 3-D RANS
Convergence criteria	Scaled residuals for, continuity: $1 \cdot 10^{-11}$, velocities: $1 \cdot 10^{-11}$, energy: $1 \cdot 10^{-11}$ k: $\cdot 10^{-11}$, ε: $1 \cdot 10^{-11}$
Turbulence model	Realizable k-ε model; empirical k and ε profiles (Eq. 2.4 and Eq. 2.5)
Discretization	Pressure velocity coupling: scheme (SIMPLE) Spatial Discretization: Gradient (Least Squares Cell Based); Pressure (2nd Order); Momentum, Turbulent Kinetic Energy, Turbulent Dissipation Rate, and Energy (all four 2nd Order Upwind)

Table 3-7 (Table 3-6 continued): Grid and model characteristics for validation case.

Near-wall modeling	Standard wall function, with full buoyancy effects (enables the inclusion of the influence of buoyancy effects on ε), Case isothermal: $2.5 < y^+ < 32$ Case 79 °C: $2.5 < y^+ < 25$ Case 176 °C: $2.9 < y^+ < 28$
Boundary conditions	
Inlet	Imposed temperature (24 °C), user-defined profiles adopted for k, ε, and U, where $U(z) = U_{ref} \cdot \left(\frac{z}{z_{ref}}\right)^{\alpha}$
Outlet	Imposed back flow temperature (for non-isothermal cases only), pressure outlet; user-defined profiles adopted for k and ε
Cube's walls	Imposed wall temperature (79 °C or 176 °C for heated surfaces, other building surfaces according to the values presented by Richards et al. (2006)), no-slip, roughness height $k_s = 0$ [m] (Eq. 2.1)
Bottom cube's approach	Adiabatic, roughness height $k_s = 6{,}33 \cdot 10^{-3}$ [m], $C_s = 7.73$ [-] (Eq. 2.1)
Bottom cube's wake	Imposed wall temperature, roughness height $K_s = 6{,}33 \cdot 10^{3}$ [m], $C_s = 7.73$ [-] (Eq. 2.1)
Top	Symmetry

Isothermal case

In Figure 3-31 the measured and predicted mean wind speed fields are shown. The CFD model is unable to accurately predict the recirculation vortex behind the building, a too large vortex is observed. Predict is a low wind speed field which stretches diagonally from x/H = 1.1 at height z/H = 0.75 to the bottom of the domain at x/H = 2.1, effectively creating a very large vortex. This is a result of the k-ε model which underestimates the turbulent kinetic energy in the recirculation region behind the building and therefore overestimating the wind speed and size of the recirculation vortex. This is typical for k-ε model and more general for linear RANS models. This however, does not mean that good results cannot be obtained in more complex situations (Casey and Wintergerste, 2000; Hargreaves and Wright, 2007; Tominaga et al., 2008).

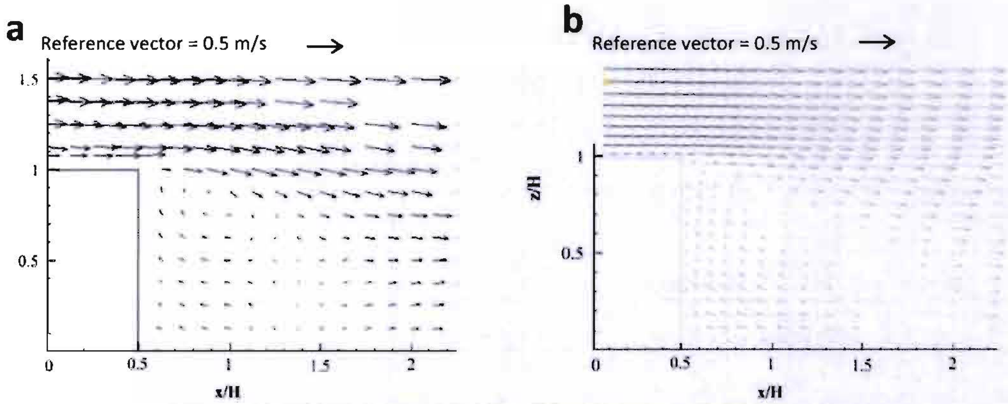

Figure 3-31: Comparison of a) measured; b) predicted flow field at location y = 0 for the isothermal case.

The observations made from Figure 3-31 also reflects upon the comparison of the wind speed profiles as shown in Figure 3-32 and Figure 3-33. The mentioned large recirculation vortex especially has an effect on the region behind the building for z/H < 1. Figure 3-32 shows that, in most parts, the predicted U component wind speed agrees well with the wind tunnel measurements. Largest discrepancies occur directly above the building model (x/H = 0) and in the wake of the cube. The same can be concluded from the calculated RMSE (Table 3-8 and Table 3-9). In Figure 3-33 the measured and predicted U component wind speed are shown on a horizontal plane. The largest discrepancy can be observed at the location x/H = 1.5.

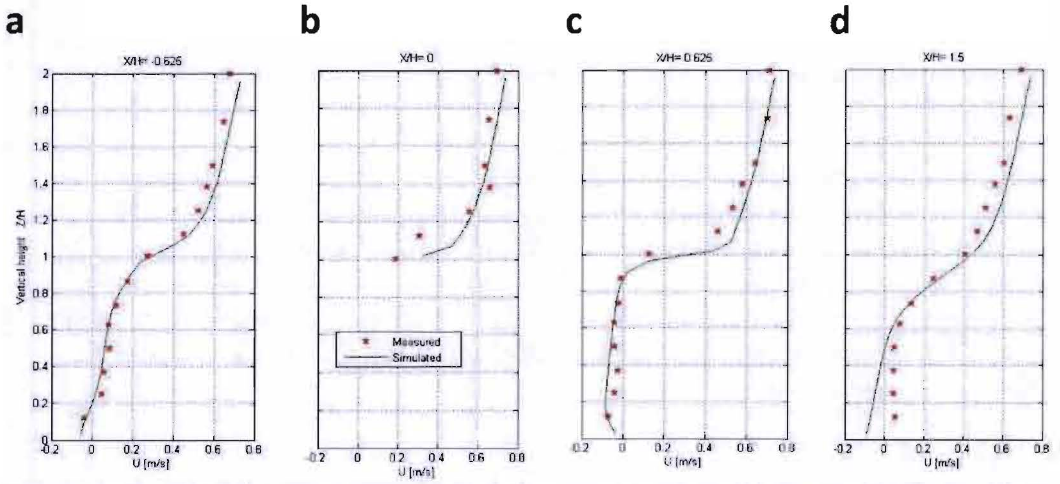

Figure 3-32: Comparison of U component wind speed in the vertical center plane (y = 0) at four location in the streamwise direction, U_{ref} = 0.52 m/s, isothermal case, a) x/H = -0.625; b) x/H = 0; c) x/H = 0.625; d) x/H = 1.5.

Table 3-8: RMSE of the calculated U component wind speed in the vertical center plane (y = 0), U_{ref} = 0.52 m/s, isothermal case.

x/H [-]	RMSE [m/s]
-0.625	0.033
0	0.096
0.625	0.092
1.5	0.067
Total	0.073

Table 3-9: RMSE of the calculated U component wind speed in the horizontal center plane (z/H = 0.5), U_{ref} = 0.52 m/s, isothermal case.

x/H [-]	RMSE [m/s]
-0.625	0.041
0	0.039
1.5	0.050
Total	0.044

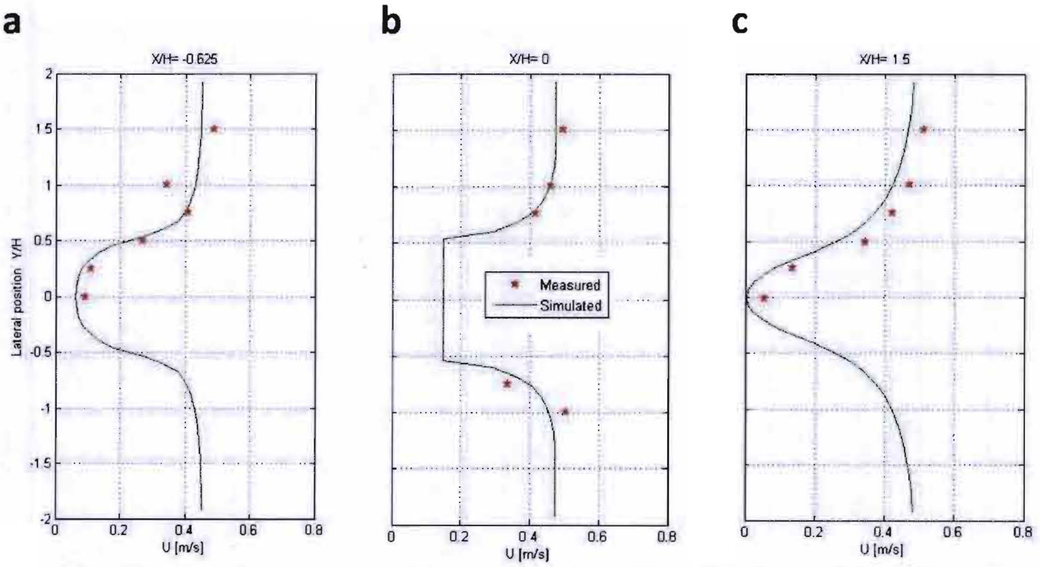

Figure 3-33: Comparison of U component wind speed in the horizontal center plane (Z/H = 0.5) at three location in the streamwise direction, U_{ref} = 0.52 m/s, isothermal case, a) x/H = -0.625; b) x/H = 0; c) x/H = 1.5.

Non-isothermal cases

In Figure 3-34 the measured and predicted mean wind speed fields for the non-isothermal case with an imposed wall temperature of 176 °C are shown. In line with the previous validation case, the thermal effect of the heated wall on the wind flow is slightly overestimated by the simulations. In Figure 3-34b this is observed at the top right corner of the building. For the measurements (Figure 3-34a) at location $x/H = 1.25$ (indicated by the red line) it can be observed that $U = 0$ m/s and $W \neq 0$ m/s. The same is observed for the predicted wind flow, but then at the streamwise location $x/H = 1.75$ (indicated by the red line). Also, the height where the U component wind speed $\neq 0$ m/s, is different, respectively $z/H = 0.8$ and $z/H = 0.6$ for the measurements and the predicted flow. This can be explained by a higher U component wind speed due to the large recirculation vortex behind the building. Since no wind speed measurements were available for this case, a quantitative comparison is unfortunately not possible.

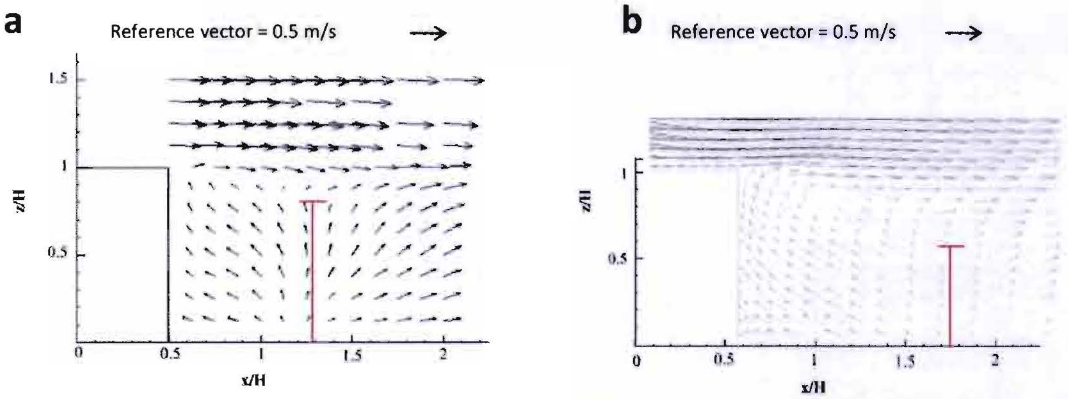

Figure 3-34: Comparison of a) measured; b) predicted flow field at the cube's center at location y = 0 with T_{wall} = 176 °C and T_{ref} = 24 °C.

The calculated RMSE of the predicted temperature distribution for the T_{wall} = 176 °C case is shown in Table 3-10. The total RMSE is 4.3 °C. What cannot be derived from this comparison is that the temperature was underestimated at all the evaluated points. This is visible in Figure 3-35 and Figure 3.36 in which the vertical and horizontal temperature distribution behind the building are presented. Expected is that one of the main causes for this underestimation is the overestimation of wind speed mainly at the top right of the building, as previously discussed in the isothermal case. This is confirmed when two points behind the cube at height 1.02H and streamwise locations $x/H = 0.55$ and $x/H = 0.625$ are scrutinized. For these points, a temperature of respectively 43 °C and 48 °C was measured and a temperature of 32 °C was predicted. Not including these points in the calculation decreases the RMSE from 4.3 °C to 3.4 °C.

Table 3-10: RMSE [°C] of the calculated vertical temperature distribution in the center plane at location y = 0 with T_{wall} = 176 °C and T_{ref} = 24 °C.

x/H [-]	RMSE [°C]
0.55	4.7
0.625	6.3
1.0	3.1
1.5	1.7
Total	4.3

The temperature distribution is similar for the two predicted cases (Figure 3-35b). When comparing the measured and predicted contours, it can be observed that they differ in shape and thickness of the temperature layers. For the measurements as well as the prediction, a higher temperature is observed near the top of the building (Figure 3-35). However, the size of this bulge is underestimated by the simulations. Practically, this can be expressed in thickness of the different temperature layers. For the T_{wall} = 79 °C case, the measured T/T_{ref} = 1.24 layer stretches to x/H = 1.2 and the predicted layer to x/H = 0.6. Similar for the 176 °C case, the measured T/T_{ref} = 1.36 layer stretches as far as x/H = 1.3, whereas the end of this layer is predicted to be much closer to the wall x/H < 0.6. The observed differences in profile shape and layer thickness correspond to the earlier observation of an average underestimation of 4.3 °C by the predictions.

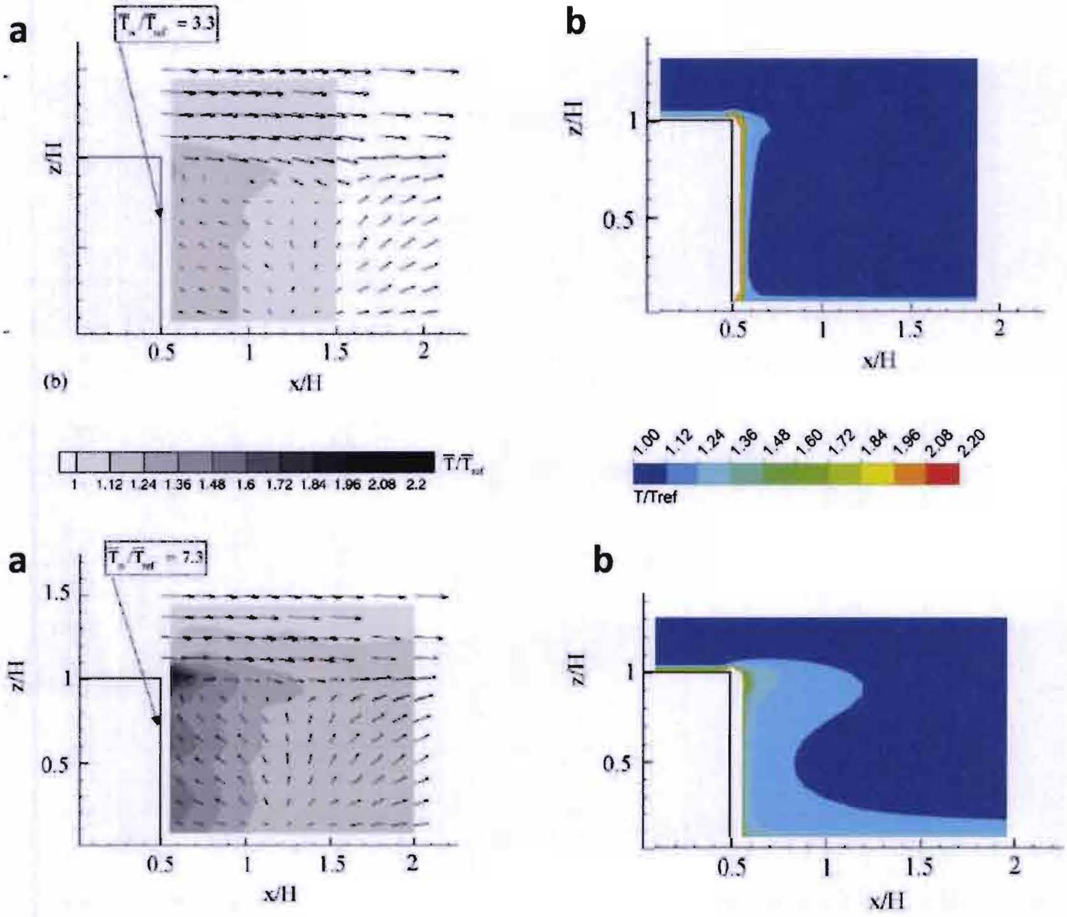

Figure 3-35: Comparison of a) measured; b) predicted vertical non-dimensional temperature distribution, T_{ref} = 24 °C, T_{wall} = 79 °C (top) and T_{wall} = 176 °C (bottom), y = 0. Temperature field are clipped to range meaning that values that are off the scale are blank, e.g. high T/T_{ref} > 2.2 non-dimensional temperatures near wall.

In Figure 3-36 the measured and predicted horizontal temperature profiles are shown at three heights. For the measurements and predictions, higher temperatures are observed near the sides of the building. The highest temperatures however, are predicted to occur near the corner of the building, whereas they were measured at the location y/H = 0.4 and y/H = -0.4. At a height of z/H = 0.7 (Figure 3-36a), the thickness of the T/T_{ref} = 1.12 at the corners is predicted to be thinner than was actually measured. Least accurately predicted is the temperature distribution at height z/H = 1.13. This is a consequence of the overestimation of wind speed above the cube (Figure 3-32b). From Figure 3-36 it can be concluded that the predicted horizontal temperature distribution profiles at two out of three heights correspond well with the measurements bearing in mind the minor inaccuracy at the corners and the constant underestimation of the temperature.

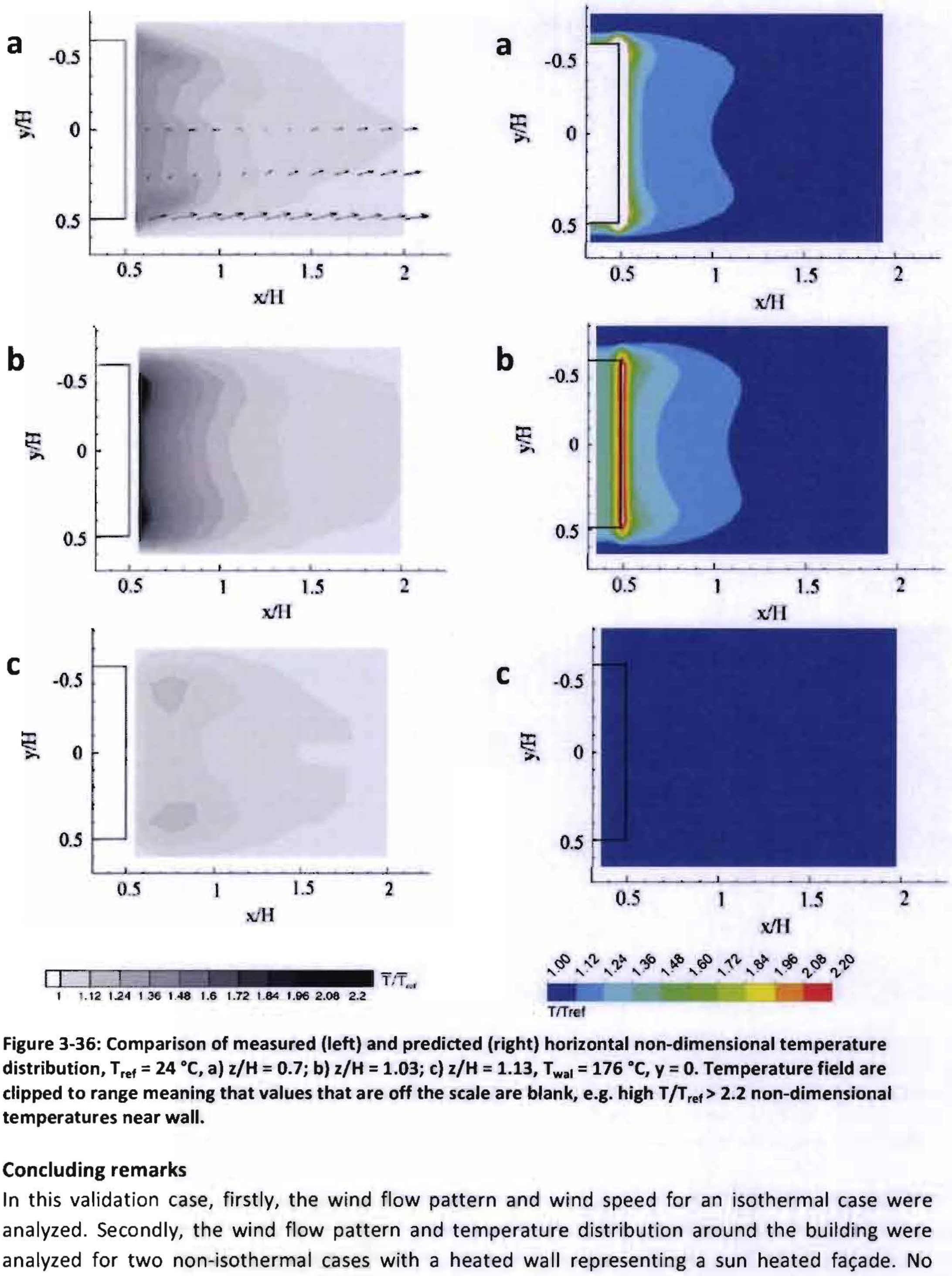

Figure 3-36: Comparison of measured (left) and predicted (right) horizontal non-dimensional temperature distribution, T_{ref} = 24 °C, a) z/H = 0.7; b) z/H = 1.03; c) z/H = 1.13, T_{wal} = 176 °C, y = 0. Temperature field are clipped to range meaning that values that are off the scale are blank, e.g. high $T/T_{ref} > 2.2$ non-dimensional temperatures near wall.

Concluding remarks

In this validation case, firstly, the wind flow pattern and wind speed for an isothermal case were analyzed. Secondly, the wind flow pattern and temperature distribution around the building were analyzed for two non-isothermal cases with a heated wall representing a sun heated façade. No quantitative comparison was possible concerning temperature distributions, as data were only available in picture form. For the comparison a structured grid with 237,600 cells and the realizable k-ε model were adopted. Before concluding the validation part of the study, the effect of applying standard wall functions instead of enhanced wall treatment is studied.

3.3.4 Adopting standard wall functions instead of low-Re-number modeling

For the case study city of Rotterdam, applying the preferred low-Re-number modeling method is not feasible due to the required grid resolution and corresponding computational resources needed. Instead, the wall-function approach was applied for both the case study city and all three validation cases. The variant as described below is conducted to get an indication of the effect of applying standard wall functions instead of low-Re-number modeling. For the comparison, the deviation in case set-ups must be taken into account. Due to the enhanced wall treatment limitation that no roughness can be assigned to walls, the approach wind speed and turbulence profiles are influenced. A no-slip condition without roughness was adopted simultaneously with the enhanced wall treatment. As a result, the first step in this case is to compare the approach wind speed profiles 1H before the cube. From this point on in this paragraph, the validation case as described in paragraph 3.3.1 will be referred to as "reference case".

The adopted grid and model characteristics for the variant are as described in Table 3-6. The isothermal reference case is used for comparing wind speed and the non-isothermal distribution reference case with T_{wall} = 176 °C for comparing the buoyancy effect and temperature distribution.

The comparison in Figure 3-37 shows a slight acceleration of the wind speed profile in the near ground region ($0.1 < z/H < 0.6$) when comparing the low-Re-number simulation to the reference case. A possible explanation is that no wall roughness can be set when enhanced wall-treatment is applied. This artificial acceleration might be countered by decreasing the approach domain length; however, the aim of this transition variant is to get an error estimate of applying low-Re-number modeling to an unchanged grid. The kink at height $z/H = 0.1$ can be explained by the influence on the wind speed profile by the building which is situated only 1H upstream. In Figure 3-37 only the $z/H < 2$ region is shown, because the region above ($z/H > 2$) overlays very well and shows no further interesting data.

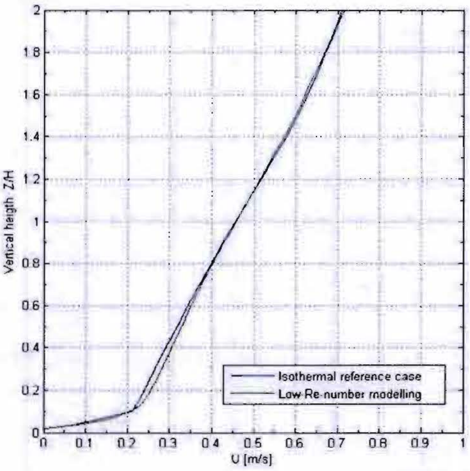

Figure 3-37: Comparison of wind speed profiles, reference case and low-Re-number modeling case, 1H before cube, y = 0

y^+ value

Sources in literature suggest that when $y^+ \approx 1$ is not feasible, at least $y^+ < 4$ should be realized so that the center of the wall-adjacent cell y_p is well inside the linear sub-layer (Casey and Wintergerste, 2000). The preferred value of $y^+ \approx 1$ was not feasible; the value was however mostly within the recommended limits for applying enhanced wall treatment and the low-Re-number modeling method. Near the building, y^+ values were in the range of $0.3 < y^+ < 4.3$ for the isothermal and $0.2 < y^+ < 4.5$ for the non-isothermal simulation. In the non-isothermal simulation the y^+ value was predominately well within the desired range, $y^+ > 4.5$ occurred only in a few small areas on the heated wall.

Wind speed profile

Table 3-11 and Table 3-12 show that adopting enhanced wall treatment, results in a total increased accuracy in predicting the wind speed of respectively 16.4% and 4.6%. In addition, it can be seen that for the profile in the vertical plane at x/H = 1.5, accuracy actually decreases. A similar observation is made for the horizontal profile in Table 3-12 where accuracy also decreases at the location x/H = 1.5. Based on the tables below, it can be concluded that the overall accuracy of the wind speed predictions has increased, taken in mind that locally some predictions are actually less accurate. This increased accuracy is mostly a result of the more accurately predicted wind speed around the cube. In the wake at location x/H = 1.5 wind speed was predicted less accurately.

Table 3-11: Comparison of the RMSE of the calculated U wind speed in the vertical center plane for the reference and low-Re-number modeling case, y = 0, U_{ref} = 0.52 m/s, isothermal case.

x/H [-]	RMSE [m/s] *Reference case*	RMSE [m/s] *Low-Re case*	Increased accuracy [%]
-0.625	0.033	0.024	27.3
0	0.096	0.087	9.4
0.625	0.092	0.054	41.3
1.5	0.067	0.075	-11.9
Total	0.073	0.061	16.4

Table 3-12: Comparison of the RMSE of the calculated U wind speed in the horizontal center plane for the reference and low-Re-number modeling case, z/H = 0.5, U_{ref} = 0.52 m/s, isothermal case.

x/H [-]	RMSE [m/s] *Reference case*	RMSE [m/s] *Low-Re case*	Increased accuracy [%]
-0.625	0.041	0.031	24.4
0	0.039	0.039	0.0
1.5	0.050	0.054	-8.0
Total	0.044	0.042	4.6

Temperatures

In contrast to the prediction of wind speed, the accuracy of predicting temperature profiles did not increase when enhanced wall treatment was applied. The prediction of temperature close behind the cube (x/H=0.55) is less accurate, where the other three locations show better results compared to the reference case. However, the decreased accuracy in the near wall region is larger than the increased accuracy in the region further away from the wall. As a result, the use of enhanced wall treatment for predicting temperatures in this validation case does not increase the total accuracy.

Table 3-13: Comparing the RMSE [°C] of the calculated vertical temperature distribution for the reference case and low-Re-number case, y = 0, T_{wall} = 176 °C, T_{ref} = 24 °C.

x/H [-]	RMSE [°C] *Reference case*	RMSE [°C] *Low-Re case*	Increased accuracy [%]
0.55	4.7	5.6	-19.2
0.625	6.3	6.0	4.8
1.0	3.1	2.4	22.6
1.5	1.7	1.2	29.4
Total	4.3	4.3	0.0

When enhanced wall treatment is applied, increased accuracy is expected, especially in the near-wall region. The opposite was observed from the previously shown tables. In Figure 3-38 the vertical temperature profile of the low-Re-number simulation is compared to the reference case and the measurements at a location close to the heated wall. This comparison shows that the shape of the profiles if very much alike. However, when enhanced wall treatment is applied, simulations show that the temperature in the z/H < 1 region is underestimated by 4-10 °C.

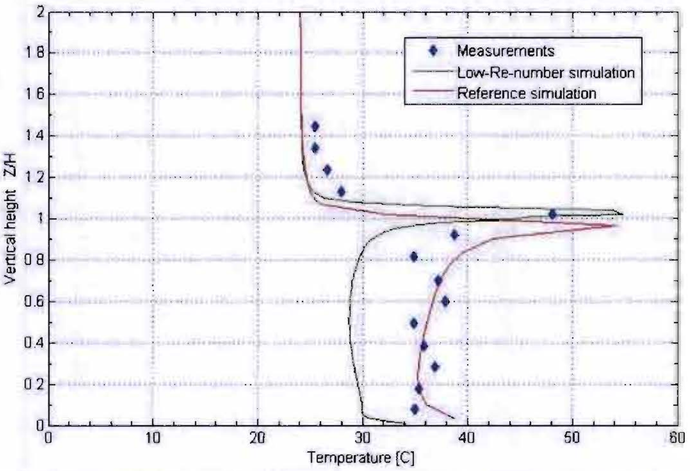

Figure 3-38: Comparison of the vertical temperature profile of the calculated vertical temperature distribution for the reference case and low-Re-number case, x/H = 0.55, y = 0, T_{wall} = 176 °C, T_{ref} = 24 °C.

There is no direct explanation as to why accuracy has decreased so significantly in the near wall region. Some possible contributing factors are described in the paper by Richards et al. (2006): for example a 2 mm aluminum plate was used, simulated material properties might have been slightly different and as a result the wall to air heat transfer coefficient could differ from that in the wind tunnel set-up. Related to the heat transfer coefficient is that the predicted wind speed is higher, increasing the heat flux and herewith the removal of heat from the near wall region. Also, another turbulence model might have resulted in better results. In previous paragraphs grid dependence of the performance of turbulence models has been demonstrated.

Concluding remarks

The variant described in this paragraph was conducted to get an error estimate of applying standard wall functions instead of low-Re-number modeling. Based on the comparison of the two approaches, it can be stated that, when applying low-Re-number modeling, accuracy increases for the predicted wind speed and that no increased accuracy was observed for the predicted temperature. This last observation is in contrast with literature, where an increased accuracy in prediction of temperatures is stated (Casey and Wintergerste, 2000). Possible causes for these contradicting results have been discussed in this paragraph.

Bases on the obtained results and literature sources, no conclusive and quantitative statements can be made concerning the possible decreased accuracy of the predictions, with respect to not adopting low-Re-number modeling, and instead adopting a relatively coarse grid and standard wall functions for the case study city.

4 Method: development of urban CFD models

4.1 Generating the computational grid and domain

Developing the mesh and computational domain was not straightforward. Besides solving the problem of missing entries in the GIS data, the computational grid also had to be divided into numerous manageable pieces and assembled in a later stage. The process of transforming the data set of xyz-coordinates with missing data points to a computational grid and - domain consists of the following steps:

1) Obtain GIS data. GIS data were purchased from *Stuurgroep AHN*, the company that manages the AHN (2011) data in the Netherlands. The structured data is supplied in text file format, where each line represents a xyz-coordinate.
2) Make a selection of the GIS data that will be used. In total six sections of GIS data (1.25 km^2 each) were used to configure the area of interest. Observed is that the missing GIS data points predominately occur over bodies of water. Based on this observation, a possible explanation for the non-functioning of LIDAR technology could be the reflective and absorbent qualities of water.
3) Missing coordinates in the GIS data set are filled up. Firstly, using 'if' and 'else' statements in an m-file of the mathematical application Matlab (The MathWorks Inc., 2010), gaps in the structured grid are traced by comparing the distance between two consecutive grid points in the text file with the GIS grid resolution. Consequently, coordinates on the ground plane (x and y direction) are added, at the same time, height data (z direction) based on the height of surrounding coordinates are appended.
4) Change the GIS data grid resolution from 0.5 m to respectively 2.0 m and 5.0 m. Making the grid coarser is realized by reducing the number of entries on the ground plane and appending height data that is an average of surrounding height data points. Changing the GIS grid resolution in an early stage has considerable advantages for creating the computational grid. Firstly, reducing the number of data points makes the preprocessing less time-consuming. Secondly, equal GIS grid resolution and mesh resolution allow for a simpler meshing scheme that is generally applicable.
5) Divide grid into manageable pieces. For this purpose an optimum computational grid size had to be found. Trial-and-error proved that 50 GIS data grid points on the ground plane, which translates into 6,085 separate meshes, to be the most time-effective. The necessity of dividing the computational grid into manageable pieces was a result of limited capabilities of the preprocessor.
6) Create journal files for the preprocessor. A journal-file contains command lines for the preprocessor Gambit which allows for automation of the preprocessing. There is no limit to the length of a journal-file; hence one after another part of the grid can be generated.
7) Create mesh files. The preprocessor Gambit is used to process the journal files. The last command line in each section of the journal-file is responsible for exporting a mesh file containing information on the created computational grid. Generating the computational grid turned out to be a very laborious process despite automating a large part of the grid-generation process. An estimated 25,000 hours of computational time was needed by the preprocessor. Paragraph 4.2 explains the process and method used to create the mesh files as this process is a very important part in developing an urban CFD model using GIS data.
8) Append the 6,085 mesh files into one computational grid. The created mesh files are imported and assembled in the CFD code Ansys (2009b) to form the computational grid that represents the case study city; Figure 4-2 depicts this process. Meshes can be coupled by adopting the boundary condition 'Interface' on connecting boundaries. For this purpose all interfaces should be given unique names if this has not yet been done when creating the mesh files. It is recommendable to do the same for all boundaries and fluids. Adopting unique names is recommended at all times when importing multiple meshes to make identification of each boundary easier. In addition, default boundary names given by Ansys are likely to cause trouble as a result of maximum name

lengths. For example, the first wall boundary is called 'wall' by default; each consecutive boundary has a '.1' added to this name.

Journal files were used to import meshes, assign unique boundary names, merging, and define mesh interfaces. In this project so called subs were created in which approximately 250 mesh files were appended in a case file. In a later stage these subs would be appended to one another. Note that after appending all meshes, boundaries, e.g. interfaces, walls, symmetry, velocity inlets, and pressure inlets, should be merged first. Defining the mesh interfaces is the last step, as merging deletes all previously defined mesh interfaces.

Figure 4-1 depicts the process of preparing GIS data and preprocessing. Steps *a-d* correspond with steps *1-4* as described above, step *e* summarized steps *5-7, and* step *8* corresponds to step *f*.

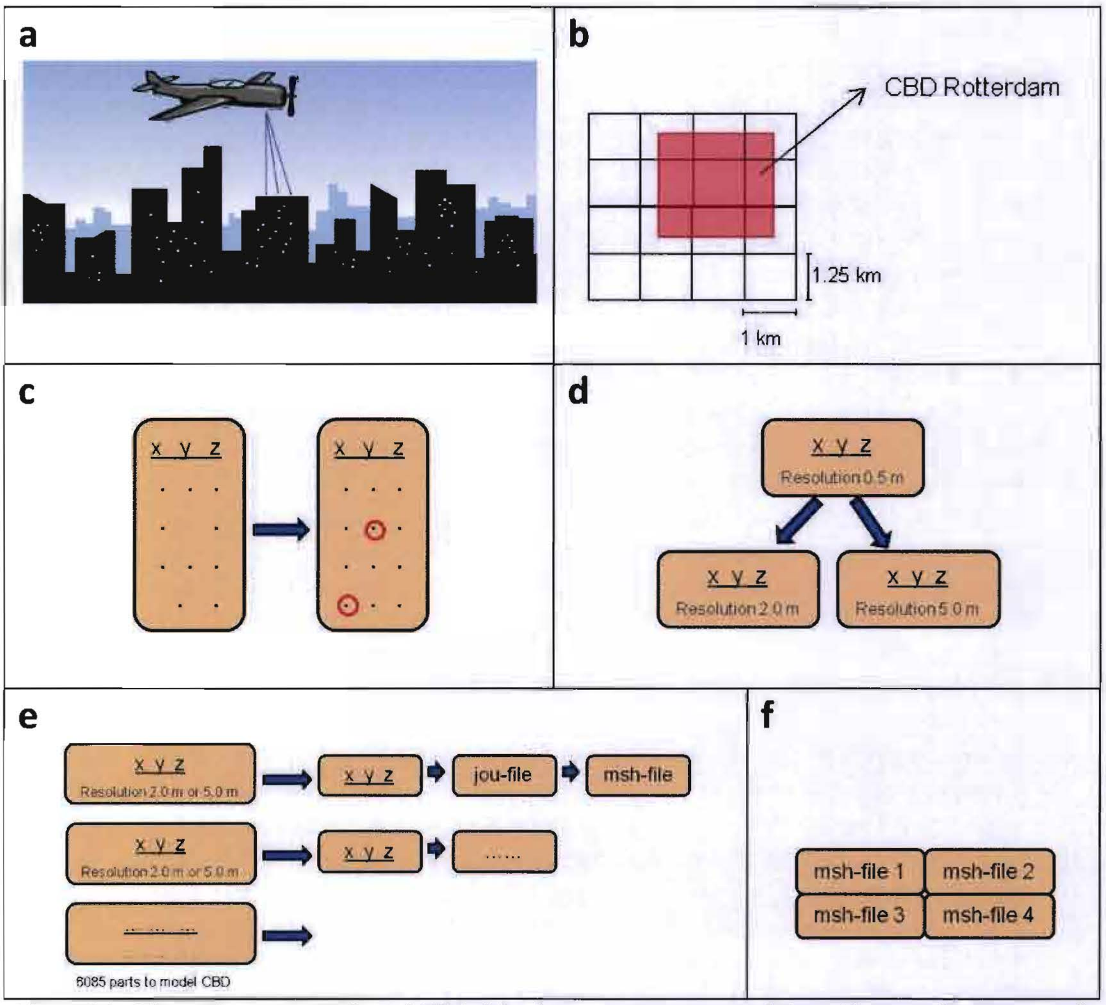

Figure 4-1: Schematic representation of GIS height data measurements and the grid-generation process. a) Elevation measurements are conducted by planes fitted with LIDAR technology and stored in a GIS database; b) make a selection of the GIS data that is going to be used; c) missing coordinates in the GIS data set are filled up; d) grid resolution of the structured grid is changed from 0.5 m to respectively 2.0 m and 5.0 m; e) grid is divided into manageable pieces for the preprocessor, journal files to create grid are written and the preprocessor prepares the 6,085 parts of the grid; f) couple mesh files into one computational grid.

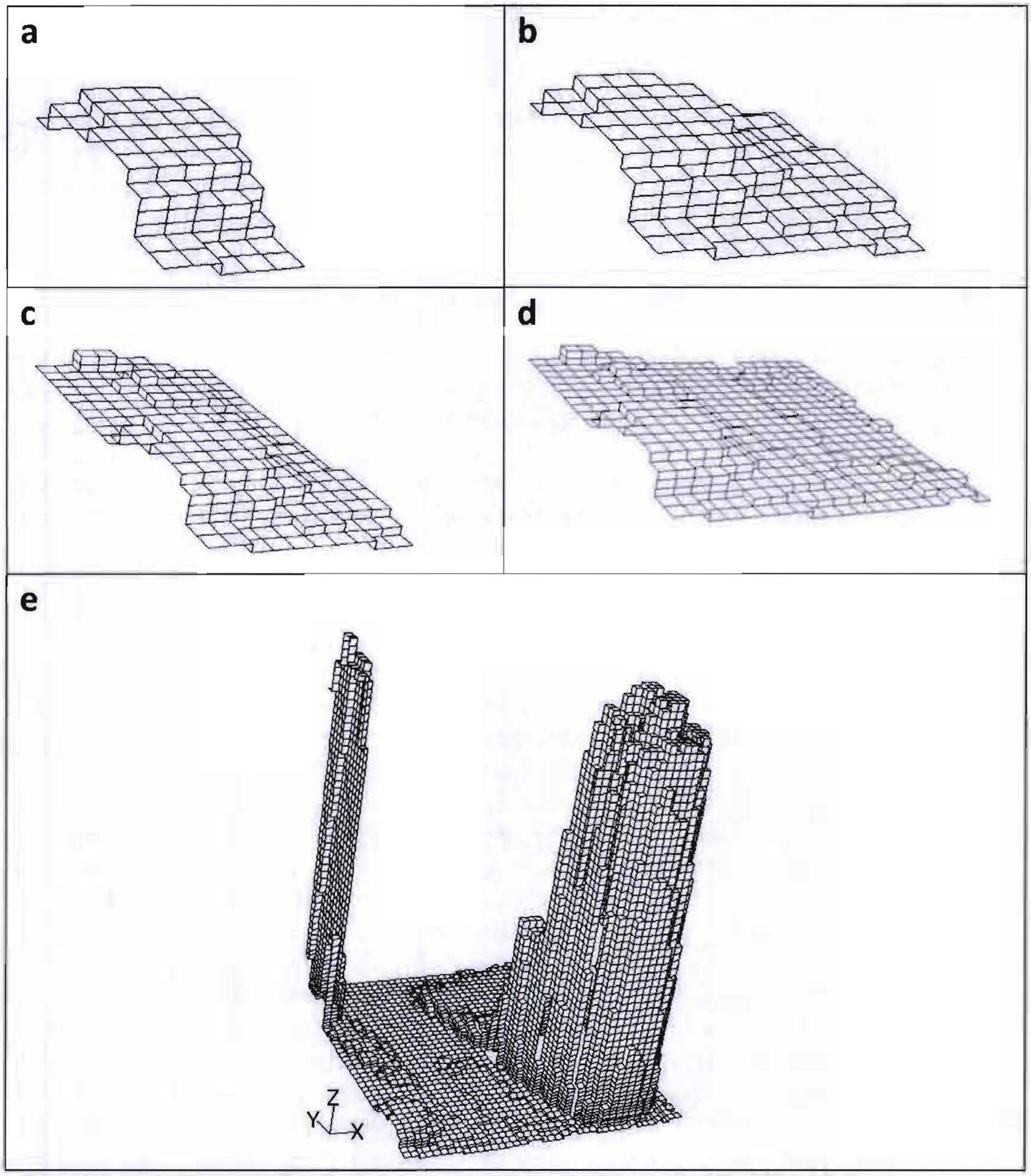

Figure 4-2: Appending mesh files; displayed are respectively a) 1; b); 2; c) 4; d) 8; e) 32 mesh files.

Matlab files

For the grid-generation process described in this paragraph, a total of five Matlab m-files (The MathWorks Inc., 2010) were created for respectively preparing GIS data, write journal files, and coupling the mesh files in Ansys (2009b):

1) Simplify coordinates and fill up gaps; the 'Rijksdriehoekscoördinaten' are transformed into more manageable coordinates, where at the same time gaps in the structured grid are filled up.
2) Change grid resolution; input for this m-file is the xyz-text files, the current grid resolution and the desired grid resolution.
3) Selection tool; this m-file is used to create separate text files containing xyz-coordinates for each of the 6,085 mesh parts.
4) Convert GIS data to journal files for the preprocessor.

5) Import and change boundary names; this last m-file generates journal files for the CFD code that controls the, import of mesh files, coupling of these mesh files, and assigning unique boundary and zone names.

With basic knowledge of Matlab and the other described programs, these m-files are self-explanatory due to added commentary lines. Hence, no additional information on the subject is provided in this report. The fourth m-file however, is elucidated in the next paragraph as this process is a very important part in developing the computational domain of the urban CFD model.

4.2 Generating mesh files for the urban CFD models

Generating the computational grid was semi-automated using journal files. The conventional grid-building approach BFG was applied whilst adopting a body-conformal structured grid. The GIS height data is used to create the building surfaces and other obstacles in the domain.

1) On the xy-plane at the top of the domain (6H for the case study city) a predefined number of vertices in the y-direction and one additional vertex in the x-direction are created. Edges are made using these vertices.
2) Face sweep in the y-direction is applied to create the first set of faces.
3) Using the already created faces, another sweep action is performed to create a structured set of faces, each face representing a particular GIS xyz-coordinate.
4) Face mesh is applied to all faces.
5) A series of connected meshed edges is created in the z-direction which will be used to make volumes by extruding faces from the top to the bottom of the domain. Separate meshed edges are used, because this allows for faces to be extruded to different heights.
6) For the top part of the domain, i.e. part of the domain above the highest building *H*, volume sweep including mesh is applied. The whole upper part of the domain is meshed as no buildings are present here. Volume sweep with mesh is also applied for the lower part of the domain, i.e. part of the domain from the top of the highest building down to street level. The face that is used for the sweeping process is selected using the LOC2ENT command which, depending on the used command, can select the closest vertex, edge, face, or volume. This allows for the correct faces to be swept, for example, if a xy-coordinate has an assigned z-value of 9.8 m, the journal-file is written such that sweeping stops at this height, effectively creating a surface representation, e.g. a building roof, pavement, or grass field. Furthermore, the GIS height data is rounded down to the closest available fixed height. This fixed height is a predefined value that goes up in steps of 0.8 m close to the ground, and 2.0 m near the top of the highest building. Obstacles in the computational domain can for example be, 6.5 m, 7.6 m, 9.8 m, or 10.1 m high, but nothing in between. This step is taken to ensure a conformal structured grid as well as to limit the number of computational cells.
7) Using the LOC2ENT command, boundary conditions are assigned to the top of the domain and interfaces. By default non-defined boundaries are transformed into wall boundaries when the grid is exported. It is recommended to also assign unique names to these boundaries and the fluid for further treatment in the CFD code.
8) The database-file is saved, a mesh file exported, and the next grid part can be automatically loaded into Gambit.

Figure 4-3 depicts the process of creating mesh files for the urban CFD model. Steps *a-g* correspond with steps *1-7* as described above

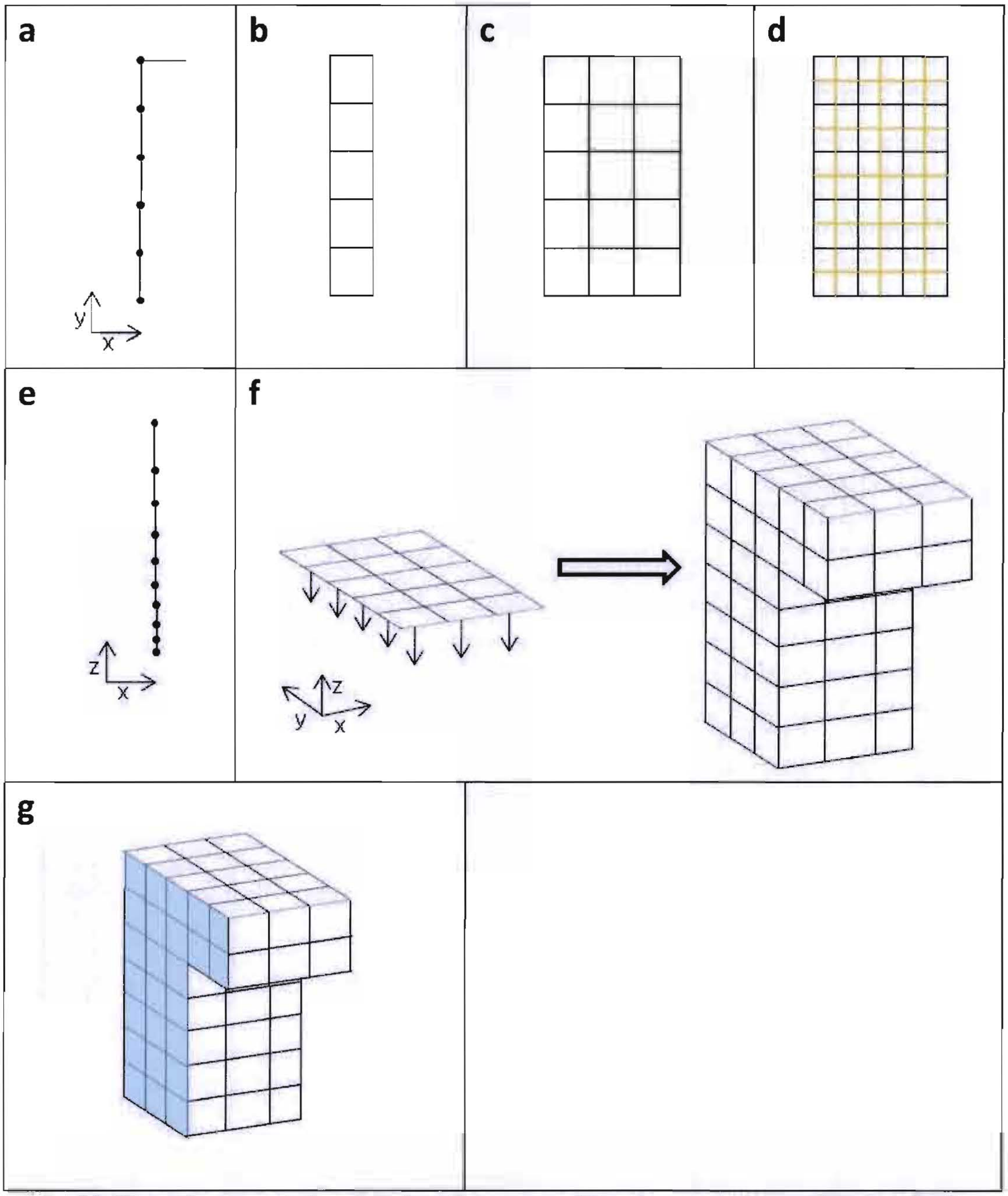

Figure 4-3: Schematic representation of mesh making process. a) Create vertices; b) sweep faces in y-direction; c) sweep faces in x-direction; d) face mesh; e) create reference mesh edge in z-direction; f) volume sweep to create the computational domain; g) define boundary conditions.

4.3 Discussion of the applied methodology

GIS data and nested-grid techniques

Experience from this study tells that utilizing GIS data can be a very effective asset in creating an urban CFD model. Several factors with respect to desired mesh resolution or resolutions when adopting nested-grid techniques must be taken into account when purchasing the GIS data:

- A high GIS grid resolution might not always be desirable, as it for example might take longer to preprocess data, e.g. decreasing GIS grid resolution and filling up missing data entries. When, for example GIS data is required with a resolution of 5 m for simulation purposes, there is no use in buying GIS data with a resolution of 0.5 m as this only results in the additional preprocessing step of decreasing GIS grid resolution.
- The obtained grid resolution influences and herewith limits the possible grid refinement as it is easiest to decrease resolution with a factor that is a natural number, e.g. 2, 3, and 4.
- The measurement accuracy should be as high as possible, e.g. the in this project adopted grid with a maximum deviation of 5 cm was more than sufficient.

Based on experiences from this study, a GIS data grid resolution of 1 or 2 meters is sufficient as a starting point towards creating a high-quality urban CFD model.

Another point of discussion concerning the use of GIS data for urban CFD models is at what domain size adopting GIS data to define the building geometries becomes interesting with respect to the time needed to create this grid, assuming a body-conformal structured grid is used to represent an urban area. Traditionally, city plans and applications, such as Google Earth (2011) are used to create the geometry of part of a city (Dixon et al., 2003; Gidhagen et al. 2004; Huang et al., 2005; Chan and Leach, 2007; Lu et al., 2007). It is difficult to define a so called breakeven point stating from which domain size it is interesting to use GIS data and semi-automating grid-generation techniques. Not only the domain size, but many other variables play a role, such as available computational resources, the user's knowledge, and already developed tools for preparing GIS data and preprocessing. The topology of the urban area should also not be underestimated, as several large buildings in a relatively small domain will noticeably simplify the manual grid-generation process when manually creating the computational domain.

As GIS data can limit the hands-on-time needed to preprocess the computational grid, nested-grid techniques can decrease the required computational resources needed for running the simulations. Due to the applied methodology this project does not provide information on the efficiency and effects of applying nested-grid techniques within the area of interest. A form of the nested-grid technique was however applied as the domain extensions in the approach, wake, and lateral direction had a different resolution on the ground plane, i.e. the xy-plane, than the three target areas Station, Coolsingel, and Residential Area. Two important aspects should be taken into account when decreasing resolution in the domain surrounding a target area. Firstly, resolution on the ground plane can be coarser, but too big a step should be avoided. Secondly, resolution in the z-direction should be kept the same throughout the domain for the purpose of calculating an accurate vertical wind speed profile. When considering the use of nested-grid techniques the advantages are obvious, however, the increased time needed for preparing GIS data and preprocessing should also be taken into account.

Creating the computational grid

At the beginning of the project a choice was made to use GIS data and semi-automate the grid-generation process, whilst adopting the traditional Body Fitted Grid (BFG) method to generate a structured grid. Essential for preparing GIS data and the semi-automatic grid-generation process is the use of a mathematical application, such as Matlab (The MathWorks Inc., 2010). Indispensable functionalities are the ability to write text and journal files, loop functions, and the use of conditional statements such as 'if', 'else', and 'then'. Below, the use of GIS data, the BFG method, and applied method to create the grid are discussed.

The consideration of using GIS data not only depends on the time efficiency, however it is the most important argument especially when developing urban CFD models. Besides time, this approach has other advantages over manually creating the computational domain, it is for example more likely that all obstacles in the urban environment are included and height differences, such as sloping streets are accounted for. Manually creating the computational domain on the other hand allows for incorporating greater building detail and a better representation of obstacles, such as vegetation and lampposts.

The choice was made to apply the traditional BFG method as opposed to the Immersed Boundary (IB) method; pros and cons of both methods have already been discussed in paragraph 2.3.8 of the literature study. Biggest advantages of the BFG method and likely reasons to choose this approach are that there is a lot of knowledge available, it is integrated in all commercial CFD codes, and a wide range of strong preprocessors is available. Biggest advantage of the IB method is its ability to deal with complex geometries. In this project though, this is not a significant factor looking at the desired grid resolution and requirements. However, it would have allowed for slightly more variation in obstacle height as the BFG method was restricted by fixed building heights to ensure a body-conformal structured grid. To assess this possible improvement, inaccuracies as a result of cut-through cells due to the non-body-conformal grid should be thoroughly investigated.

Generating the mesh started with preparing the GIS data and writing the journal files to generate mesh files, which in a later stage would be assembled into one computational grid. Two main issues can be identified as to why the intended computational grid of 4.2 km^2 could not be realized: 1) too many (mesh) volumes were created by the preprocessor and 2) too many separate meshes with non-conformal boundaries had to be appended in the CFD code. Figure 4-4 shows the causes of these two issues. The approach to use face sweep combined with separate mesh-edges in the z-direction to create the surface representations resulted in an abundance of meshed volumes. Creating these meshed volumes drains memory and decreases the preprocessor memory efficiency. To solve this problem the grid was divided into over 6,000 pieces. In turn, all these grid parts were assembled in the CFD code, a process which again was draining the computer's memory. It was not until this moment that the used software actually started producing errors and limitations towards creating the initially intended 4.2 km^2 computational grid (paragraph 4.4). In the end, the grid-generation process had to be stopped when an Ansys error message indicated that too many boundary names were defined. A yet unknown maximum was exceeded due to additional boundaries that were created by Ansys by default, as a result of non-overlapping boundaries (paragraph 4.4). In contrast to other boundaries, these new boundaries cannot be merged. Besides this problem, appending the meshes in the CFD code resulted in a very large computational requirement, causing Ansys to freeze when it was attempted to append two sets of approximately 1000 mesh files.

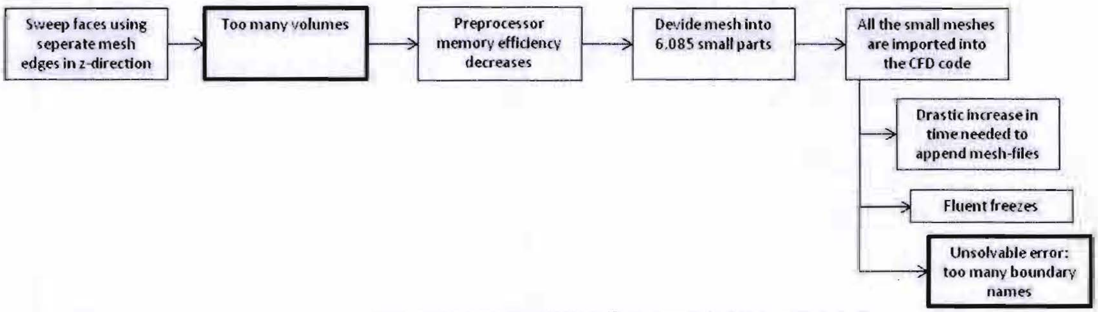

Figure 4-4: Cause and effect flow chart why the intended 4.2 km^2 grid could not be realized.

Now of course the big question is: "How can the number of mesh files that need to be assembled using the CFD code be reduced?" An option would be to develop a grid-generation method in which less meshed volumes need to be created by the preprocessor; as a result the grid would have to be divided into fewer parts. Expected is that this will also decrease the required computational resources. The second option is to use the same approach towards making the mesh, but then use a specialized preprocessor to append meshes before importing the meshes into the CFD code. The use of the software Tgrid and the Ansys functionality tmerge was suggested in a very late stage of this study. Tgrid is a specialized preprocessor used to create unstructured tetrahedral meshes for very complex and large surface meshes (Ansys, 2011). It is not clear, how this preprocessor deals with non-overlapping boundaries. Testing Tgrid capabilities might be interesting for future projects as at this moment no licenses for this product were available at TU/e. The use of tmerge was suggested by the Ansys helpdesk (Ansys help-desk, 2011). However, as tmerge basically works the same as the append function in Ansys, only without an interface, similar problems with respect to boundary names are expected.

Geometry of buildings and obstacles

One of the advantages of using GIS data is that it is more likely that all obstacles in the urban environment are included and height differences, such as sloping streets are accounted for. This advantage can also be seen as a disadvantage. As LIDAR technology is used for height measurements, e.g. parked vehicles, lampposts, and temporarily placed scaffolds and cranes are identified as surface representation. Also, bridges are identified as solid objects on the water surface. In Figure 4-5 a large street with partially a central reservation and pavement is displayed. It can be seen that despite the precaution of only conducting height measurements when the trees are leafless, still trees appear as solid objects in the computational domain (trees are encircled in the two figures).

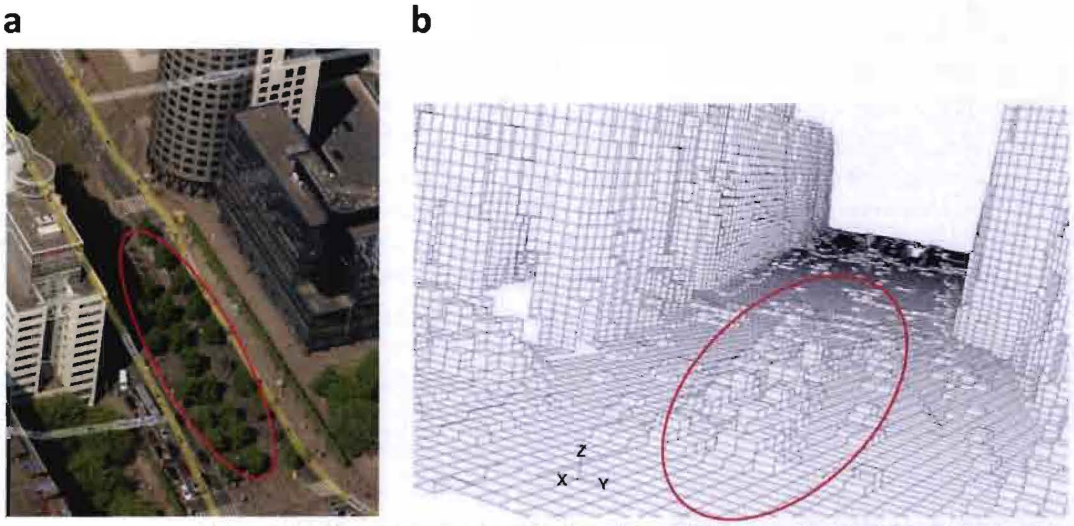

Figure 4-5: Street in the computational domain showing obstacles such as vegetation and cars. a) Screenshot Bing maps (2011); b) computational domain.

By coincidence, a building crane was included in the computational domain. A Google Earth (2011) screenshot of this crane and its geometrical representation are shown in Figure 4-6. The inclusion of this crane in the computational domain demonstrates the sensitivity of the applied GIS data approach with respect to temporary obstacles in an urban environment.

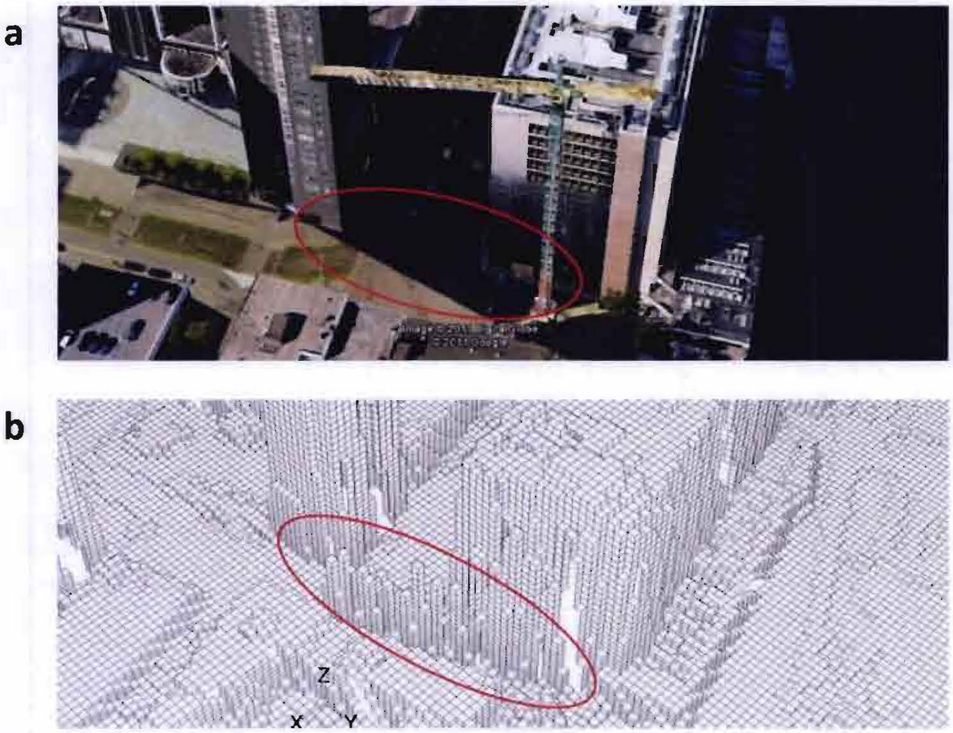

Figure 4-6: a) Google Earth screenshot and b) geometrical representation of building crane

When the GIS data grid resolution was decreased, new z-coordinates were calculated for each xy-coordinate based on the height data of the surrounding points. This averaging process, together with sloping roofs and building orientation results in a deformation of buildings in the computational domain. How sloping roofs influence building shape speaks for itself, how decreasing grid resolution and building orientation influences a building's shape in the computational domain is less obvious. In Appendix D the theory behind the often observed height differences near building façades is elucidated. In Figure 4-7 and Figure 4-8 a Google Earth screenshot and the corresponding geometry in the computational grid are compared. It can be observed that the actually cube-shaped building is affected by the change in grid resolution. In the same figure holes in the building's surface representation are visible; this is a result of non-overlapping boundaries. Due to graphical limitations of Ansys, these interface boundaries cannot be displayed and holes are observed in the geometry. Both height difference near building façades and holes in the geometry can also be observed in Figure 4-5 and Figure 4-6.

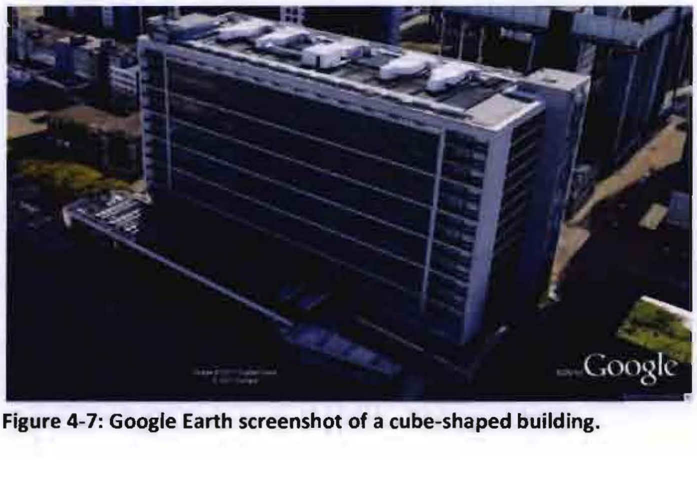

Figure 4-7: Google Earth screenshot of a cube-shaped building.

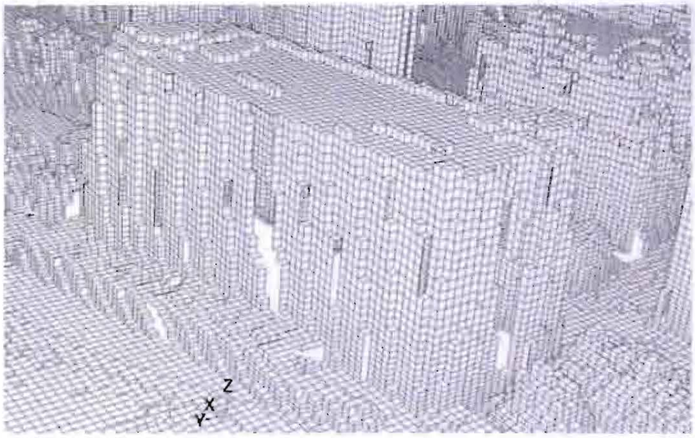

Figure 4-8 (Figure 4-7 continued): Geometrical representation of a cube-shaped building.

Applications of the urban CFD model

After discussing the use of GIS data, the applied methodology, and the graphical representation of buildings and obstacles; the question now is how the employed compromises influence capabilities and application of the created CFD model.

Based on the conducted model validation and applied grid and model characteristics, the obtained simulation results (chapter 5) with respect to the analysis of natural ventilation in urban areas are deemed satisfactory. Recommended is however, that these types of urban CFD models are not used for wind comfort problems, as they lack important details with respect to the building shapes and have a grid resolution that is too coarse near the ground.

In addition to analyzing wind flow and heat transfer in cities, urban CFD models can also be used for, e.g. analysis of pollutant dispersion, smoke dispersion, and the in the introduction discussed UHI effect. In paragraph 2.1, possible measures towards mitigating the UHI effect were summarized. The most widely applied mitigation measure is increasing evapotranspiration, i.e. latent cooling by planting and vegetation. This can be translated into the creation of more parks, green zones, and applying green roofs. Two limitations in the current CFD model prevent the incorporation of this most widely applied and promising mitigation measure. Firstly, moisture transfer should be added to the model's functionality. The second issue is a result of how the grid is build-up by means of the semi-automated grid-generation process. Not each building façade or roof is a separate wall boundary; instead the surface representation of each imported mesh represents one wall boundary. In the model created in this study, multiple wall boundaries were merged to simplify model use by decreasing the number of boundaries. With the used method it is impractical to assign boundaries to each building façade and roof, as boundaries were defined in the preprocessor for the small meshes where it is not yet possible to identify building roofs and façades. By manually sorting out which boundaries represent a roof, it would be possible to change these boundary conditions and evaluate the large scale implementation of green roofs. Using the same approach, parks and other green zones could be defined in the computational domain. It has to be taken in mind that no wall boundaries and zones should be merged until roofs, parks, or green zones have been defined.

The evaluation of pollutant and smoke dispersion in urban areas fall outside the scope of this study. However, with the right knowledge on required model and grid characteristics these issues might be easier to implement into an urban CFD model, as neither is troubled by assigning boundary conditions to specific buildings surfaces. However, other issues, such as defining sources of pollution and fire are of importance.

4.4 Software errors and limitation: displayed errors

Using the proposed methodology resulted in high computational requirements with respect to preparing GIS data and generating the mesh files. Also, the last step towards creating the computational domain, coupling all mesh files using the "appending case file" function in the CFD code, is a step that should not be underestimated concerning required computational time and error solving. For future reference, the most important errors that occurred during the grid-generation process and software related issues are described in this and the next paragraph.

Error: Increase stack size

Stack size specifies the size of the execution stacks used by each user process, e.g. long select lists, deeply nested stored procedures, and multiple selects (Skybase, 2011). When a stack overflow occurs an error message will be displayed. Therefore, determining the appropriate stack size is a trial-and-error process. Applied to the CFD software this means, that large numbers of, for example interfaces and zones can result in a stack size error.

When starting Ansys from the command level, the following option can be used to increase stack size: -s*xxx*, where *xxx* stands for the stack size in bytes. As a reference, in this project a stack size of 90.000.000 bytes was sufficient.

Error: Cannot allocate additional chunks

The default heap size in Ansys is 100.000 bytes. A 'cannot allocate additional chunks' error can indicate that this heap limit is reached and therefore more memory should be allocated to the process. When starting Ansys from the command level, the option -h*xxx* increases heap size for the cortex, where -cl -h*xxx* increases heap size for Ansys. As a reference, in this project increasing the Ansys stack size to 40.000.000 bytes was sufficient.

Error: Too many listed boundary names

When two meshes are appended, they are connected using interface boundaries, where non-overlapping faces are by default transformed into wall boundaries. These new wall boundaries cannot be merged as this action deletes previously defined mesh interfaces. When a lot of meshes are connected, as was the case for the model of the CBD of Rotterdam, an error is displayed by Ansys: 'wta[1](surface is)'. Expected was that this error is a result of all these additional boundaries exceeding a yet undefined software maximum. This was confirmed by the Ansys helpdesk, who could not reproduce this error using the same software version as Ansys froze, but were able to append the files and come up with a possible viable explanation using the latest Ansys version R13 (Ansys help-desk, 2011). After appending multiple mesh files, the boundary condition list displayed a warning that not all items were listed as there were too many boundary condition names. Expected is that also the applied Ansys version in this study could not handle the number of boundaries. A solution could be to merge more boundaries. However, Ansys does not allow for merging of non-overlapping boundaries. In the end, between 800-1000 meshes could be appended for the three domains that were created before the error occurred. In Figure 4-9 the principle of non-overlapping boundaries and the resulting new boundaries are depicted for a simple 2-D situation.

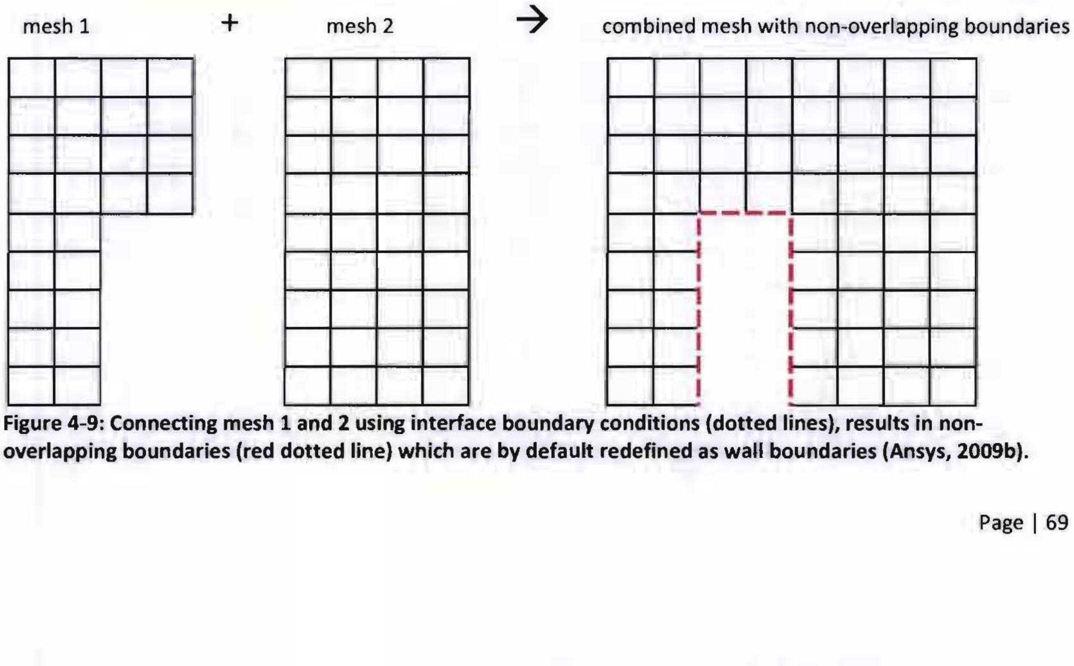

Figure 4-9: Connecting mesh 1 and 2 using interface boundary conditions (dotted lines), results in non-overlapping boundaries (red dotted line) which are by default redefined as wall boundaries (Ansys, 2009b).

4.5 Software errors and limitation: software issues

Grid display

Non-overlapping boundaries are recognized by Ansys as sliding interfaces. This does not affect the calculation, it does however indicate a graphical limitation as these wall boundaries cannot be displayed as a part of the grid leaving holes in the geometry.

Computational time

As previously mentioned, making a large computational domain using GIS data is a very time-consuming process. It could be discussed that the applied methodology in this study has not been optimal, partially due to availability of knowledge on this specific subject. As the project progressed it was observed that not just large mesh files, but especially large stack sizes dramatically increases required computational time during preprocessing. For appending approximately 250 meshes (212 MB of mesh files and 132 MB after appending these in a case file), a pc with 8 GB RAM memory could be used. For further appending of mesh files, the server, a SUN Fire X4150 with 64 GB RAM memory, was used. In addition, there is the realistic possibility that Ansys freezes performing the task of appending multiple large case files with non-default values for stack and heap size. During this study it was attempted to append two meshes of approximately five million cells; after left running for over one week the operation of appending two case files containing approximately 800-1000 meshes each was still not completed by Ansys. Similar issues drastically increased computational time needed by the preprocessor. The large number of mesh volumes, which are a result of using separate mesh edges in the z-direction, affect memory efficiency.

Parallel processing

Another software related issue with respect to required computational time is Ansys' inability to use parallel processing for multiple mesh and data options (Ansys, 2009a). These options are only available for serial cases. The preprocessor Gambit does not have a build-in parallel processing functionality at all.

Memory cache

When Ansys and Gambit are operating they leak memory to the cache. What a cache memory basically does is temporarily store data that is expected to be read soon or multiple times, and by doing so increasing system performance. However, Ansys and Gambit leak data to the cache which then is never deleted until the system reboots. This results in a less efficient use of memory as the memory allocated to the cache cannot be reallocated to another process limiting the servers' capabilities. Since recently, a new script is in use on the BPS server. This script runs on the background and periodically clears the cache memory, increasing memory efficiency.

Inhomogeneous flows

When dealing with urban CFD models the vertical grid resolution can cause problems with the approach flow; due to software related limitations in choosing the roughness constant C_s as described in paragraph 2.3.4, inhomogeneous flows can occur. Implementing user-defined functions and a short approach flow domain helps minimize the artificial acceleration of wind speed profiles but still incurs inaccuracies.

5 Case study city Rotterdam: simulation set-up and results

5.1 Description of urban area and domains

Rotterdam is a city and municipality on the river banks of the Nieuwe Maas in the west of the Netherlands (Figure 5-1). Rotterdam is known worldwide for its port which is the largest in Europe and until 2004 even the busiest in the world. This city is chosen as a case study because of the oceanic influence on its climate, the availability of detailed elevation data, but foremost because of the presence of interesting medium and high-rise buildings in the central business district (CBD). The definition of high-rise can differ per city in the Netherlands. In standards (NEN-EN 1990, 2002) and also in Rotterdam, high-rise is defined as all buildings with a height > 70 m. For the purpose of this study, medium-rise is defined as all buildings between 20 m – 70 m, and low-rise are all buildings < 20 m.

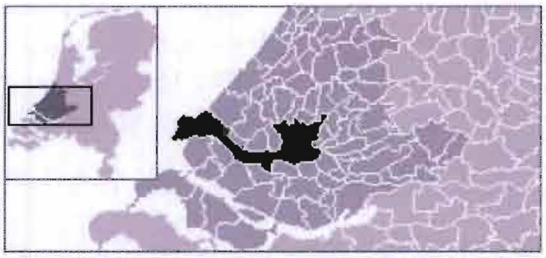

Figure 5-1: Municipality of Rotterdam (en.wikipedia.org/wiki/Rotterdam, accessed: April 2010).

The CBD of Rotterdam is a mix of medium- and high-rise office and residential buildings, aerial pictures are shown in Figure 5-2. Adjacent to the CBD, residential areas are situated that are characterized by predominately low-rise but also some medium-rise buildings. To the northwest of Rotterdam, the Hague Airport is situated. A river just south of the city center connects Rotterdam to the North Sea; Rotterdam lies approximately 30 km inland. Another water body and a park are located to the northeast, respectively known as Kralingse Pond and Forest.

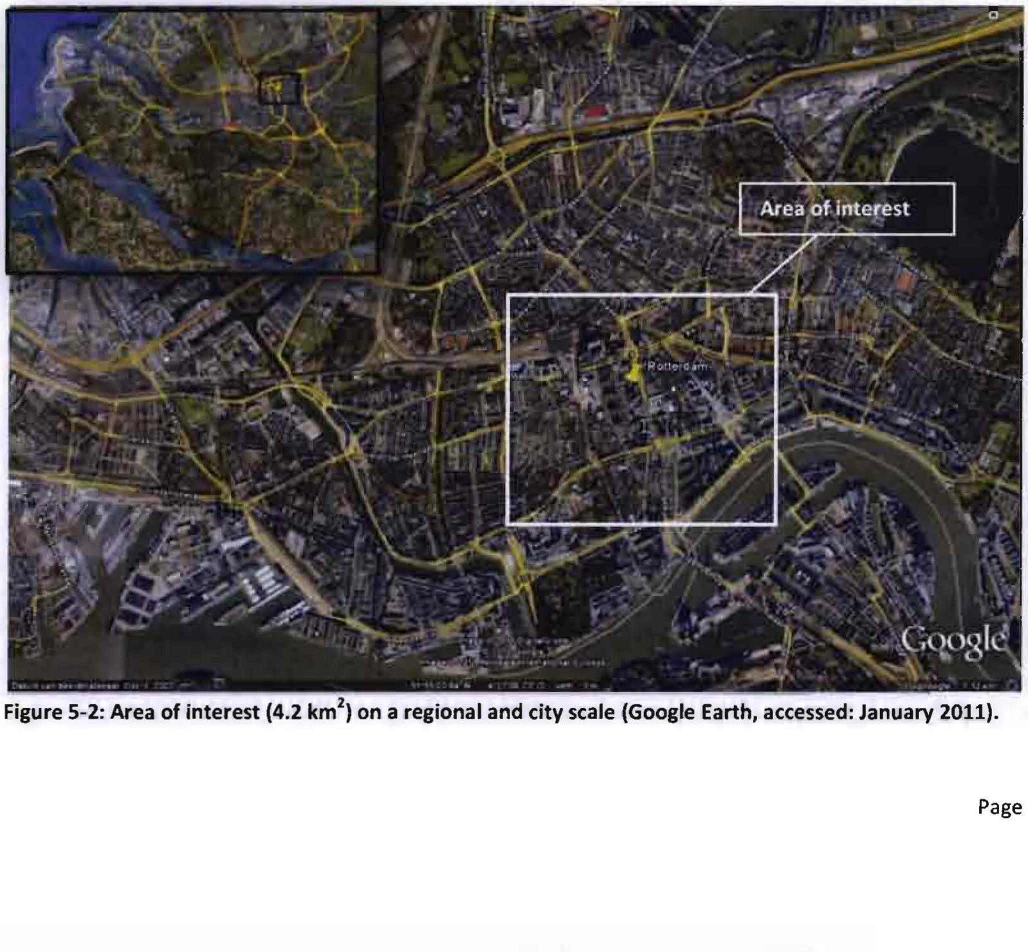

Figure 5-2: Area of interest (4.2 km^2) on a regional and city scale (Google Earth, accessed: January 2011).

The area of interest in this study, as depicted in Figure 5-2, is part of the CBD of Rotterdam and covers an area of approximately 4.2 km^2. This area was chosen because of the interesting high-rise buildings and corresponding population density.

Domains

As described in the paragraph 'project methodology', creating a computational domain of the intended target area with a size of approximately 4.2 km^2 was not feasible. The three smaller domains that were created instead are:

- Domain 1: *Station*, a cluster of high-rise office buildings near the central railway station (size of target area 400 x 400 m^2).
- Domain 2: *Coolsingel*, the main shopping street of Rotterdam (size of target area 300 x 400 m^2).
- Domain 3: A *Residential area* in the center of Rotterdam (size of target area 1000 x 1000 m^2).

Figure 5-3 and Figure 5-4 show the area of interest and target areas on respectively a map and using a bird eye view. Detailed views of domain 1 and 2 are shown in Figure 5-5. The figures below provide an indication of the location of the area of interest with respect to Rotterdam CBD. Appendix A shows the exact location and dimensions of the area of interest and target areas.

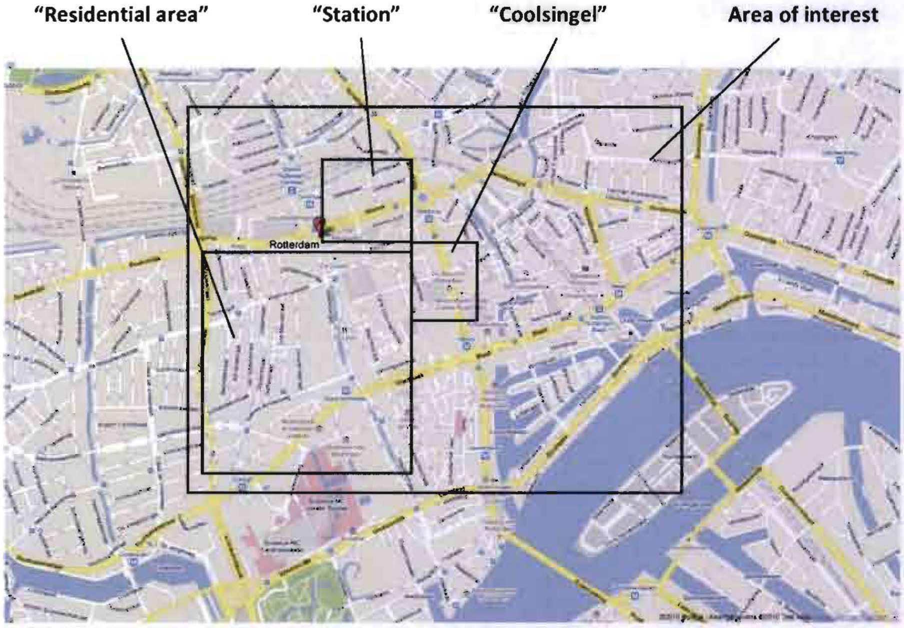

Figure 5-3: Area of interest and target areas: domain 1-3 (maps.google.com).

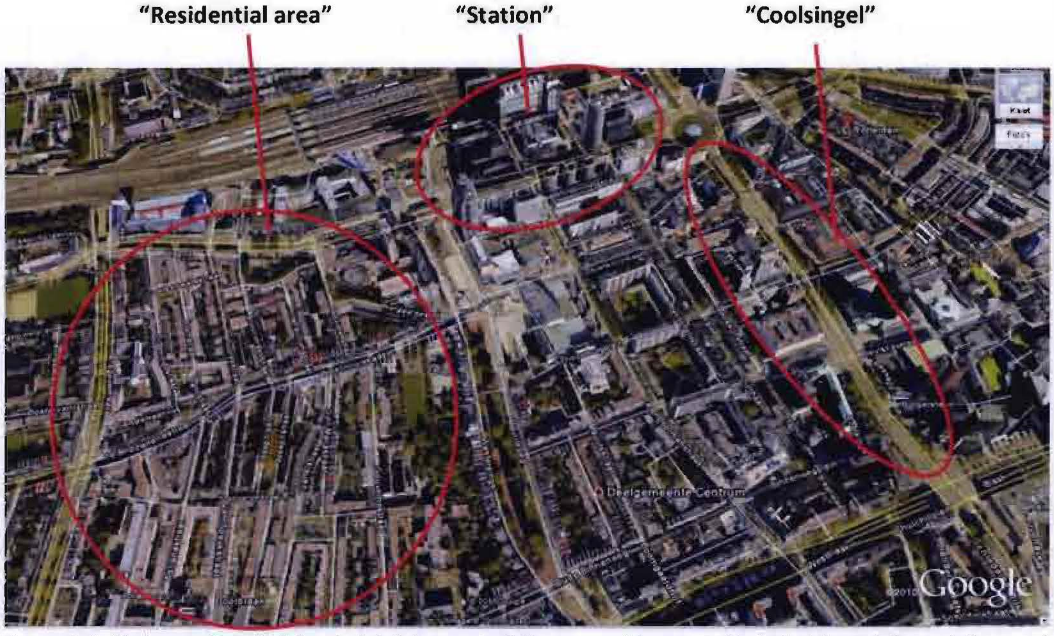

Figure 5-4: Bird eye view (0.5 km height) for part of the area of interest. Encircled from left to right are the three target areas: Residential area, Station, and Coolsingel (Google Earth, accessed: January 2011).

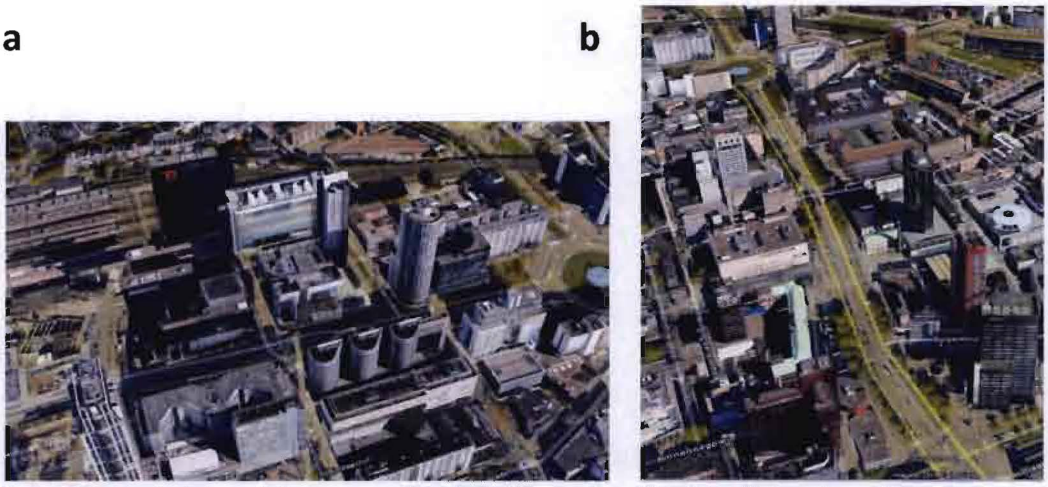

Figure 5-5: Detailed view of a) target area "Station"; b) target area "Coolsingel" (Google Earth, accessed: January 2011).

5.2 Simulation set-up of the case study city

5.2.1 Description of simulation variants

Simulation cases for the case study city Rotterdam are limited to one wind direction; the statistically most common wind direction according to the NPR 6097 (2006) as described in Appendix C. The prevailing wind direction is southwest; wind speeds of 3.0 - 8.0 m/s are most common for this wind direction.

In total nine simulations are conducted; a set of three simulations for each of the three domains.

- Isothermal case; with $U_{ref} = 8$ m/s.
- Wind-induced ventilation flow; with $U_{ref} = 5$ m/s, $\Delta T = 25$ K, and $Ri<<1$.
- Buoyancy-driven flow; with $U_{ref} = 0.1$ m/s, $\Delta T = 25$ K, and $Ri>>1$.

Where, U_{ref} is the approach flow wind speed at a height of 60 meters and ΔT is the difference between T_{wall} and T_{ref}. To determine if a ventilation flow is either wind-induced or buoyancy-driven the Richardson number is adopted. The calculated Ri-numbers (Eq. 2.7) for the non-isothermal simulation variant are presented in Table 5-1. These values where calculated based on the stated U_{ref}, ΔT, and the following values: $\beta = 36 \cdot 10^{-6}$ K^{-1}(concrete), $g = 9.81$ m/s^2, H = 50 m (domain Station), H = 40 m (domain Coolsingel), and H = 10 m (domain Residential area).

Table 5-1: Richardson numbers for the non-isothermal simulation variants.

Domain	*Wind-induced flow*	*Buoyancy-driven flow*
Station	0.017	44.1
Coolsingel	0.014	35.3
Residential Area	0.0035	8.8

5.2.2 Description of grid and model characteristics

Roughness classification

NPR 6097 (Figure C.1 and Figure C.2) in combination with Google Maps (Figure C.3 and Figure C.4) was used to determine the roughness classification (Wieringa, 1992) for the approach domain of the three target areas. Recommended is that a terrain of up to 10 km upstream is taken into consideration when using the updated Davenport classification (Wieringa, 1992). The NPR provides a roughness classification map for a radius of 6 km from a defined coordinate. Based on the figures presented in Appendix C, the aerodynamic roughness length of the region southwest of Rotterdam CBD is estimated to be $y_0 = 1.0$ m.

Grid characteristics

The grid was generated using the described method in paragraphs 4.1 and 4.2. The computational domains of the target area grids were extended based on recommendations in literature (Franke et al., 2007). As a result, a domain height of 6H, upstream domain 1H, lateral domain 1H, and a downstream domain length of 10H was adopted, where H = 163 m, which is the height of the highest building in the three domains.

A structured, body fitted grid, with hexahedral cells is applied. The adopted resolution on the horizontal xy-plane is 5 m for the domain Residential area, and 2 m for the domains Station and Coolsingel. The resolution in the z-direction is 0.8 m at the bottom of the domain, and increases to 2.0 m near the top of the highest building in the domain (H = 163 m). A maximum grid-stretching ratio in the bottom part of the domain of 1.05 is observed. From height 1H to 6H, grid-stretching is 1.2. The computational domain has a total of 123 cells in the z-direction. As a result, domain 'Station' has $4.9 \cdot 10^6$ cells, 'Coolsingel' $3.9 \cdot 10^6$ cells, and 'Residential area' $5.5 \cdot 10^6$ cells.

Boundary conditions

Inlet boundary conditions for wind speed and turbulence are based on the theoretical profiles: $U(y) = \frac{u^*}{\kappa} \cdot \ln\left(\frac{y+y_0}{y_0}\right), = \frac{u^{*2}}{\sqrt{C_\mu}} = 3.33u^{*2}$, and $\varepsilon = \frac{U^{*3}}{(\kappa \cdot (y+y_o))}$ (Eq. 2.2, Eq. 2.4, and Eq. 2.5). The same profiles were used for the pressure-outlet boundaries. With respect to wall boundaries, the roughness parameters C_s and k_s in the approach part of the domain were set adopting a user-defined function to realize a homogeneous approach flow. For wall boundaries in the target areas, the Ansys (2009b) default values C_s = 0.5 and k_s = 0 were adopted. Depending on the type of simulation, isothermal boundaries or an inlet temperature and wall temperatures were specified. The boundary condition 'symmetry' is set for the top of the domain.

Near-wall modeling

As discussed in paragraph 2.3.6, applying the preferred low-Re-number modeling method is not realizable due to the required grid resolution and corresponding computational resources needed. Instead, standard wall functions are adopted for the case study city. For the standard wall function to apply, the center of the first cell from the wall needs to be situated in the log-layer ($30 < y^+ < 1000$) (Ansys, 2009a). The y^+ values for the simulation variants are as presented in Table 5-2. A wide range of 0 – 64,404 for the domains Station and Coolsingel is observed in the simulations. An even wider range of 48 – 641,951 was observed for the domain with the lowest grid resolution, Residential area. Predominantly, y^+ values of the three domains do not exceed a value of approximately 25,000; higher values are observed at very few locations in the grid.

Table 5-2: y^+ values for the simulation variants.

Domain	*Isothermal*	*Wind-induced flow*	*Buoyancy-driven flow*
Station	10 - 48,623	0 - 64,404	0 – 33,488
Coolsingel	4 – 40,959	0 – 50,854	0 – 31,222
Residential area	48 – 52,634	586 – 641,951	385 – 207,939

Thermal effect

In the model a fixed temperature boundary condition is applied; the heat flux from wall to fluid is computed by multiplying the temperature difference by the heat transfer coefficient. The fluid side heat transfer coefficient is calculated based on the local flow field conditions, such as turbulence, temperature, and wind speed profile (Ansys, 2009a). Furthermore, buoyancy is implemented in the CFD model as recommended by the Ansys user's guide (2009a). Note that in this model only convective heat transfer is included. Furthermore, the Boussinesq approximation is used for buoyancy, which is valid because $\beta \cdot (T - T_0) \ll 1$. In this formula, β is the thermal expansion coefficient and $T\text{-}T_0$ the maximum temperature difference. Lastly, the option 'full buoyancy effect' is selected, which enables the inclusion of the influence of buoyancy effects on ε.

Overview

Table 5-3 provides an overview of the applied grid and model characteristics for the case study city Rotterdam.

Table 5-3: Grid and model characteristics for the case study variants.

Feature	Description
Grid	Structured, body fitted, equidistance grid; minimal cell size 0.8 [m]. Cell count: *Station* $4.9 \cdot 10^6$ cells; *Coolsingel* $3.9 \cdot 10^6$ cells; and *Residential area* $5.5 \cdot 10^6$ cells.
Domain	Height 6H, upstream domain 1H, downstream domain 10H; where H = 163 [m]
Solver	Steady 3-D RANS
Convergence criteria	Continuity: $1 \cdot 10^{-11}$, velocities: $1 \cdot 10^{-11}$, energy: $1 \cdot 10^{-11}$ k: $\cdot 10^{-11}$, ε: $1 \cdot 10^{-11}$
Turbulence model	Realizable k-ε model
Discretization	Pressure velocity coupling: scheme (SIMPLE) Spatial Discretization: Gradient (Least Squares Cell Based); Pressure (2nd Order for the isothermal variant and Standard or Body Force Weighted for non-isothermal variants); Momentum, Turbulent Kinetic Energy, Turbulent Dissipation Rate, and Energy (all four 2nd Order Upwind)
Near-wall modeling	Standard wall function, with full buoyancy effects (enables the inclusion of the influence of buoyancy effects on ε). Calculated y^+ values: Isothermal cases $4 < y^+ < 52{,}635$; 5.0 m/s cases $0 < y^+ < 641{,}951$; 0.1 m/s cases $0 < y^+ < 207{,}939$.
Boundary conditions	
Inlet	Velocity-inlet, imposed temperature, theoretical profiles for U, k, and ε; $U(y) = \frac{u^*}{\kappa} \cdot \ln\left(\frac{y+y_0}{y_0}\right)$, $\varepsilon = \frac{U^{*3}}{(\kappa \cdot (y+y_o))}$, $k = \frac{u^{*2}}{\sqrt{C_\mu}} = 3.33u^{*2}$
Outlet	Pressure-outlet, imposed back flow temperature, theoretical profiles for k and ε.
Bottom target area	Imposed wall temperature, no-slip, roughness height $k_s = 0$ [m] and $C_s = 0.5$ [-]
Bottom upstream domain	Imposed wall temperature, no-slip, roughness height $k_s = 0.4$ [m] and $C_s = 8.569$ [-]
Top	Symmetry

5.3 Computational domains

For this study a grid was made for the three target areas Station, Coolsingel, and Residential area. The computational domain for the target area Station is depicted in Figure 5-6. This figure shows the main street (indicated by the arrow) around which the medium-rise and high-rise buildings are clustered.

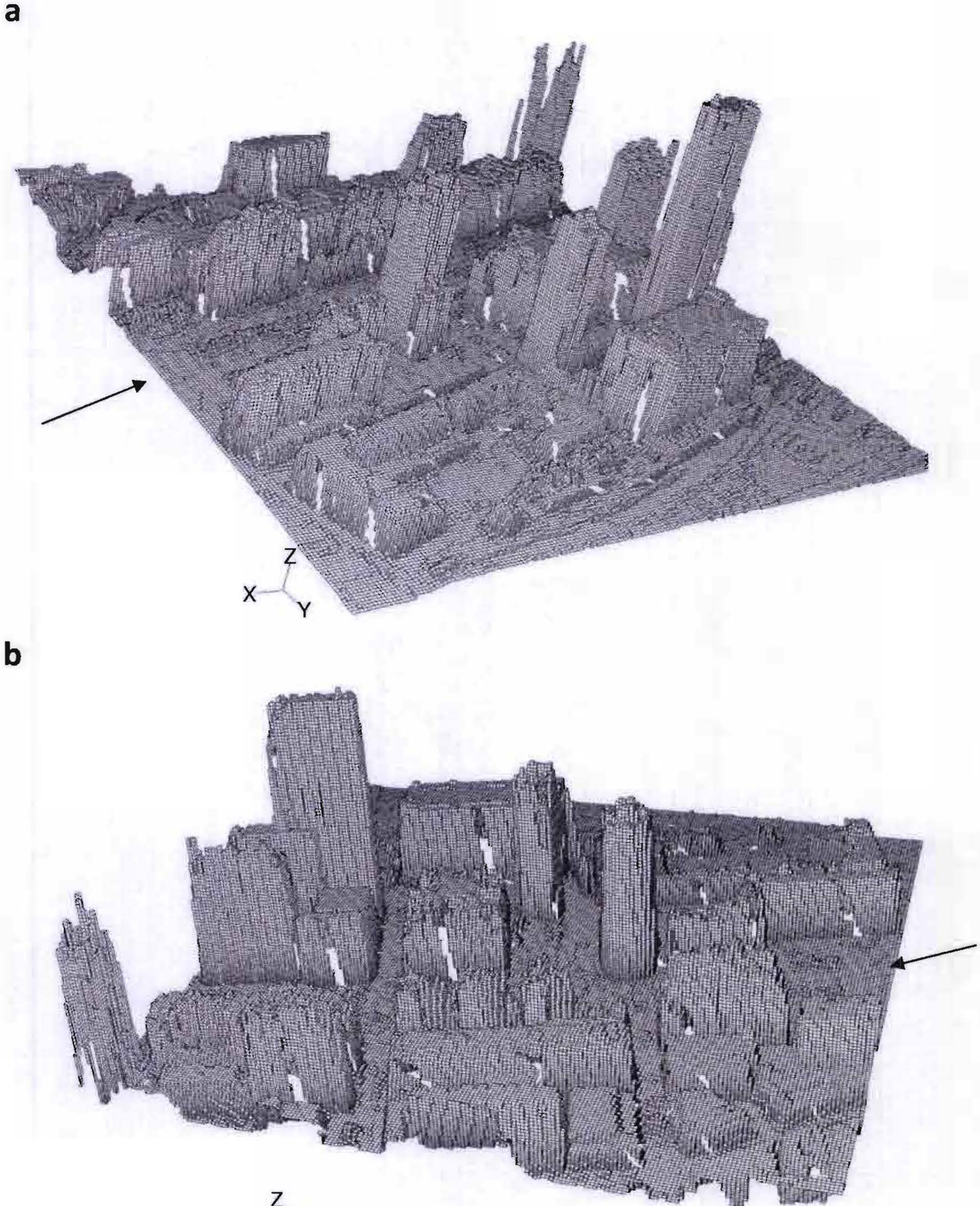

Figure 5-6: Geometrical representation of the domain 'Station'.

The computational domain for the target area Coolsingel is depicted in Figure 5-7. This figure shows the main shopping street of Rotterdam (indicated by the arrow) and the predominantly medium-rise buildings.

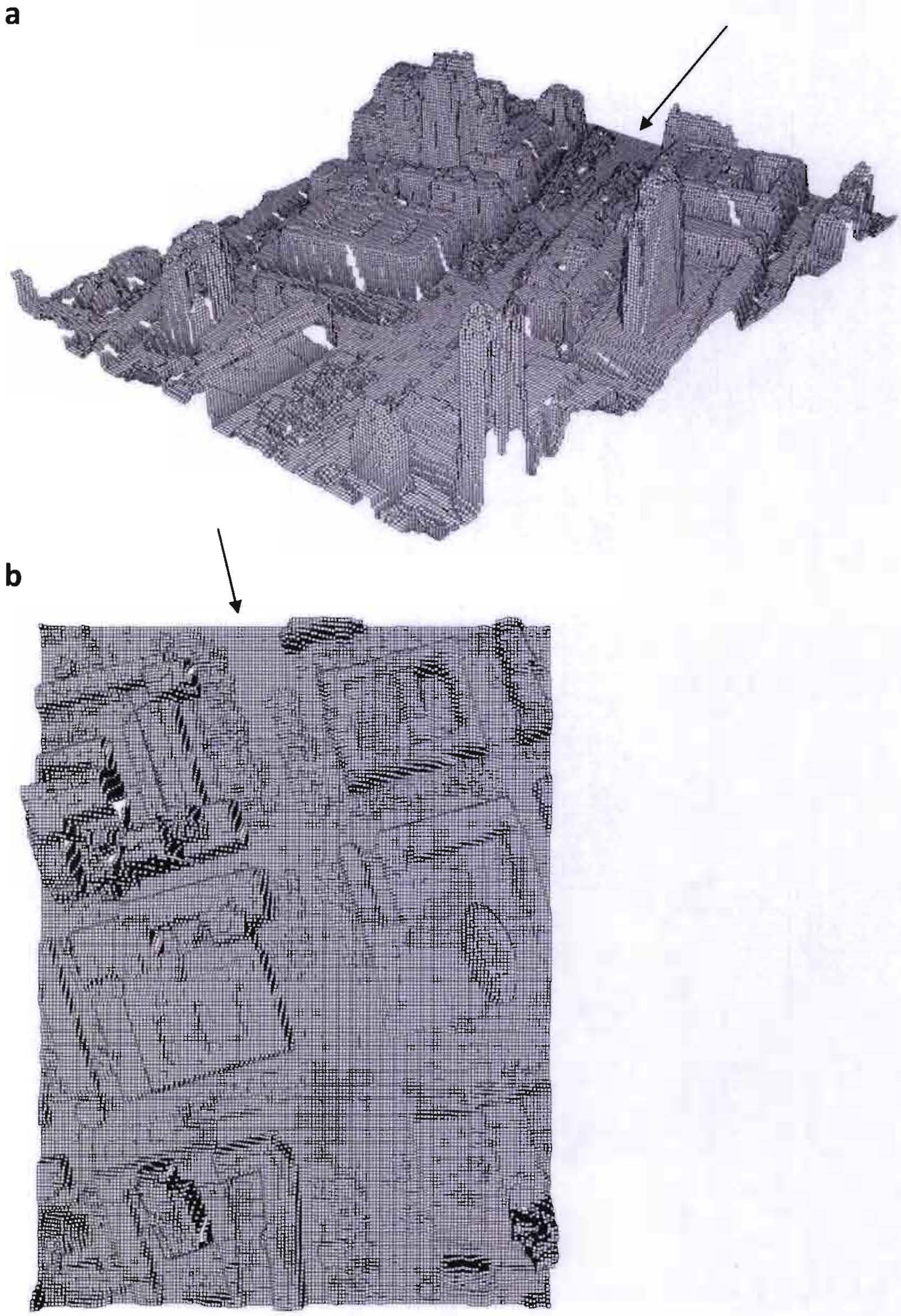

Figure 5-7: Geometrical representation of the domain 'Coolsingel'.

The computational domain for the target area Residential area is depicted in Figure 5-8. This figure shows the residential area that lies adjacent to Rotterdam CBD. On the top right of Figure 5-8a and thus bottom left of Figure 5-8b, some medium-rise buildings can be observed. Furthermore, roads are distinctive features in this domain. No buildings are present in the bottom and top left of the domain, this is a result of the initial subdivision of the domain into smaller parts for the purpose of generating the 4.2 km^2 grid.

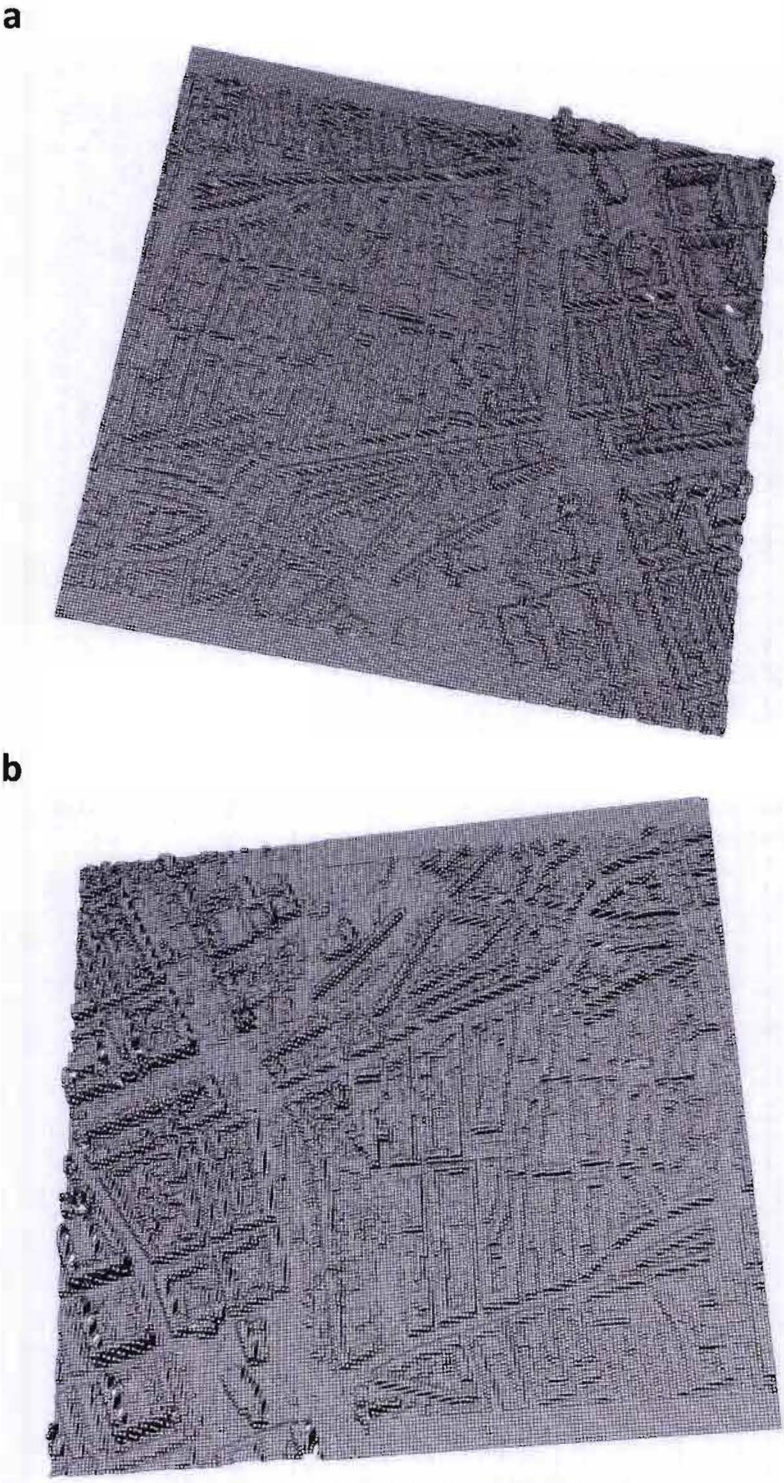

Figure 5-8: Geometrical representation of the domain 'Residential area'.

5.4 Homogeneous ABL flow

Homogeneous ABL flows are possible when the ground roughness is in balance with the vertical wind speed and turbulence profiles. Determined was that adopting an aerodynamic roughness length of y_0 = 1 m was appropriate for the case study city Rotterdam. Due to the software limitations as discussed in paragraph 2.3.4, Ansys only allowed for an aerodynamic roughness length of y_0 = 0.35 m. To assess the influence of the adopted lower ground roughness, the wind speed profiles at the inlet boundary and 30 meters before the target area (at a place where influence of buildings is minimal) are compared for the isothermal case. Figure 5-9 shows that except for a minor acceleration near the ground $z < 20$ m, influence on the wind speed profile is minimal and deemed acceptable for simulation purposes.

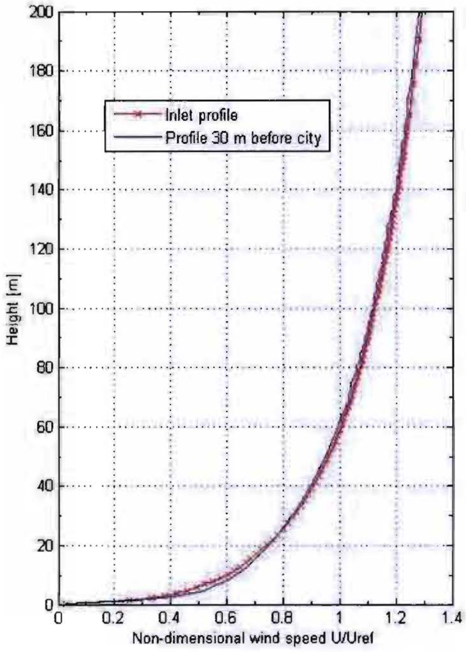

Figure 5-9: Comparison of normalized wind speed profile at the inlet boundary and 30 m before the city (at a location where the profile is not influenced by obstacles from the target area) for an isothermal case.

5.5 Isothermal case

The first set of simulations that was conducted consisted of isothermal variants for the three target areas. For these simulations a reference wind speed at height 60 m of U_{ref} = 8.0 m/s was adopted. Due to the number of variants and the large amount of data that were extracted from the simulations, only a selection of the results is presented below. Also, it has to be taken in mind that the emphasis for this research is placed foremost on the mapping of the applied methodology with respect to developing urban CFD models using GIS data. The complete set of isothermal simulation results are presented in Appendix E.

In Figure 5-10 the vertical planes that are used to present the simulation results in this paragraph, paragraph 5.6, Appendix E, and Appendix F, are shown. The planes in this figure are from the domain Station; planes in the other two domains are set-up similarly.

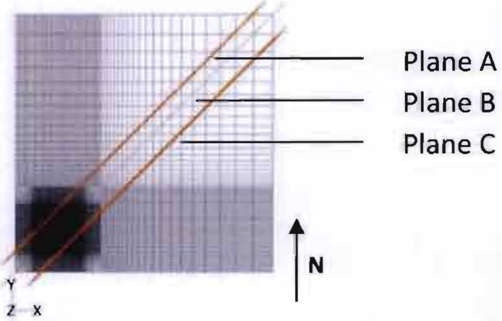

Figure 5-10: Overview of vertical planes in the streamwise direction for domain Station.

In Figure 5-11 the normalized velocity magnitude for two horizontal cross-sections at height 2 m and 30 m for domain Station are shown. At pedestrian height, 2 m, a wind speed amplification factor of 2.5 - 3.5 is observed in the main street canyon (indicated by the arrow). The strongest amplification occurs as a result of a corner flow near a building at about ⅔ of the length of the street canyon (near the tip of the arrow). Very low wind speeds are observed in stagnation areas behind buildings and in areas blocked by obstacles. The square that has been drawn at the top right of the domain is a good example of an area where both phenomena occur. An example of a stagnation area in front of a building can be seen in the bottom left corner of the domain.

At a height of 30 m (Figure 5-11b), the wind flow is less strongly affected by the street canyon, no amplification occurs here. Stagnation areas before and behind tall buildings are still observed. The area affected by the building depends on the height of the building and building configuration preceding the building. A good example is the large building in the top of the domain (encircled). The approach flow for this building is relatively calm, as it is sheltered by a cluster of other tall buildings that change the wind flow and decrease wind speed. This figure also clearly shows a corner flow with increased wind velocity at two buildings in the top left of the domain, a result of the absence of obstacles upstream. Based on the figures below, it can be stated that the amplification near the ground, where the wind flow is influenced by a high concentration of buildings and obstacles, is much higher than higher up in the domain; a maximum amplification of respectively 3.5 and 1.4 is observed.

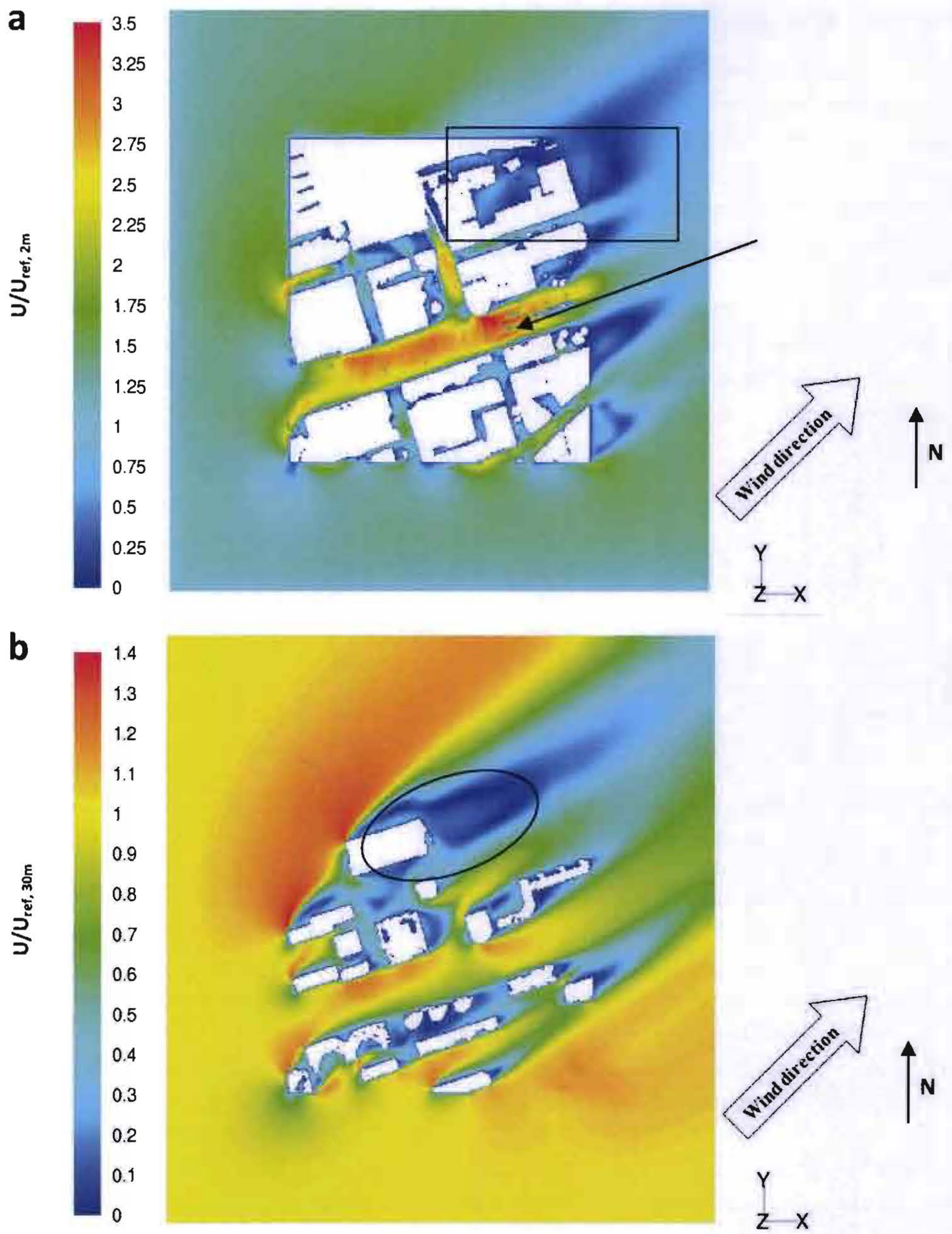

Figure 5-11: Contours of normalized mean velocity magnitude U/U_{ref} for horizontal cross-section for domain Station at heights a) 2 m ($U_{ref, 2m}$ = 2.14 m/s) and b) 30 m ($U_{ref, 30m}$ = 6.68 m/s). Note that U_{ref} = 8.0 m/s was not used in this figure, instead U_{ref} is height dependent, the local wind speed at the corresponding height from the inlet profile is adopted.

In Figure 5-12 the normalized velocity magnitude on a vertical plane in the streamwise direction for domain Station is shown. It can be observed that the wind speed behind each building decreases on the leeward side, also, the larger the building, the larger the wake. More complex wind flows occur when buildings lie in each other's wake and stagnation areas. On the right side of the domain (indicated by the square), a thick layer of low wind speed is observed. This is not only a result of the buildings visible in this vertical plane, but foremost of the building configuration in this part of the domain as was previously indicated in Figure 5-11. Also noticeable, are the areas of low wind speed where the target area connects to the approach and wake domains, e.g. at the right side of the domain (indicated by the triangle). As a result of height differences in the target area, it is difficult to make flawless connections to the approach and wake domain on all sides of the target area.

With respect to showing vertical planes in a 3-D figure of the domain, both a figure with and without a mesh are shown. This approach is adopted as only showing the figure with a mesh, can give a wrong impression of the situation. A good example is tall building in Figure 5-12a that appears to have no wake (as indicated by the arrow). However, when the figure is displayed without the mesh, it becomes clear that this building does not even lie in the vertical plane.

Lastly, wind flow around the building on the left side of the domain is scrutinized (encircled). What can be observed is that because of holes in the geometry, as described in paragraph 4.4 and 4.5, the insides of buildings are displayed where wind speed is equal to zero. Due to the applied method, this graphical issue can unfortunately not be overcome.

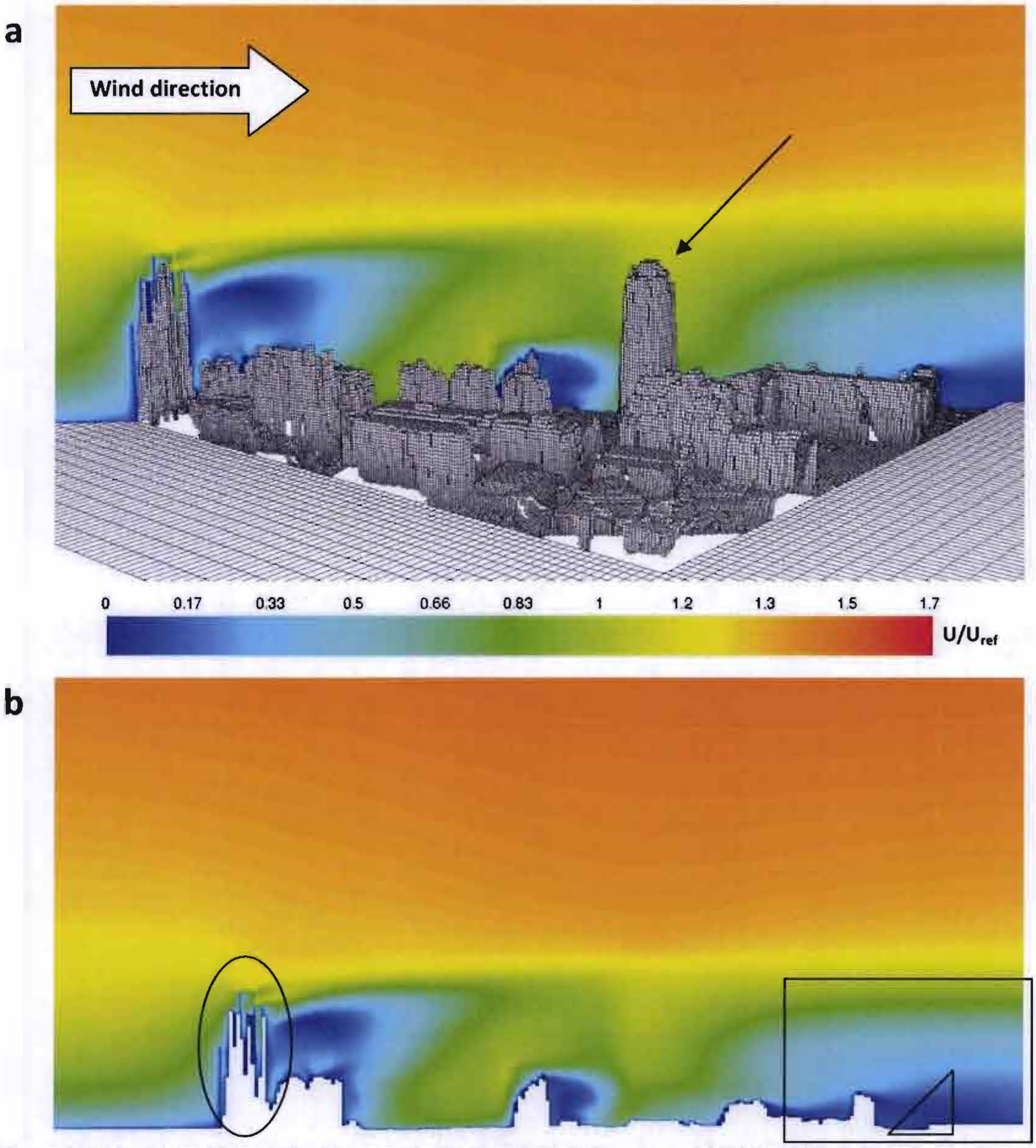

Figure 5-12: Contours of normalized mean velocity magnitude U/U_{ref} at vertical plane B for domain Station, U_{ref} = 8 m/s.

In Figure 5-13 the normalized velocity magnitude for two horizontal cross-sections at height 2 m and 10 m for domain Residential area are shown. At pedestrian height, 2 m, high wind speed amplification is restricted to only a few streets in the domain, some of which are encircled. Predominantly however, wind speed is decreased due to the high concentration of buildings, which appear to block the wind flow. Similar to the domain Station, the strongest amplification occurs in the form of a corner flows (indicated by the arrow), a result of the absence of obstacles upstream. Very low wind speeds are observed in stagnation areas behind buildings and in areas blocked by obstacles. Figure 5-13a also shows that the wake behind tall buildings is bigger compared to lower buildings. To illustrate this, the wake behind buildings in the top left of the domain (low-rise) and buildings in the top right of the domain (medium-rise) can be compared. Consequently, the same is observed at a height of 10 m (Figure 5-13b). Based on the figures below, it can be stated that the amplification at pedestrian level is much higher than higher up in the domain; a maximum amplification of respectively 2 and 1.2 is observed.

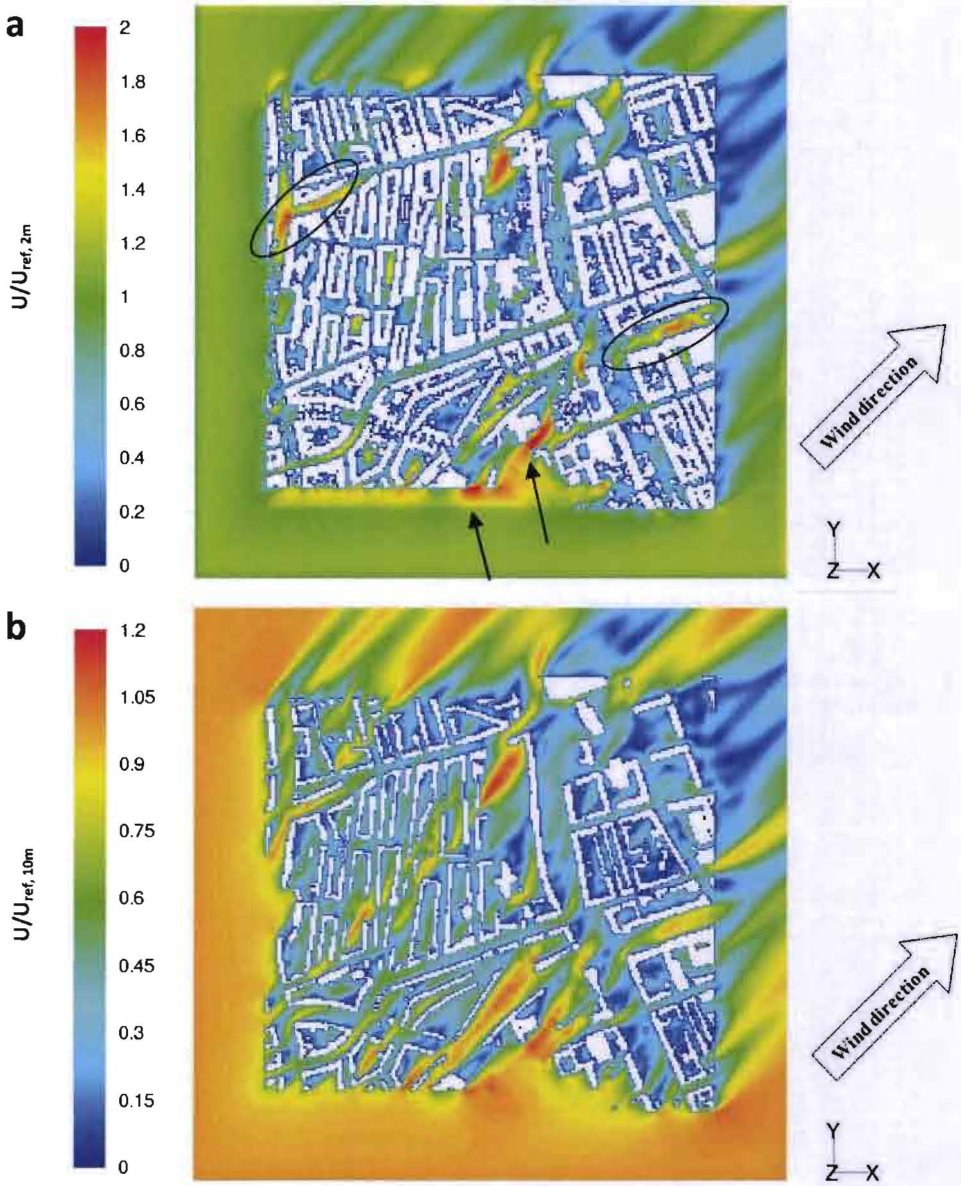

Figure 5-13: Contours of normalized mean velocity magnitude U/U_{ref} for horizontal cross-section for domain Residential area at heights a) 2 m ($U_{ref,\,2m}$ = 2.14 m/s) and b) 10 m ($U_{ref,\,10m}$ = 4.38 m/s). Note that U_{ref} = 8.0 m/s was not used in this figure, instead U_{ref} is height dependent, the local wind speed at the corresponding height from the inlet profile is adopted.

In Figure 5-14 the normalized velocity magnitude on a vertical plane in the streamwise direction for domain Residential area is shown. As these figures depict a larger target area compared to the figures for domain Station, observations and description of these figures will focus on the influence of the urban area on the vertical wind speed profile. It can be observed that initially the wind speed profile seems quite undisturbed and unchanged in the streamwise direction. However, when taking a closer look, a slight acceleration of the wind speed profile at the top region of the domain is observed. On the other side, a deceleration of the wind speed profile is observed behind the target area. To illustrate this, the height at which $U/U_{ref} \approx 0.75$ at, 1) the domain inlet and 2) approximately 80 m behind the target area are marked by a dotted line in Figure 5-14b. These lines are extended to the middle of the domain, so these heights can be compared; a deceleration of the wind speed profile in the lower part of the domain is observed.

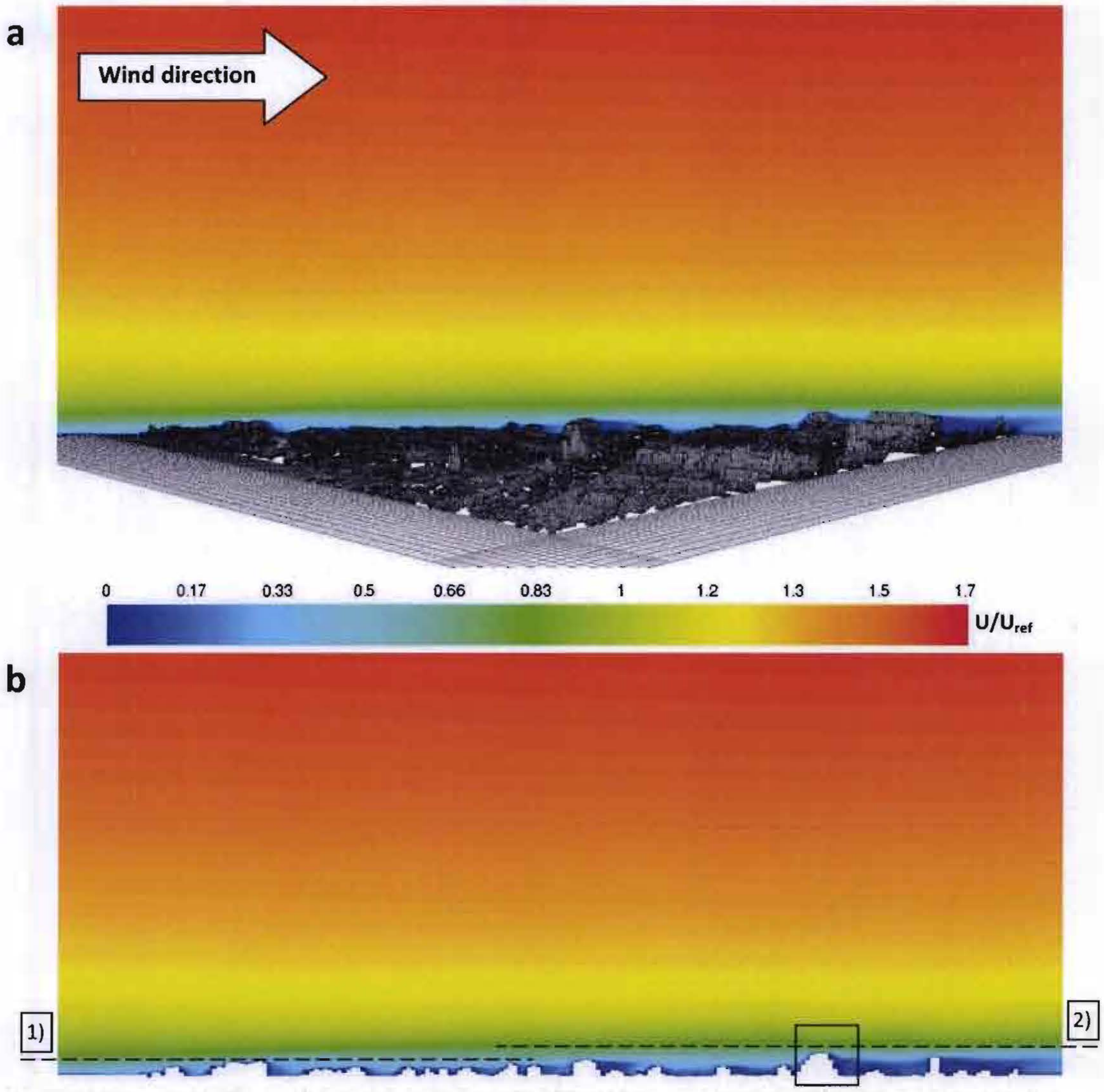

Figure 5-14: Contours of normalized mean velocity magnitude U/U_{ref} at vertical plane B for domain Residential area, U_{ref} = 8 m/s.

5.6 Non-isothermal cases

For the non-isothermal simulation variant, a reference wind speeds at height 60 m of U_{ref} = 5.0 m/s for wind-induced flows and U_{ref} = 0.1 m/s for buoyancy-driven flows were adopted. The inlet temperature was set to match the reference temperature T_{ref} = 10 °C, wall temperatures in the target area were set to T_{wall} = 35 °C; resulting in ΔT = 25 °C. Due to the number of variants and the large amount of data that was extracted from the simulations, only a selection of the results is presented below. The complete set of non-isothermal simulation results are presented in Appendix F.

5.6.1 Wind-induced flow

In Figure 5-15 the normalized velocity magnitude in a vertical plane for domain Coolsingel are compared for a) the wind-induced and b) the isothermal simulation. The wind-induced variant is non-isothermal and as a result the wind flow is, be it only minimal, influenced by thermal effects. For the comparison it has to be taken into account that the U_{ref} for the isothermal and non-isothermal simulation are not the same. It can be observed from the two figures below that the most striking difference between the variants is the size of the wake behind the buildings (indicated by a square). This can be explained by the difference in reference wind speed. In addition, it can be stated that the most pronounced difference in wind flow pattern occur locally, at locations where wind speed is low, and as a results the thermal effects become more dominant.

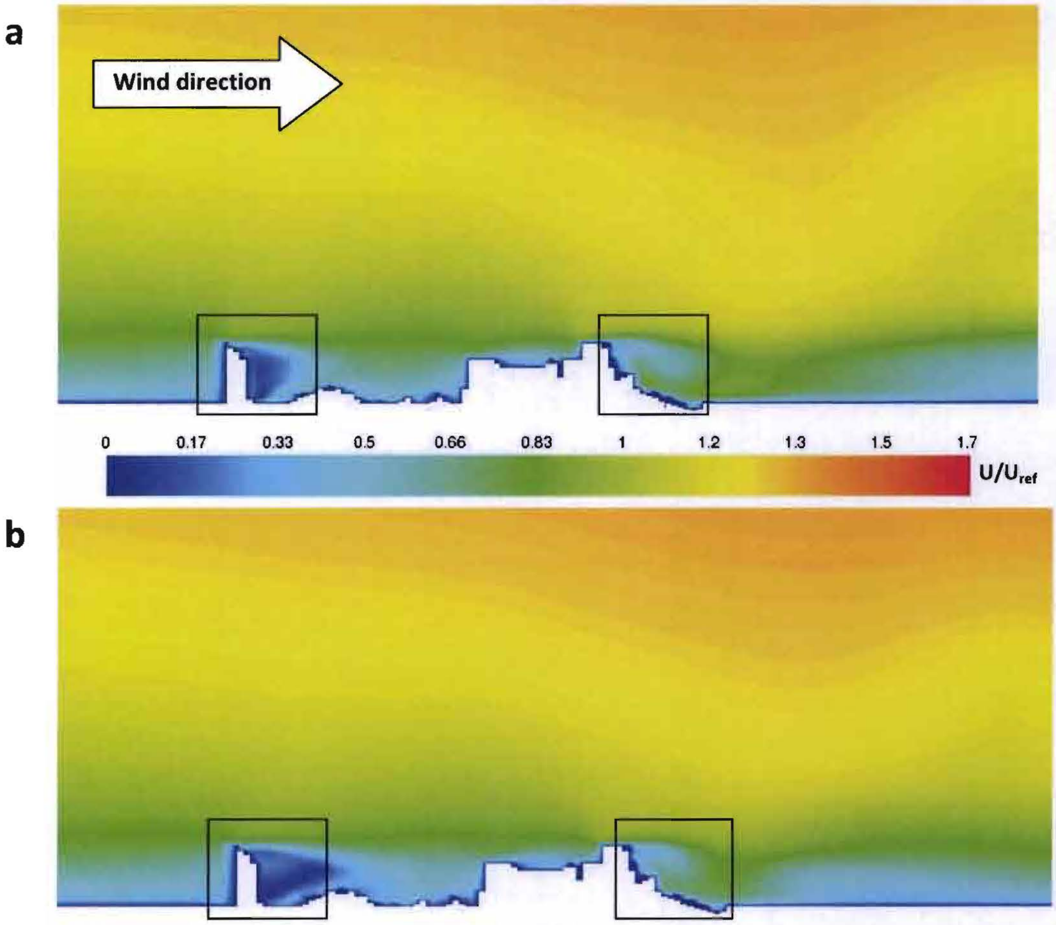

Figure 5-15: Contours of normalized mean velocity magnitude U/U_{ref} at vertical plane C for domain Coolsingel, a) U_{ref} = 5.0 m/s and b) U_{ref} = 8.0 m/s (isothermal variant).

In Figure 5-16 the normalized temperature for two horizontal cross-sections at height 2 m and 20 m for domain Coolsingel are shown. At pedestrian height, 2 m, a temperature amplification factor of 1.1 - 1.4 is observed in most parts of the domain. The strongest amplification occurs in areas of low wind speed (two of which are indicated by a square). The same observation is made at a height of 20 m (Figure 5-16b). In general the air temperature at this height is slightly lower as it is less affected by the surface temperatures of streets and pavements at ground level. What can also be observed at both heights, are increased temperatures in the wake of buildings. In both figures, two of these low wind speed areas are indicated by a square.

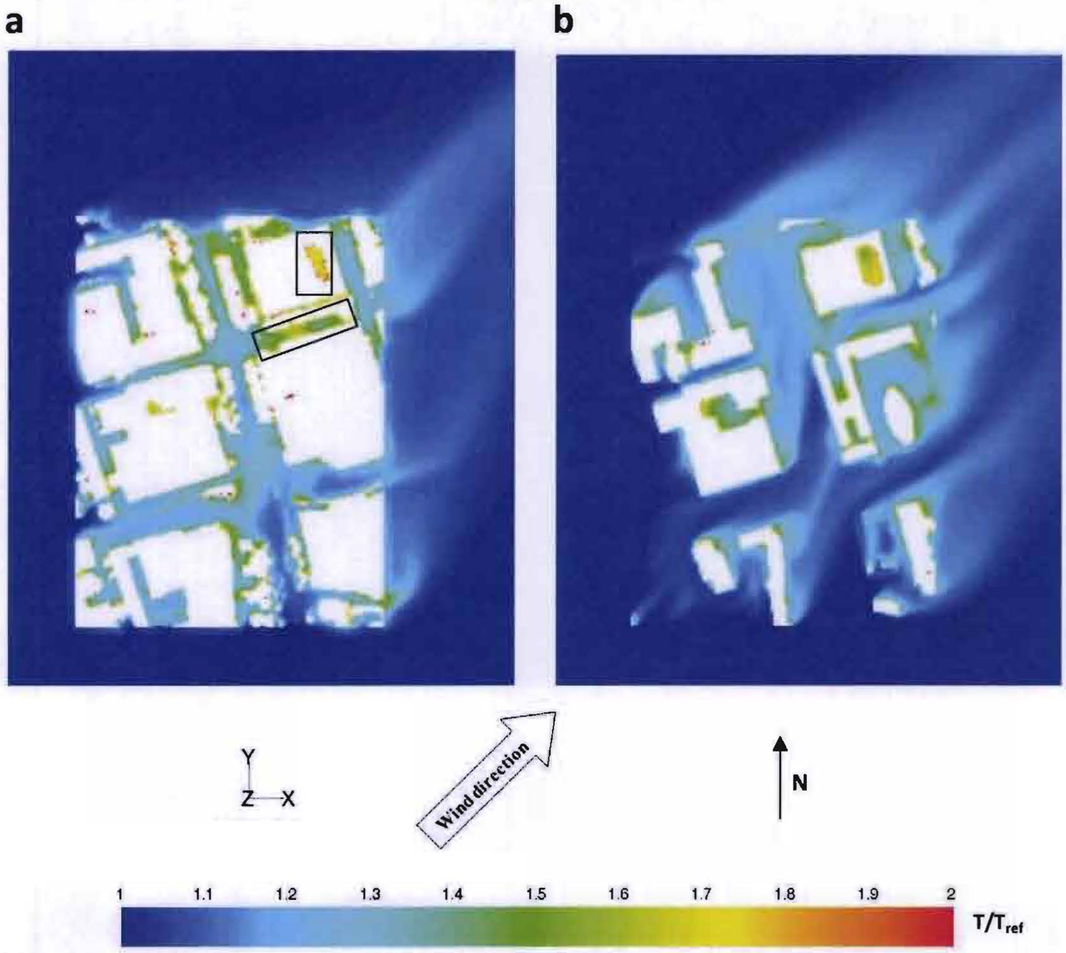

Figure 5-16: Contours of normalized temperature T/T_{ref} for horizontal cross-section for domain Coolsingel at heights a) 2 m; b) 20 m, T_{ref} = 10 °C.

In Figure 5-17 the normalized temperature in a vertical plane in the streamwise direction for domain Coolsingel is shown. A strong influence of the 35 °C building surfaces on the air temperature can be observed. The tall building indicated by the left arrow in Figure 5-17b for example, influences air temperature in the streamwise direction until several times its own height. This heated air reaches the next cluster of buildings (indicated by the right arrow), and heated air is transported until far behind the target area.

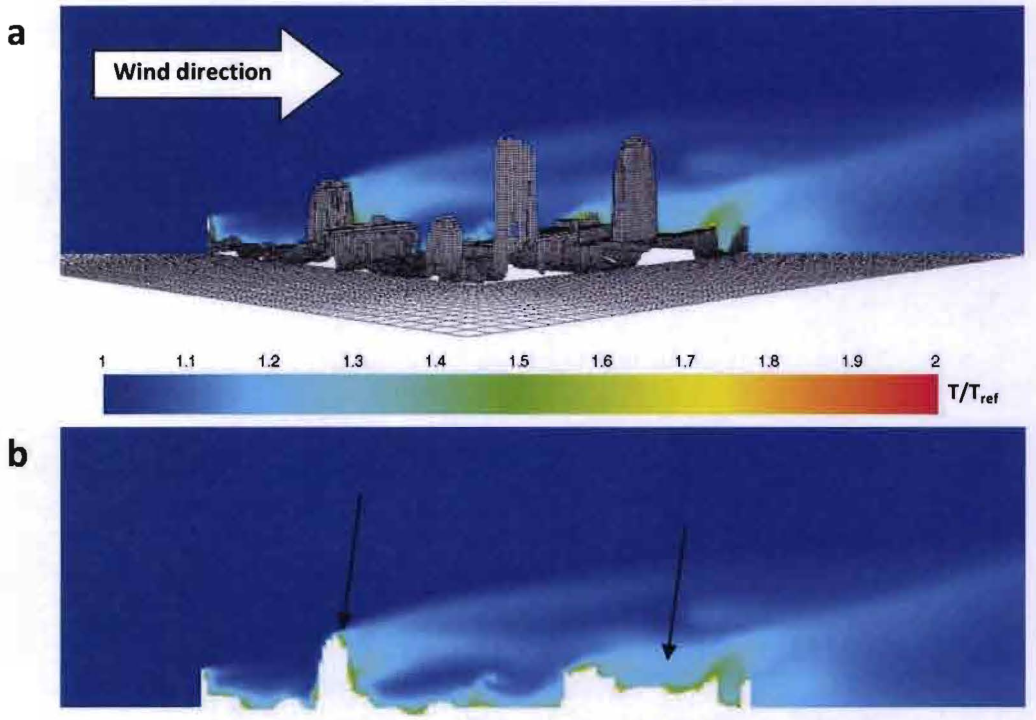

Figure 5-17: Contours of normalized temperature T/T_{ref} at vertical plane B for domain Coolsingel, T_{ref} = 10 °C.

5.6.2 Buoyancy-driven flow

Domain *Station*

In Figure 5-16 the normalized temperature for two horizontal cross-sections at height 2 m and 30 m for domain Station are shown. At both heights a temperature amplification factor of 1.1 - 1.4 is observed in most parts of the domain, which is incidentally quite similar to the simulation variants with a wind-induced ventilation flow. It can be seen that no wake occurs behind (tall) buildings. Instead, a ring with increased temperature occurs around the target area. This phenomenon (indicated by the arrow) is most clearly depicted in Figure 5-18b at a height of 30 m. That no wake is present suggests an upward flow direction as can be expected of a buoyancy-driven flow.

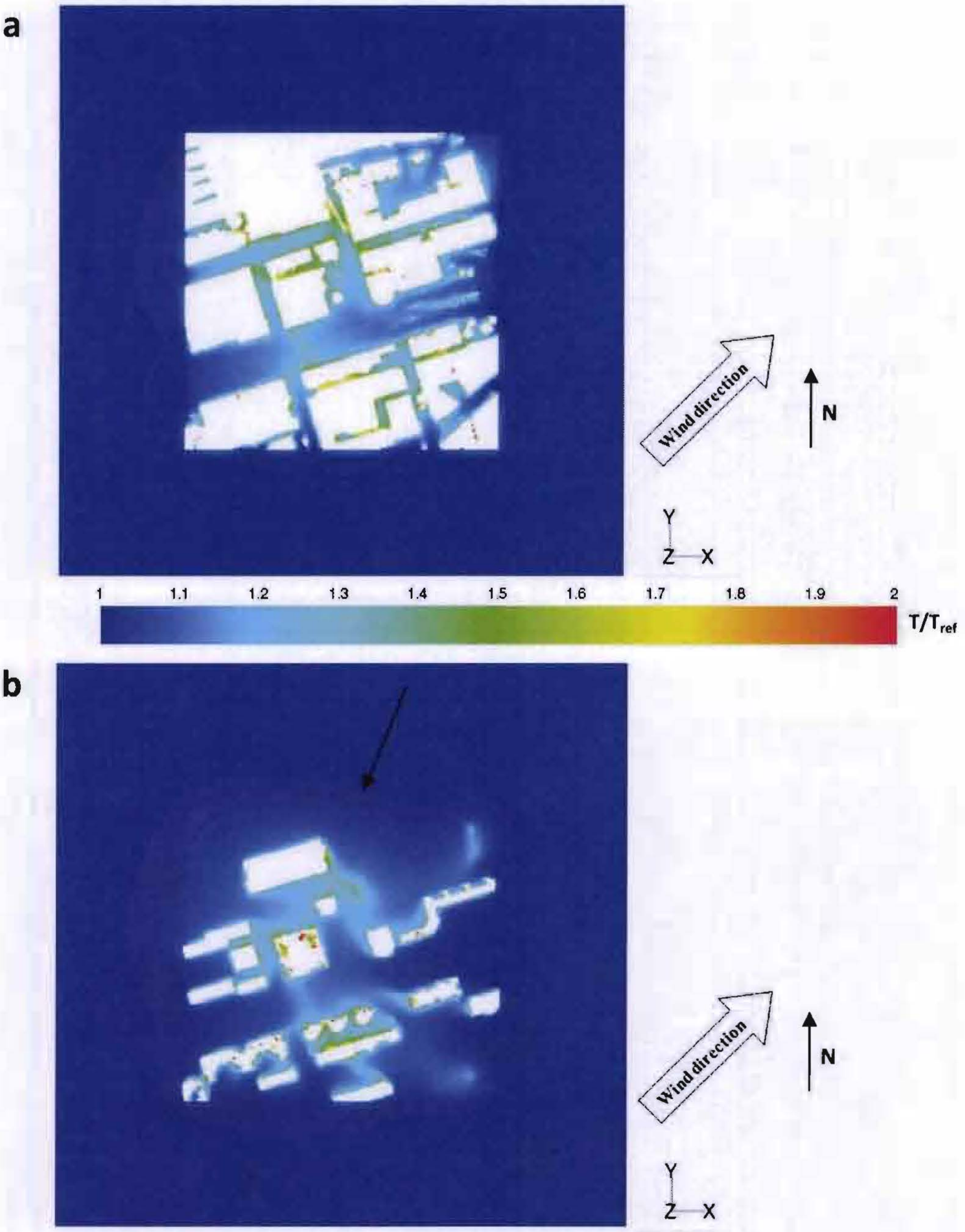

Figure 5-18: Contours of normalized temperature T/T$_{ref}$ for horizontal cross-section for domain Station at heights a) 2 m; b) 30 m, T$_{ref}$ = 10 °C.

In Figure 5-19 the normalized velocity magnitude in a vertical plane in the streamwise direction for domain Station is shown. In addition, vectors have been drawn to depict the wind flow pattern above the target area. It can be seen that the buoyancy-driven flow induces a high-velocity upward ventilation flow. This translates into velocities of > 2.5 m/s in the region high above the target area. It should also be noted that, as was the intention, the inlet profile with U_{ref} = 0.1 m/s is dominated by the buoyancy-driven flow from the target area.

Striking is the large vortex that is predicted to the left of the target area. This is the first indication that the symmetry boundary condition adopted for the top of the domain is unsuitable for the simulation of buoyancy-driven ventilation flows. The effect on the wind flow pattern and possible amplification of the wind speed as a result of this boundary condition are scrutinized in paragraph 6.2 of the discussion chapter. Thus far, it can be stated that this observation strongly questions the accuracy and reliability of the simulation.

Besides high-velocity buoyancy-driven flows in the domain, high-velocity areas can be identified in lower parts of the domain, some have been indicated by squares in Figure 5-19b.

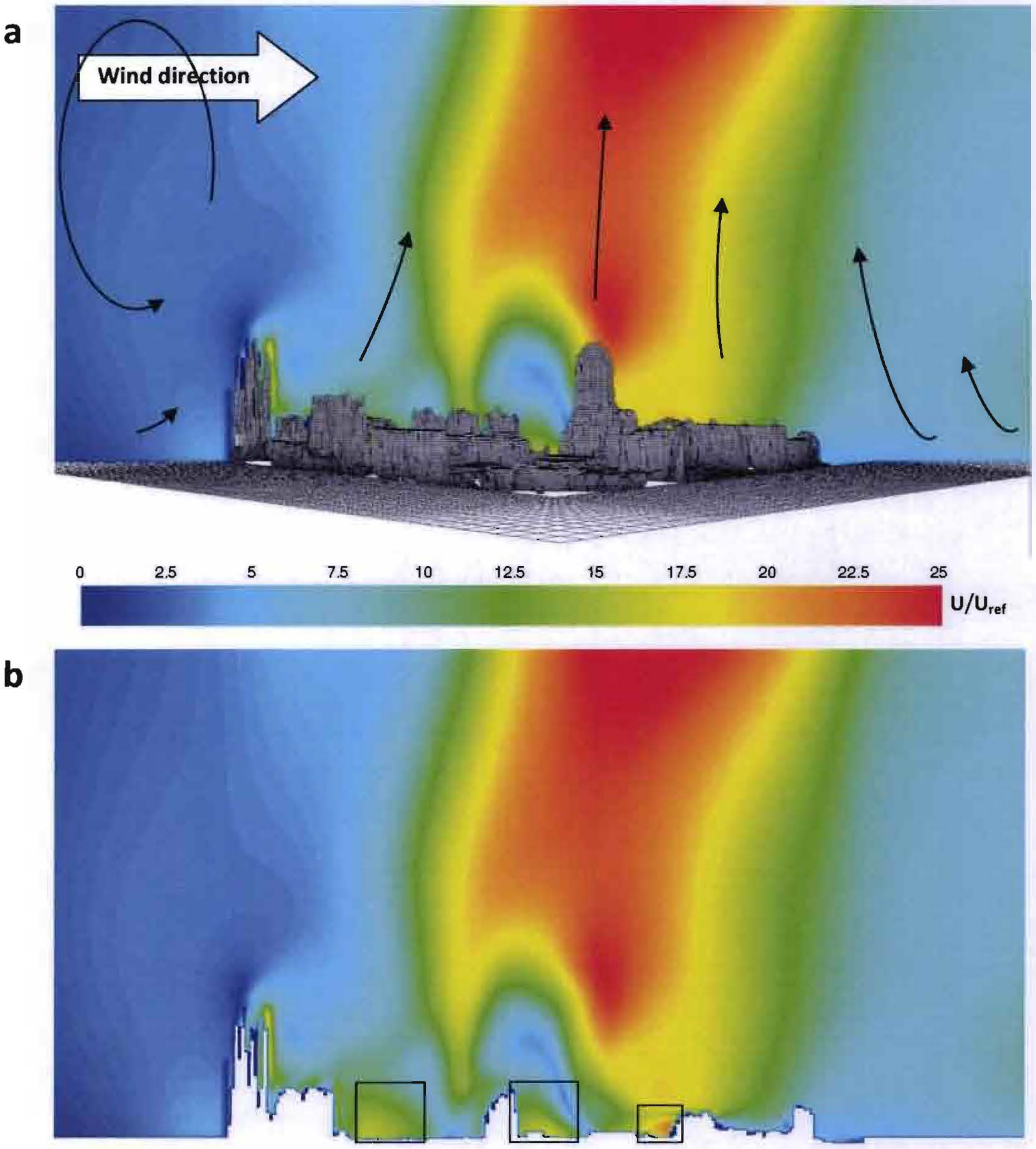

Figure 5-19: Contours of normalized mean velocity magnitude U/U_{ref} at vertical plane B for domain Station, U_{ref} = 0.1 m/s.

Interesting to see is what the effect of the buoyancy-driven flow is on the temperature distribution in the target area Station. Contours of normalized temperature in a vertical plane in the streamwise direction for domain Station are shown in Figure 5-20. As previously observed in the horizontal cross-sections, an amplification of 1.1 - 1.4 occurs in the region $z < 30$ m. Locally, in the vicinity of buildings, even higher values are observed. In the figure below it can be seen that air temperatures also noticeably increase at heights $z > 30$ m, and not in just one part of the domain, but above almost the entire target area. This increase in air temperature is most pronounced in the middle of the domain, where the buoyancy-driven flow converges. Lastly, it should be stated that accuracy of the predicted air temperature strongly depends on the predicted wind flow (Figure 5-19). Previously it was argued that wind flow pattern was strongly influenced by the adopted symmetry boundary condition for the top of the domain.

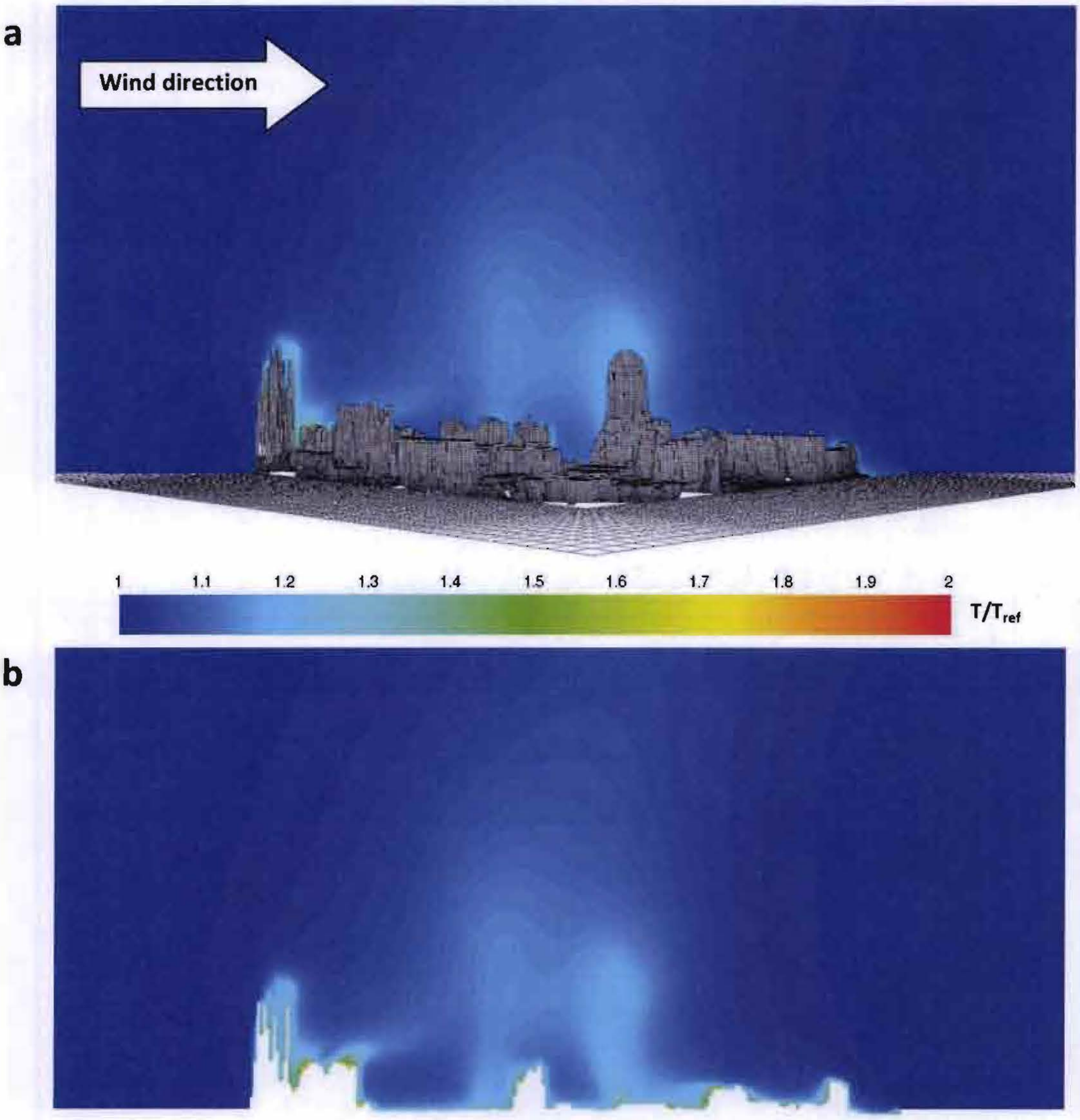

Figure 5-20: Contours of normalized temperature T/T_{ref} at vertical plane B for domain Station, T_{ref} = 10 °C.

Domain *Residential area*

In Figure 5-21 the normalized temperatures for two horizontal cross-sections at height 2 m and 20 m for domain Residential area are shown. At both heights a temperature amplification factor up to 1.4 is observed in most parts of the domain. However, amplifications up to 1.7 at pedestrian level are no exception. It can be seen that no wake is observed behind any of the buildings. A low U_{ref} combined with the observation that no wake is present suggests an upward flow direction as can be expected of a buoyancy-driven flow.

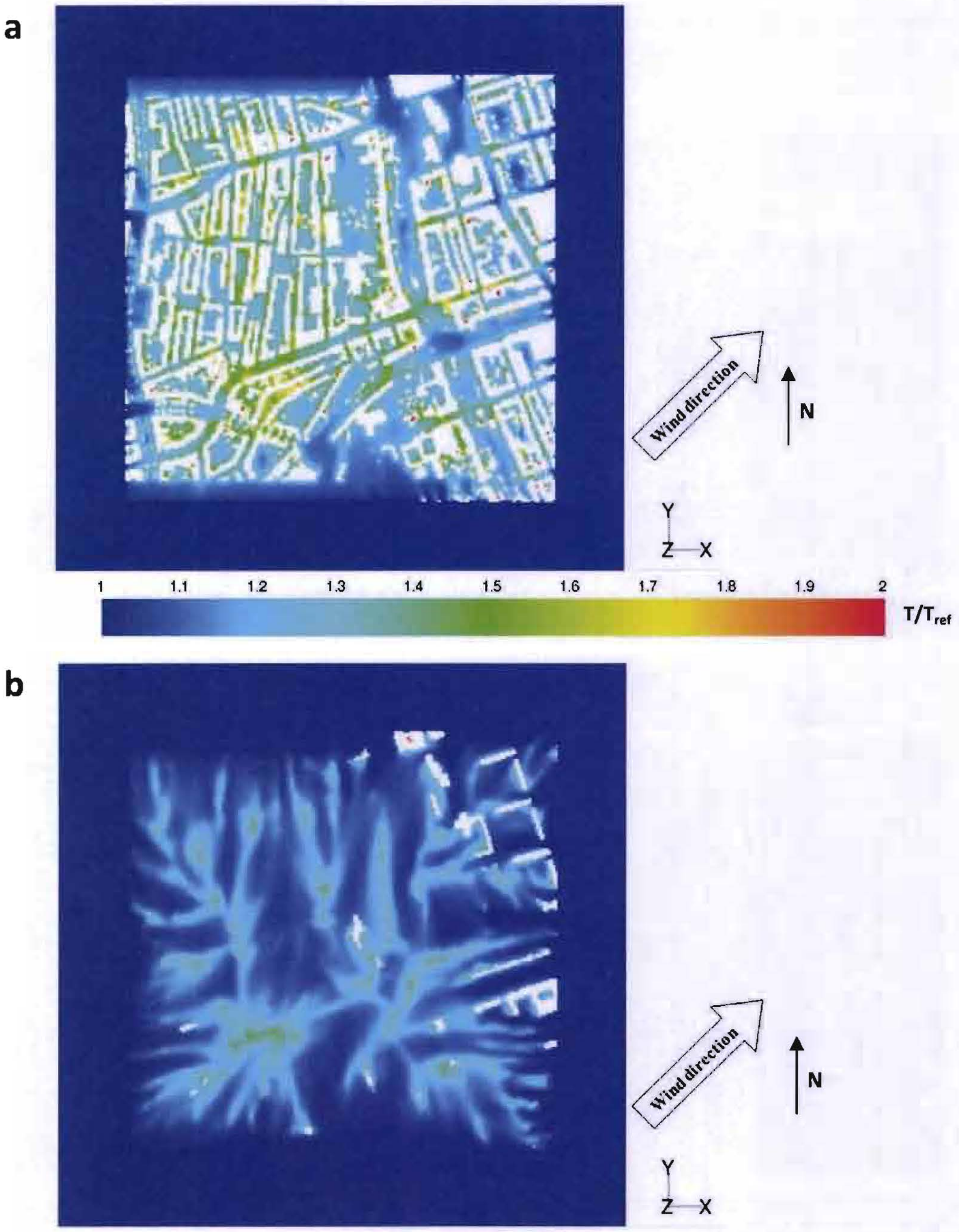

Figure 5-21: Contours of normalized temperature T/T_{ref} for horizontal cross-section for domain Residential area at heights a) 2 m; b) 20 m, T_{ref} = 10 °C.

In Figure 5-22 the normalized velocity magnitude in a vertical plane in the streamwise direction for domain Residential area is shown. In addition, vectors have been drawn to depict the wind flow pattern above this target area. Similar to the domain Station, a high-velocity upward ventilation flow (W component wind speed) with wind speeds of > 2.5 m/s are observed. This is quite a high value with respect to the reference wind speed of 0.1 m/s (U component wind speed). A difference between this and the previously presented domain is that in the relatively large domain Residential area, the upward flow appears to be split into two parts. The vortex that is observed upstream of the domain is smaller in diameter than was observed for the domain Station. For this simulation, again, it should be noted that the symmetry boundary condition affects the wind flow above the urban area. As previously mentioned, the accuracy and reliability of this simulation, as a result of the adopted top boundary condition, will be discussed in paragraph 6.2.

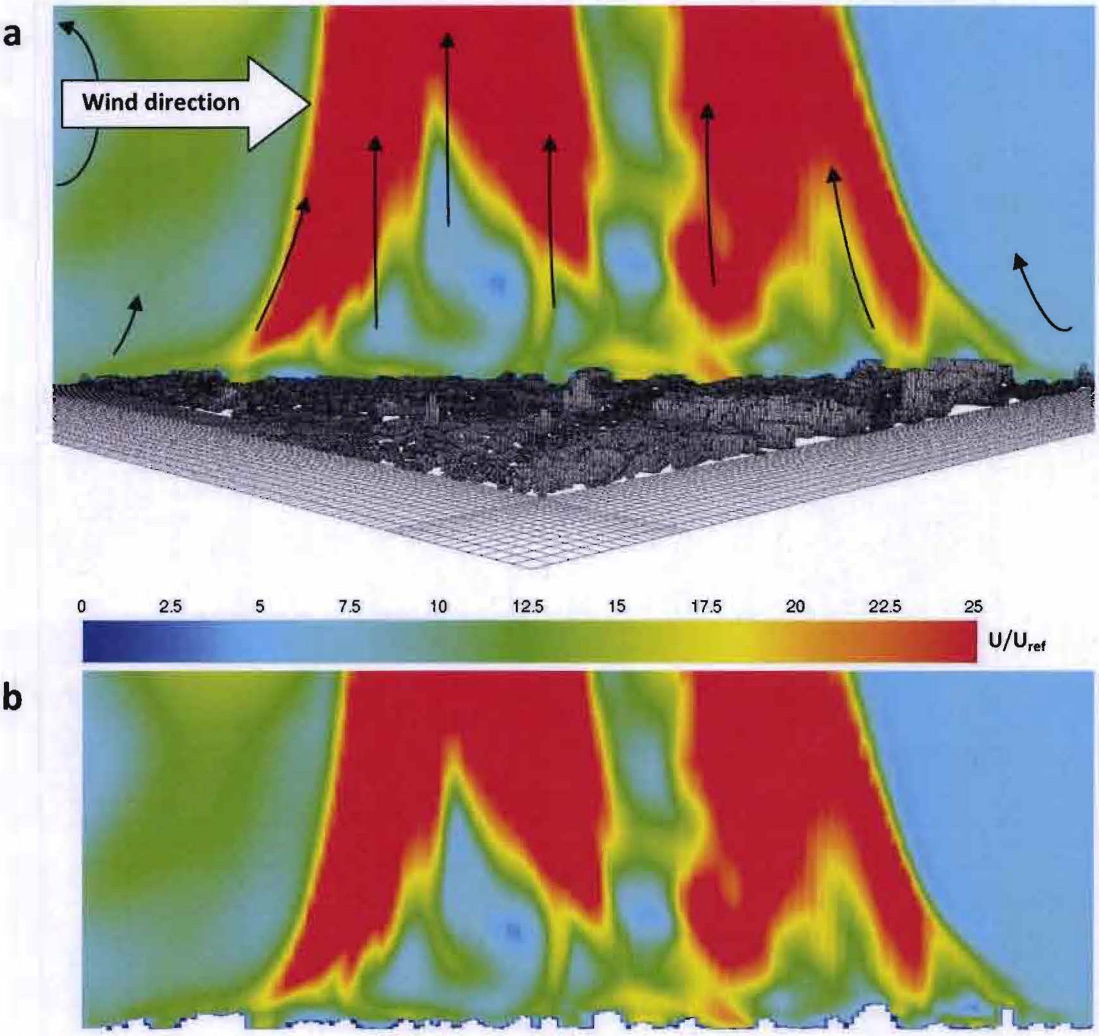

Figure 5-22: Contours of normalized mean velocity magnitude U/U_{ref} at vertical plane B for domain Residential area, U_{ref} = 0.1 m/s.

In Figure 5-23 contours of the normalized temperature in a vertical plane in the streamwise direction for domain Residential area are shown. As previously observed in the horizontal cross-sections, an amplification of up to 1.4 occurs in the region $z < 20$ m. Also, air temperatures increase at heights $z > 20$ m. Striking is that air temperature on the left side of the target area is higher than on the right side. This is a result of the predicted higher wind speeds in this part of the domain (Figure 5-22).

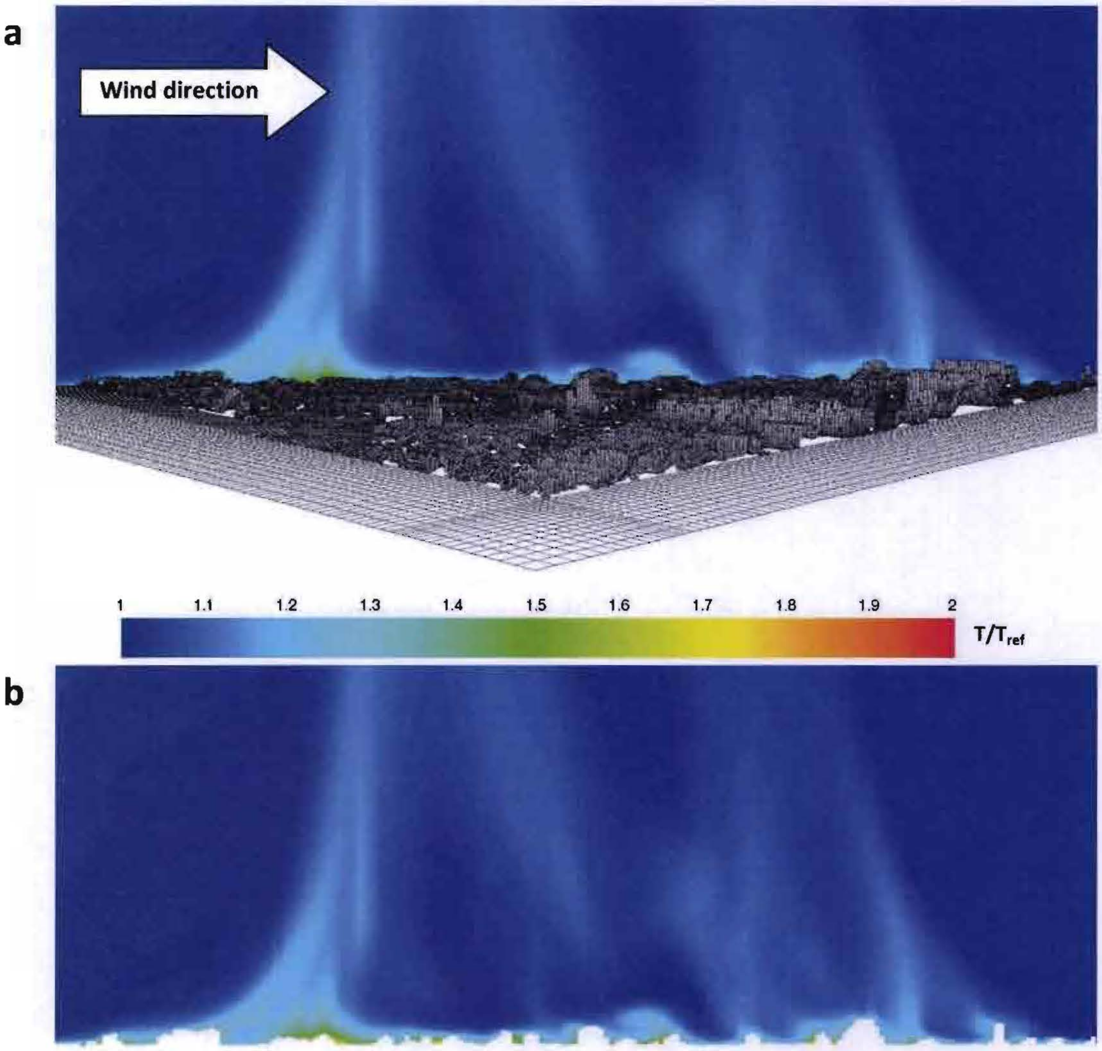

Figure 5-23: Contours of normalized temperature T/T_{ref} at vertical plane B for domain Residential area, T_{ref} = 10 °C.

5.6.3 Convective heat transfer coefficient

The convective heat transfer coefficient (CHTC) can be utilized to assess to which extent an urban area is ventilated, with respect to transporting heat from the urban environment. A high CHTC contributes to a higher degree of heat transportation than a low CHTC.

In Figure 5-24 the CHTC for domain Residential area from a top view is depicted for two simulation variants. In can be seen that for the variant with a wind-induced ventilation flow (U_{ref} = 5.0 m/s), the CHTC of building roofs, roads, pavements, and topsides of other obstacles, predominantly lies in the range 3 - 20 W/ $m^2 \cdot K$. For the variant with a buoyancy-driven flow, these values predominantly range from 5 - 13 W/ $m^2 \cdot K$.

Comparing the two top views it can be observed that in general wind-induced ventilation flow leads to a higher CHTC. Especially in the top right part of the domain where medium-rise buildings are present (encircled). These high buildings are exposed to higher velocities and herewith higher CHTCs. However, in other parts of the domain the CHTC is observed to be comparable for the two variants, e.g. as indicated by the rectangles in the figures below. Occasionally in street canyons the buoyancy-driven flow can even result in a higher CHTC, an example in the wide street as indicated by the arrow.

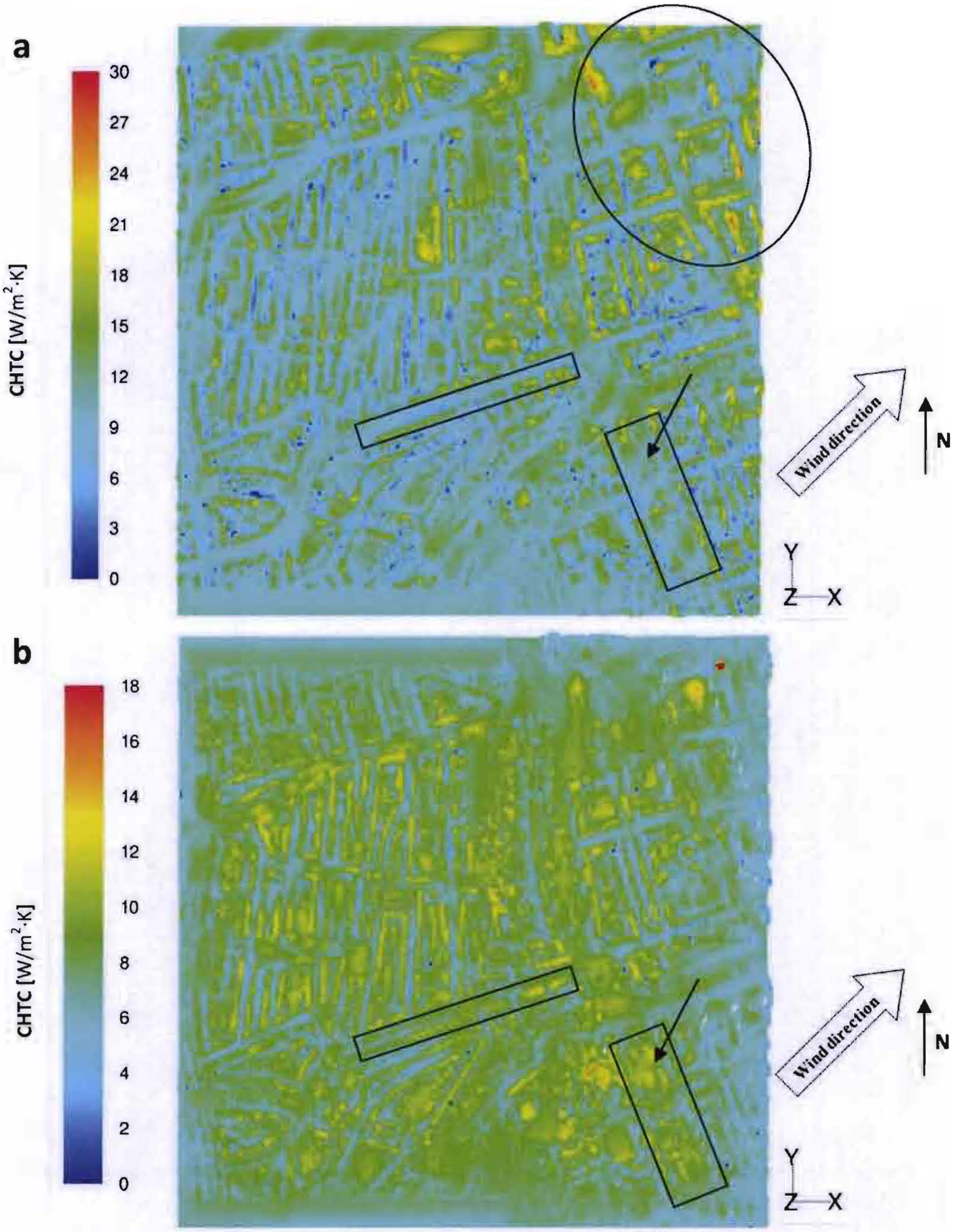

Figure 5-24: Contours of the convective heat transfer coefficient [W/m^2·K] from a top view for domain Residential area, a) U_{ref} = 5.0 m/s and b) U_{ref} = 0.1 m/s.

In Figure 5-25 the CHTC for domain Station from an isometric view is depicted for the simulation variants wind-induced flow (a) and buoyancy-driven flow (b). Similar to an area with mostly low-rise building, this domain with a combination of medium- and high-rise buildings shows that the CHTC is highest as a result of a wind-induced ventilation flow. Also, it can be seen that the CHTC of the windward facing walls is the highest for this variant. Lastly, the CHTC increases with the building height for both types of ventilation flows, (e.g. as indicated by the squares).

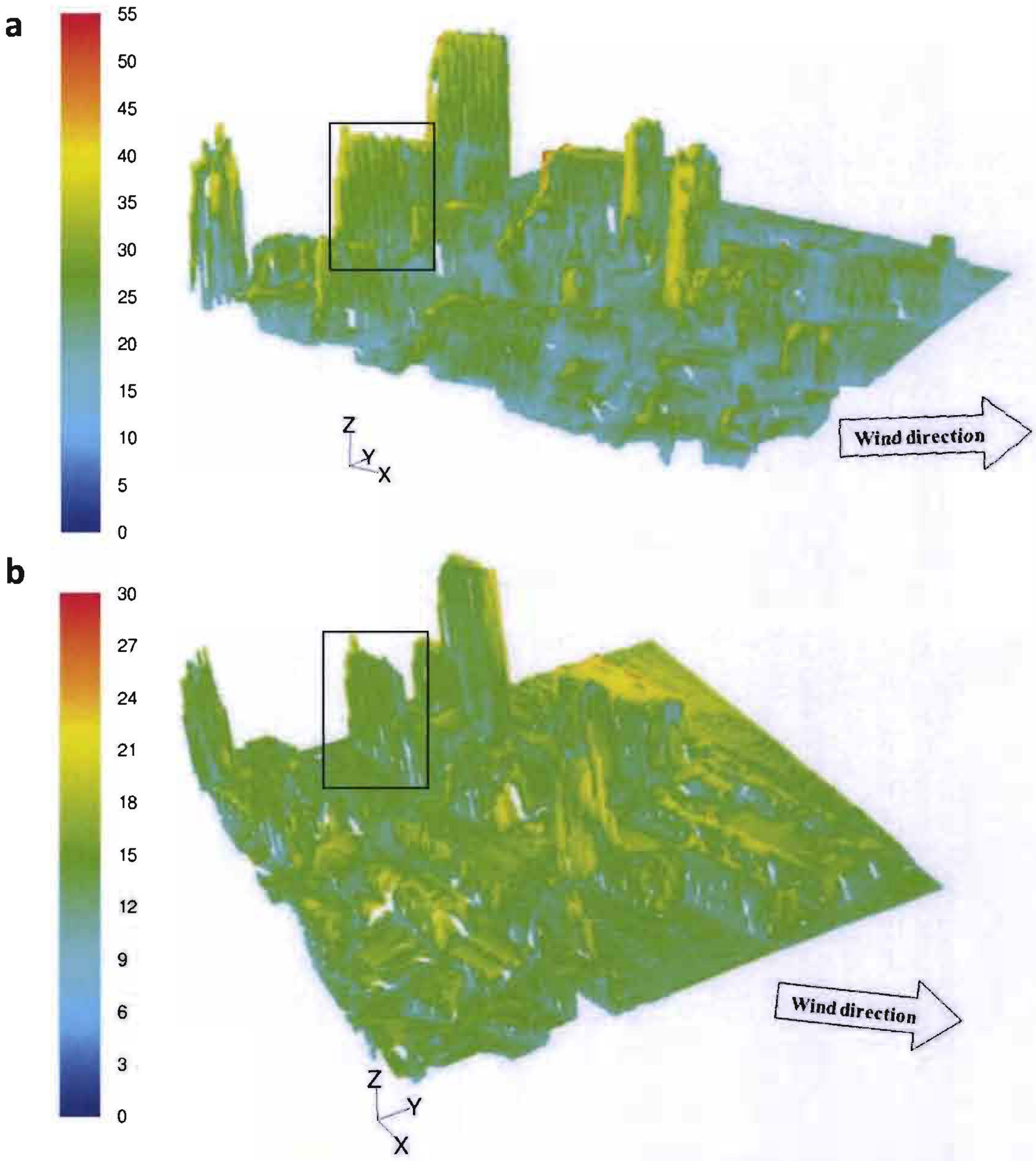

Figure 5-25: Contours of the convective heat transfer coefficient [W/m^2·K] from an isometric view for domain Station, a) U_{ref} = 5.0 m/s and b) U_{ref} = 0.1 m/s.

6 Discussion

6.1 Methodology

Emphasis in this project was placed on mapping of the applied methodology with respect to developing urban CFD models using GIS data. The method of generating the mesh files and the computational domain have therefore been extensively described in paragraphs 4.1 and 4.2. In paragraph 4.3, 'Discussion of the applied methodology', the use of the method was scrutinized and the pros and cons were discussed using practical examples encountered in this research project. Subsequently, software related errors and limitations were listed, explained, and solutions were offered in paragraphs 4.4 and 4.5. For the purpose of completeness, the points of discussion in these three paragraphs are recited below.

Discussion of applied methodology:
- GIS data and nested-grid techniques
- Creating the computational grid
- Geometry of buildings and obstacles
- Applications of the urban CFD model

Software errors and limitations:
- Increase stack size (error)
- Cannot allocate additional chunks (error)
- Too many listed boundary names (error)
- Grid display
- Computational time
- Parallel processing
- Memory cache
- Inhomogeneous flows

As the points above have previously been discussed, no further notice to these subjects is made in this discussion paragraph.

6.2 Simulation results

The simulation results for the case study city Rotterdam were presented and described in chapter 5. In this paragraph, some notes with respect to the set-up of the simulation variants and results are discussed.

Simulation set-up

The computational domains were generated according to the proposed method and later by appending domain extensions to the target areas in the lateral and streamwise direction. Ground surface height differences in the target area made it difficult to make flawless connections to the domain extensions. In this research project, the average ground surface height of the target areas was adopted as height for the bottom cell of the lateral and streamwise domain extensions. This approach inevitably influences the general wind flow as is indicated in figures of the normalized wind speed, for example the domain Station (Figure 5-11a and Figure 5-12b).

With respect to the calculated y^+ values, a wide range of 0 – 64,404 for the domains Station and Coolsingel was observed in the simulations. An even broader range of 48 – 641,951 was observed for the domain with the lowest grid resolution, Residential area. Mostly, y^+ values for the three domains do not exceed a value of approximately 25,000; higher values are observed at very few locations in the grid. Stated in literature is that standard wall functions are valid when $30 < y^{+} < 500$ (Ansys, 2009a). With urban CFD models values in this range are not feasible. Consequently, adopting standard wall functions will inevitably lead to inaccuracies. However, these high y^{+} values also show why currently, wall functions and not enhanced wall-treatment are the only option for solving near-wall flows for urban CFD models.

As mentioned in the project methodology, convective heat transfer was assumed to be the only form of heat transfer in this validation case. With respect to the remaining simulation set-up this is a reasonable assumption as radiation is nil due to imposed temperatures on all wall boundaries. Also, conduction is of no influence due to the steady-state nature of the simulation.

Variant results

Before discussing the variant results, the three adopted validation cases for this study are reviewed with respect to their applicability for validating an urban CFD model as the 2-D cases and to a lesser extent also the 3-D non-isothermal case, are relatively simple. It is however, not easy to find a suitable validation case in which both wind speed and temperature measurements are extensively described. In addition, it was not within the scope of this project to conduct full-scale measurements that could be used for validation purposes. It should be noted that the urban CFD model is deemed sufficiently validated using the adopted isothermal and non-isothermal cases, in which the wind flow around a single building and more complex flows in street canyons were included.

In paragraph 4.3 the observed holes in the geometry due to graphical limitation of the used software were discussed. Consequently, holes are also observed when creating surface contour plots, an example of this is the contour plot of the CHTC in Figure 5-25. In an early stage of the project this problem was first encountered and it was verified that similar to displaying the grid, this was only a graphical limitation. It is for example possible to plot graphs or measurement points for these surfaces.

In the isothermal variant for domain Residential area (Figure 5-14), an acceleration of the wind speed profile in the top of the domain, and a deceleration in the bottom of the domain, was observed. This contradiction can be explained by the difference in ground roughness length. The acceleration is likely a result of the lower ground roughness length that had to be adopted in the approach flow domain as a result of a limited value for the roughness constant C_s (see paragraph 2.3.4). Deceleration of the wind speed profile in the bottom part of the domain on the other hand, is a result of the difference in roughness height between the target area and the approach domain, i.e. the target areas aerodynamic roughness length is higher than that upstream.

For all variants, results of wind speed and temperature contours were presented at different heights including a height of 2 m. Accuracy of the results for this height could be questioned when discussing wind comfort at pedestrian height, as the grid lacks important details with respect to the building shapes and has a grid resolution that is too coarse near the ground to allow for accurately predicting small-scale flows.

For all simulation variants, boundary condition types were set in a similar way; a velocity-inlet, a pressure-outlet, wall boundaries at the bottom, and a symmetry boundary at the top of the domain. Based on the simulation results of the buoyancy-driven flow variants, a slightly different approach would have been more appropriate for these cases. It was observed that anomalies occurred as a result of the adopted symmetry boundary condition for the top of the domain. The Ansys manual (2009a) states that a zero flux of all quantities over a symmetry boundary is assumed, i.e. a zero normal velocity at a symmetry plane. When the mean velocity near a symmetry boundary is considered for a buoyancy-driven flow, the W component wind speed is eliminated and a horizontal component wind speed U is the result. Consequently, a vortex at the sides of a target area can occur.

Unfortunately, it is not possible to determine to which extent the upward wind flow is amplified by this phenomenon. Another observation made was that the vortex upstream of the urban area was larger than a possible downstream vortex. This is a result of the relatively short approach domain length.

Lastly, it should be stated that the accuracy of the predicted air temperature and CHTC are also discussable as both strongly depend on the wind flow and wind speed in the target area.

7 Conclusions

The aim of this study is to gain insight in the development and application of high-quality urban CFD models for analysis of natural ventilation of urban areas. To achieve this project aim, three corresponding research questions were devised which are answered in this paragraph.

1) *What information is available in literature with respect to natural ventilation of cities and the development of urban CFD models?*
   A fair number of papers are available on the subject of natural ventilation of cities. Foremost these papers describe isothermal simulations with a comparable or larger target area as applied in this study. There are multiple modeling approaches possible towards creating these large computational grids: 1) manually create the surface representation, 2) semi-automated using GIS data directly in the preprocessor, and 3) semi-automated with the use of a CAD environment. This study focused on developing an urban CFD model using the second approach. In general, it can be said that a very limited amount of information is available on, the advantages and disadvantages of these grid development methods, which problems might occur, possible software limitations, or what computational resources are required. As a result, the emphasis in this study was not only placed on analyzing natural ventilation in city, but foremost on the mapping of the applied methodology with respect to developing urban CFD models using GIS data.

2) *Can a high-quality CFD model be developed that can be used to analyze natural ventilation of a city by wind and buoyancy?*
   Despite the reduced target domain size in this study it can be concluded that an urban CFD model was successfully created and used to analyze natural ventilation of a city by wind and buoyancy. For this purpose, both isothermal and non-isothermal simulations were conducted. The simulations showed interesting results, such as complex wind-induced flows and high-velocity buoyancy-driven upward flows.

3) *To what extent can GIS data be used to develop a body-conformal structured grid for an urban CFD model and what are the current software capabilities and limitations?*
   GIS data can form the basis for generating an urban CFD model with a body-conformal structured grid. However, it has to be taken into account that the applied method in this study was not optimal; this was noted in a relatively late stage of the grid-generation process, when errors and software limitations became clear. It should be stated that, in the end, the biggest problem with the adopted methodology is the number of volumes, faces, and boundaries, that were creates for the grid. By mapping and analyzing the knowledge obtained in this study, a step was made in the right direction towards developing a method to efficiently generate a body-conformal structured grid for an urban CFD model.

8 Recommendations

During this research project, solutions were found for multiple issues, but also new research question arose. As a result, the following recommendations are made for future research projects.

Method related:

- It might be interesting to review the capabilities of the software packages Tgrid and tmerge with respect to minimizing the number of (mesh) volumes, faces, and boundaries, to make the generation of larger meshes possible. Both functions were suggested by the Ansys helpdesk (2011).
- With respect to utilizing GIS data, it might be interesting to compare the approach adopted in this project with adopting GIS data in combination with a basic map. Comparing the two methods is likely to provide a useful insight into which approach has the most potential for future projects.
- Evaluating possible measures to mitigate the UHI effect was part of the initial scope of this research project. Is should be stated that when mitigation measures are to be evaluated by an urban CFD model, moisture transport should be amongst the model's capabilities, as most mitigation measures are based on the increase of evapotranspiration.
- When GIS data is adopted to semi-automate the grid-generation process and when it is wishful to make a distinction between building roofs and the ground surface (which could be useful when, for example mitigation measures need to be implemented), it is recommended to make this distinction during the grid-generation process. This step could be incorporated in the part of the journal-file where boundary conditions are defined. The distinction could be made based on the GIS height coordinates. This may sound simple, but a lot of factors are involved making automating of this part of the grid-generation process difficult.
- The evaluation of pollution and smoke dispersion in urban areas fall outside of the scope of this study. However, with the right knowledge on required model and grid characteristics these issues might be easier to implement into an urban CFD model then UHI effect mitigation measures. Reason for this is that neither pollution nor smoke dispersion is troubled by assigning boundary conditions to specific buildings surfaces. For these types of simulations, other issues, such as defining sources of pollution and fire are of importance.

Simulation related:

- Striking is that the grid resolution in the validation cases is substantially higher than was recommended in literature. Suggested is a minimum of 10 cells per building side (Franke et al., 2007; Tominaga et al., 2008), where for the validation cases in this study acceptable results were obtained for grids twice as fine (with respect to the suggested refinement factor of 1.5). Based on these observations, it is therefore recommended that more than 10 cells per building side are adopted when possible. It should be stated that the minimum number of cells strongly depends on the size of the buildings and application of the grid.
- Based on experiences from this study, a GIS data grid resolution of 1 or 2 meters is deemed sufficient as a starting point towards creating a high-quality urban CFD model.
- The resolution in the z-direction should be fine enough to accurately impose the vertical wind speed profile and calculate its development throughout the domain.
- An outlet-boundary condition should be adopted for the top of the domain when simulating buoyancy-driven flows. Observations in this study indicated inaccurate results when a symmetry boundary condition is adopted.
- When transient calculations are conducted using the created grids, heat capacity of constructions should be include in the model. Such a model is likely to provide interesting results.

References

Ahmad, K., Khare, M., Chaudhry, K.K., 2005. *Wind tunnel simulation studies on dispersion at urban street canyons and intersections - a review*, Journal of Wind Engineering and Industrial Aerodynamics 93: 697–717.

Ansys, 2009a. *Ansys 12.0 user's guide*.

Ashie, Y., Thanh, V.C., Asaeda, T., 1999. *Building canopy model for the analysis of urban climate*, Journal of Wind Engineering and Industrial Aerodynamics 81: 237–248.

Baik, J.J., Park, S.-B., Kim, J.J., 2009. *Urban flow and dispersion simulation using a CFD model coupled to a mesoscale model*, Journal of Applied Meteorology and Climatology 48: 1667-1681.

Baetke, F., Werner, H., Wengle, H., 1990. *Numerical simulation of turbulent flow over surface mounted obstacles with sharp edges and corners*, Journal of Wind Engineering and Industrial Aerodynamics 35: 129-147.

Bartzis, J.G., Vlachogiannis, D., Sfetsos, A., 2004. *Thematic area 5: Best practice advice for environmental flows*, The QNET-CFD Network Newsletter, volume 2, number 4: 34-39.

Blocken, B., Stathopoulos, T., Carmliet, J., 2007. *CFD simulation of the atmospheric boundary layer: wall function problems*, Atmospheric Environment 41: 238-252.

Brown, M., Leach, M., Reisner, J., Stevens, D., Smith, S., Chin, S., Chan, S., Lee, B., 2000. *Numerical modeling from mesoscale to urban scale to building scale*, Third symposium on urban environment, American Meteorological Society, pages 64-65.

Burrows, D.A., Hendricks, E.A., Diehl, S.R., Keith, R., 2007. *Modeling turbulent flow in an urban central business district*, Journal of Applied Meteorology and Climatology 46: 2147-2164.

Ca, V.T., Asaeda, T., Abu, E.M., 1998. *Reductions in air-conditioning energy caused by a nearby park*, Energy and Buildings 29: 83–92.

Casey, M., Wintergerste, T., 2000. ERCOFTAC special interest group on *Quality and trust in industrial CFD*, Best Practice Guidelines, Fluid Dynamics Laboratory, Sulzer Innotec.

Chan, S.T., Leach, M.J., 2003. *A validation of FEM3MP with joint urban 2003 data*, Journal of Applied Meteorology and Climatology 46: 2127-2146.

Coirier, W. J., Kim, S., Chen, F., Tewari, M., 2006a. *Evaluation of urban scale contaminant transport and dispersion modeling using loosely coupled CFD and mesoscale models*, The 86th AMS annual meeting, Sixth symposium on the urban environment, Atlanta.

Coirier, W.J., Fricker, M., Furmanczuk, M., Kim, S., 2006b. *A computational fluid dynamics approach for urban area transport and dispersion modeling*, Environmental Fluid Mechanics 5: 443–479.

Cowan, I.R., Castro, I.P., Robins, A.G., 1997. *Numerical considerations for simulations of flow and dispersion around buildings*, Journal of Wind Engineering and Industrial Aerodynamics, volumes 67 and 68: 535-545.

Cox, C.F., Cybyk, B. Z., Boris, J. P., Fung, Y. T., Chang, S. W., 2000. *Coupled microscale -mesoscale modeling of contaminant transport in urban environments*, Third symposium on urban environment, American Meteorological Society, pages 66-67.

Dimitrova, R., Sini, J.-F., Richards, K., Schatzmann, M., Weeks, M., Perez Garciá, E., Borrego, C., 2009. *Influence of thermal effects on the wind field within the urban environment*, Boundary-Layer Meteorology 131: 223-243.

Dixon, N.S., Boddy, J.W.D., Smalley, R.J., Tomlin, A.S., 2006. *Evaluation of a turbulent flow and dispersion model in a typical street canyon in York*, Atmospheric Environment 40: 958–972.

Ehrhard, J., Khatib, I. A., Winkler, C., Kunz, R., Moussiopoulos, N., Ernst, G., 2000. *The microscale model MIMO: development and assessment*, Journal of Wind Engineering and Industrial Aerodynamics 85: 163-176.

Franke, J., Hirsch, C., Jensen, A.G., Krüs, H.W., Schatzmann, M., Westbury, P.S., Miles, S.D., Wisse, J.A., Wright, N.G., 2004. *Recommendations on the use of CFD in wind engineering. In: COST action C14 (editor van Beeck, J.P.A.J.) - Impact of wind and storm on city life built environment.* Proceedings of the international conference on urban wind engineering and building aerodynamics, Von Karman Institute, Sint-Genesius-Rode, Belgium.

Franke, J., Hellsten, A., Schlünzen, H., Carissimo, B., 2007. *Best Practice Guideline for the CFD simulation of flows in the urban environmen*t, COST Office, Brussels, ISBN 3-00-018312-4.

Fu, S., Launder, B. E., Leschziner, M. A., 1987. *Modeling strongly swirling re-circulating jet flow with Reynolds-stress transport closures*, Sixth symposium on turbulent shear flows, Toulouse, France.

Gibson, M. M., Launder, B. E., 1978. *Ground effects on pressure fluctuations in the atmospheric boundary layer*, Journal of Fluid Mechanics 86: 491-511.

Gidhagen, L., Johansson, C., Langner, J., Olivares, G., 2004. *Simulation of NO_x and ultrafine particles in a street canyon in Stockholm*, Atmospheric Environment 38: 2029–2044.

Giridharan, R., Lau, S.S.Y., Ganesan, S., 2005. *Nocturnal heat island effect in urban residential developments of Hong Kong*, Energy and Buildings 37: 964–971.

Giridharan, R., Lau, S.S.Y., Ganesan, S., Givoni, B., 2008. *Lowering the outdoor temperature in high-rise high-density residential developments of coastal Hong Kong: the vegetation influence*, Building and Environment 43: 1583–1595.

Giridharan, R. , Kolokotroni, M., 2009. *Urban heat island characteristics in London during winter*, Solar Energy 83: 1668–1682.

Golden, J.S., Carlson, J., Kaloush, K.E., et al., 2007. *A comparative study of the thermal and radiative impacts of photovoltaic canopies on pavement surface temperatures*, Solar Energy 81: 872–883.

Hall, R.C. (Ed.), 1997. *Evaluation of modeling uncertainty - CFD modeling of near-field atmospheric dispersion,* Project EMU final report, European Commission Directorate–General XII Science, Research and development contract EV5V-CT94-0531, WS Atkins Consultants Ltd., Surrey.

Hargreaves, D.M., Wright, N.G., 2007. *On the use of the k–ε model in commercial CFD software to model the neutral atmospheric boundary layer*, Journal of Wind Engineering and Industrial Aerodynamics 95: 355–369.

Heier, S., 2005. *Grid integration of wind energy conversion systems*, Chichester, John Wiley and Sons, ISBN 0470868996.

Hinze, J.O., 1975. *Turbulence*, McGraw-Hill Publishing Co., New York.

Hooff, T. van, Blocken, B., 2010. *Coupled urban wind flow and indoor natural ventilation modeling on a high-resolution grid: a case study for the Amsterdam Arena stadium*, Environmental Modeling and Software 25: 51-65.

Howard, L., 1818-1820. *The climate of London, deduced from meteorological observations, made at different places in the neighborhood of the metropolis*, volume 2: 338-346, London.

Huang, H., Ooka, H., Kato, S., 2005. *Urban thermal environment measurements and numerical simulation for an actual complex urban area covering a large district heating and cooling system in summer*, Atmospheric Environment 39: 6362–6375.

Iaccarino, G., Mittal, R., 2005. *Immersed boundary methods*, Annual Review of Fluid Mechanics 37: 239-61.

Iaccarino, G., Moreau, S., 2006. *Natural and forced conjugate heat transfer in complex geometries on Cartesian adapted grids*, Transaction on the ASME, volume 128: 838-46.

Ihara, T., Kikegawa, Y., Asahi, K., 2008. *Changes in year round air temperature and annual energy consumption in office building areas by urban heat-island countermeasures and energy saving measures*, Applied Energy 85(1): 12–25.

Jain, S.P., Rao, K.R., 1974. *Experimental study on the effect of roof spray cooling on unconditioned and conditioned buildings*, Building Science 9(1): 9–16.

Jensen, N.O., Lundtang Petersen, E., Troen, I., 1984. *Extrapolation of mean wind statistics with special regard to wind energy applications*, WMO (World Meteorological Organization), Geneva, WCP-86.

Jusuf, S.K., Wong, N.H., Hagen, E., Anggoro, R., Hong, Y., 2007.The influence of land use on the urban heat island in Singapore, Habitat International 31: 232–242.

Kikegawa, Y., Genchi, Y., Yoshikado, H., Kondo, H., 2003. *Development of a numerical simulation system toward comprehensive assessments of urban warming countermeasures including their impacts upon the urban buildings, energy demands*, Applied Energy 76: 449–466.

Kikegawa, Y., Genchi, Y., Kondo, H., Hanaki, K., 2006. *Impacts of city-block-scale counter measures against urban heat island phenomena upon a building's energy consumption for air conditioning*, Applied Energy 83(6): 649–668.

Kolokotroni, M., Giannitsaris, I., Watkins, R., 2006. *The effect of the London Urban Heat Island on building summer cooling demand and night ventilation strategies*, Solar Energy 80(4): 383–392.

Kolokotsa, D., Psomas, A., Karapidakis, E., 2009. *Urban heat island in southern Europe: the case study of Hania, Crete*, Solar Energy 83: 1871–1883.

Kondo, H., Asahi, K., Tomizuka, T., Suzuki, M., 2006. *Numerical analysis of diffusion around a suspended expressway by a multi-scale CFD model*, Atmospheric Environment 40: 2852-2859.

Konopacki, S., Akbari, H., 2002. *Energy savings for heat island reduction strategies in Chicago and Houston (including updates for Baton Rouge, Sacramento, and Salt Lake City)*, Draft Final Report, LBNL-49638, University of California, Berkeley.

Kovar-Panskus, A., Louka, P., Sini, J.-F., Savory, E., Czech, M., Abdelqari, A., Mestayer, P.G., Toy, N., 2002a. *Influence of geometry on the mean flow within urban street canyons – a comparison of wind tunnel experiments and numerical simulations*, Water, Air and Soil Pollution, Focus 2: 365-380.

Kovar-Panskus, A., Moulinneuf, L., Savory, E., Abdelqari, A., Sini, J.-F., Rosant, J.-M., Robins, A., Toy, N., 2002b. *A wind tunnel investigation of the influence of solar-induced wall-heating on the flow regime within a simulated urban street canyon*, Water, Air and Soil Pollution, Focus 2: 555-571.

Launder, B. E., Spalding, D. B., 1972. *Lectures in mathematical models of turbulence*, Academic Press, London, England.

Launder, B. E., Spalding, D. B., 1974. *The numerical solving of turbulent* flows, Computer Methods in Applied Mechanics and Engineering, volume 3, issue 2: 269-289.

Launder, B. E., 1989a. *Second-moment closure and its use in modeling turbulent industrial flows*, International Journal for Numerical Methods in Fluids 9: 963-985.

Launder, B. E., 1989b. *Second-Moment Closure: present... and future?* International Journal of Heat and Fluid Flow 10(4): 282-300.

Louka, P., Vachon, G., Sini, J.-F., Mestayer, P.G., Rosant, J.-M., 2002. *Thermal effects on the airflow in a street canyon—Nantes '99 experimental results and model simulations*, Water, Air and Soil Pollution, Focus 2: 351–364.

Lu, J., Chen, J-h., Feng, T.T.Y., Wang, J-s., 2007. *High-rise buildings versus outdoor thermal environment in chongqing*, Sensors 7: 2183-2200.

Matzarakis, A., Mayer, H., 1991. *The extreme heat wave in Athens in July 1987 from the point of view of human biometeorology*, Atmospheric Environment 25B (2): 203-211.

Memon, R.A., Leung, D.Y.C., Chunho, L., 2008. *A review on the generation, determination and mitigation of Urban Heat Island*, Journal of Environmental Sciences 20: 120–128.

Neofytou, P., Haakana, M., Venetsanos, A., Kousa, A., Bartzis J., Kukkonen, J., 2008. *Computational fluid dynamics modeling of the pollution dispersion and comparison with measurements in a street canyon in Helsinki*, Environ Model Assess 13: 439–448.

Mochida, A., Iizuka, S., Tominaga, Y., Yu-Fat Lun, I, 2010. *Up-scaling CWE models to include mesoscale meteorological influences*, Journal of Wind Engineering and Industrial Aerodynamics, Fifth symposium on computational wind engineering (CWE2010), USA.

Murakami, S., Otsuka, K., Mochida, A., Kataoka, H., Kato, S., 2003a. *CFD prediction of flow over complex terrain using local area wind energy prediction system (LAWEPS)*, Conference preprints of 11th international conference on wind engineering, Texas, Volume 2: 2821-2828.

Murakami, S., Mochida, A, Kato, S., 2003b. *Development of local area wind prediction system for selecting suitable site for windmill*, Journal of Wind Engineering and Industrial Aerodynamics 91: 1759-1776.

NEN-EN 1990, 2002. *Eurocode – Basis of structural design.*

Nozu, T., Tamura, T., 2006. *Application of fluid technique with high accuracy and conservation property to the wind resistant problems of buildings and structures*, Journal Structural and Construction Engineering 605: 27–35.

Nozu, T., Tamura, T., Okuda, Y., Sanada, S., 2008. *LES of the flow and building wall pressures in the center of Tokyo*, Journal of Wind Engineering and Industrial Aerodynamics 96 (10, 11): 1762–1773.

NPR 6097, 2006. *Toepassing van de statistiek van de uurgemiddelde windsnelheden voor Nederland*, ICS 07.060.

Oke, T.R., 1982. *The energetic basis of the urban heat island*, Quarterly Journal of the Royal Meteorological Society 108: 1–24.

Orszag, S.A., Yakhot, V., Flannery, W.S., Boysan, F., Choudhury, D., Maruzewski, J., Patel, B., 1993. *Renormalization group modeling and turbulence simulations*, International conference on near-wall turbulent flows, Arizona.

Peskin, C.S, 1972. *Flow patterns around heart valves: a digital computer method for solving the equations of motion*, PhD thesis, Physiological Albert Einstein College of Medicine, University Microfilms 378:72–30.

Richards, K., Schatzmann, M., Leitl, B., 2006. *Wind tunnel experiment modeling thermal effects within the vicinity of a single block building with leeward wall heating*, Journal of Wind Engineering and Industrial Aerodynamics 94: 621–636.

Richards, P.J., Hoxey, R.P., 1993. *Appropriate boundary conditions for computational wind engineering models using the k-ε turbulence model*, Journal of Wind Engineering and Industrial Aerodynamics 46 and 47: 145-153.

Rosenfeld, A.H., Akbari, H., Romm, J.J., 1998. *Cool communities: Strategies for heat island mitigation and smog reduction*, Energy and Buildings 28: 51–62.

Ruck, B., 1993. *Wind-tunnel measurements of flow field characteristics around a heated building model*, Journal of Engineering and Industrial Aerodynamics 50: 139-152.

Shih, T.-H., Liou, W. W., Shabbir, A., Yang, Z., Zhu, J., 1995. *A new k-ε eddy-viscosity model for High Reynolds -number turbulent flows - model development and validation*, Computers Fluids 24(3): 227-238.

Sarrata, C., Lemonsub, A., Massona, V., Guedaliac V., 2006. *Impact of urban heat island on regional atmospheric pollution*, Atmospheric Environment 40: 1743–1758.

Scaperdas, A., Gilham, S., 2004. *Thematic area 4: Best practice advice for civil constructions and HVAC*, The QNET-CFD Network Newsletter, volume 2, number 4, pages 28-33.

Sodha, M.S., Govind, P.K., Kaushik, S.C., 1980. *Reduction of heat flux by a flowing water layer over an insulated roof*, Building and Environment 15(2): 133–140.
Speziale, C. G., Sarkar, S., Gatski, T. B., 1991. Modelling the pressure-strain correlation of turbulence: an invariant dynamical systems approach, Journal of Fluid Mechanics 227:245-272.

Spronken-Smith, R.A., Oke, T.R., Lowry, W.P., 2000. *Advection and the surface energy balance across an irrigated urban park*, International Journal of Climatology 20: 1033–1047.

Taha, H., Konopacki, S., Gabersek, S., 1999. *Impacts of large scale modifications on meteorological conditions and energy use: A 10-region modeling study*, Theoretical and Applied Climatology 62: 175–185.

Takebayashi, H., Moriyama, M., 2007. *Surface heat budget on green roof and high reflection roof for mitigation of urban heat island*, Building and Environment 42: 2971–2979.

Tamura, T., Nagayama, J., Ohta, K., Okuda, Y., 2006. *LES estimation of environmental degradation at the urban heat island due to densely-arrayed tall buildings*, 17th symposium on boundary layers and turbulence, AMS, pages 22–25.

Tamura, T., 2008. *Towards practical use of LES in wind engineering*, Journal of Wind Engineering and Industrial Aerodynamics 96: 1451–1471.

Tiwari, G.N., Kumar, A., Sodha, M.S., 1982. *A review – cooling by water evaporation over roof*, Energy Conversion and Management 22(2): 143–153.

Tominaga, Y., Mochida, A., Yoshie, R., Kataoka, H., Nozu, T., Yoshikawa, M., Shirasawa, T., 2008. *AIJ guidelines for practical applications of CFD to pedestrian wind environment around buildings*, Journal of Wind Engineering and Industrial Aerodynamics 96: 1749–1761.

Tong, H., Walton, A., Sang, J., Chan, J.C.L., 2005. *Numerical simulation of the urban boundary layer over the complex terrain of Hong Kong*, Atmospheric Environment 39: 3549–3563.

Urano, A., Ichinose, T., Hanaki, K., 1999. *Thermal environment simulation for three dimensional replacement of urban activity*, Journal of Wind Engineering and Industrial Aerodynamics 81: 197–210.

Wieringa, J., 1992. *Updating the Davenport roughness classification*, Journal of Wind Engineering and Industrial Aerodynamics 41: 357-368.

Wilcox, D. C., 1998. *Turbulence Modeling for CFD*, DCW Industries, La Canada, California, ISBN 0963605151.

Solecki, W.D., Rosenzweig, C., Parshall, L., Pope, G., Clark, M., Cox, J., Wiencke, M., 2005. *Mitigation of the heat island effect in urban New Jersey*, Environmental Hazards 6: 39–49.

Yakhot, V., Orszag, S. A., 1986. *Renormalization group analysis of turbulence, I. Basic Theory*, Journal of Scientific Computing 1(1): 1-51.

Yamamota, Y., 2007. *Measures to mitigate urban heat islands*, Science and Technology Trends Quarterly review, number 18.

Yoshie, R., Mochida, A., Tominaga, Y., Kataoka, H., Harimoto, K., Nozu, T., Shirasawa, T., 2007. *Cooperative project for CFD prediction of pedestrian wind environment in the Architectural Institute of Japan*, Journal of Wind Engineering and Industrial Aerodynamics 95: 1551–1578.

Yu, C., Hien, W.N., 2006. *Thermal benefits of city parks*, Energy and Buildings 38: 105–120.

Zeng, Y., Qiu, X.F., Gu, L.H., He, I.J., Wang, K.F., 2009. *The urban heat island in Nanjing*, Quaternary International 208: 38–43.

Personal contact

Ansys help-desk, 2011. Asking questions concerning Ansys functionality using the Constumer Portal on the Ansys website.

Programs

The MathWorks Inc., February 2010. Matlab Version 7.10.0.499, R2010a

Gambit, 2004. Gambit version 2.4.6

Ansys, 2009b. Ansys Fluent 12.1.4

Google Earth, 2011. Google Earth 6 (free download)

Websites

Ansys (2011), Product information on de Ansys program Tgrid. Available at: http://www.ansys.com/Products/Other+Products/TGrid (Accessed: July 2011).

AHN (2010), Algemeen Hoogtebestand Nederland. Available at: http://www.ahn.nl/actualisatie_van_het#1092528 (Accessed: November 2010).

Bing maps (2011), www.bing.com.maps (Accessed: September 2011).

Earth Policy (2003), Record heat wave in Europe takes 35,000 lives. Available at: http://www.earth-policy.org/plan_b_updates/2003/update29 (Accessed: June 2011)

New Scientist (2003), European heat wave caused 35,000 deaths. Available at: http://www.newscientist.com/article/dn4259-european-heatwave-caused-35000-deaths.html (Accessed: June 2011)

Sybase (2011), Alphabetic listing of configuration parameters Available at: http://infocenter.sybase.com/help/index.jsp?topic=/com.sybase.help.ase_15.0.sag1/html/sag1/sag1323.htm (Accessed: July 2011)